

1 **Concerted epithelial and stromal changes during progression** 2 **of Barrett's Esophagus to invasive adenocarcinoma exposed** 3 **by multi-scale, multi-omics analysis**

4
5 Michael K. Strasser^{1#}, David L. Gibbs^{1#}, Philippe Gascard², Joanna Bons³, John W. Hickey⁴, Christian M.
6 Schürch^{4,5}, Yuqi Tan⁴, Sarah Black⁴, Pauline Chu^{4,6}, Alican Ozkan⁷, Nathan Basisty³, Veena Sangwan⁸, Jacob
7 Rose³, Samah Shah³, Sophie Camilleri-Broet⁹, Pierre-Oliver Fiset⁸, Nicolas Bertos⁸, Julie Berube⁸, Haig
8 Djambazian¹⁰, Rui Li¹⁰, Spyridon Oikonomopoulos¹⁰, Daffolyn Rachael Fels-Elliott¹¹, Sarah Vernovsky⁷, Elee
9 Shimshoni⁷, Deborah Collyar¹², Ann Russell¹³, Ioannis Ragoussis¹⁰, Matthew Stachler², James R.
10 Goldenring¹⁴, Stuart McDonald¹⁵, Donald E. Ingber^{7#}, Birgit Schilling^{3#}, Garry P. Nolan^{4,6#}, Thea D. Tlsty^{2#},
11 Sui Huang^{1#*}, Lorenzo E. Ferri^{8#}

12 1. Institute for Systems Biology, Seattle, WA, USA

13 2. Department of Pathology, University of California, San Francisco, CA, USA.

14 3. The Buck Institute for Research on Aging, Novato, CA, USA

15 4. Department of Microbiology & Immunology, Stanford University School of Medicine, Stanford, CA, USA

16 5. Department of Pathology and Neuropathology, University Hospital and Comprehensive Cancer Center Tübingen,
17 Tübingen, Germany

18 6. Department of Pathology, Stanford University School of Medicine, Stanford, CA, USA

19 7. Wyss Institute for Biologically Inspired Engineering at Harvard University, Boston, MA, USA.

20 8. Division of Thoracic and Upper Gastrointestinal Surgery, Montreal General Hospital, McGill University Health
21 Centre, Montreal, QC, Canada

22 9. Division of Pathology, McGill University Health Center, Montreal, QC, Canada

23 10. McGill Genome Centre and Department of Human Genetics, McGill University, Montreal, QC, Canada

24 11. University of Kansas Medical Center, Kansas City, KS, USA

25 12. Patient Advocates in Research, Danville, CA, USA.

26 13. National Cancer Research Institute, London, UK.

27 14. Nashville VA Medical Center and Section of Surgical Sciences, Department of Cell and Developmental Biology,
28 Epithelial Biology Center, Vanderbilt University Medical Center, Nashville, TN USA

29 15. Centre for Cancer Genomics and Computational Biology, Barts Cancer Institute, Barts and The London School of
30 Medicine and Dentistry, Queen Mary University of London, London, UK

31 # equal contribution

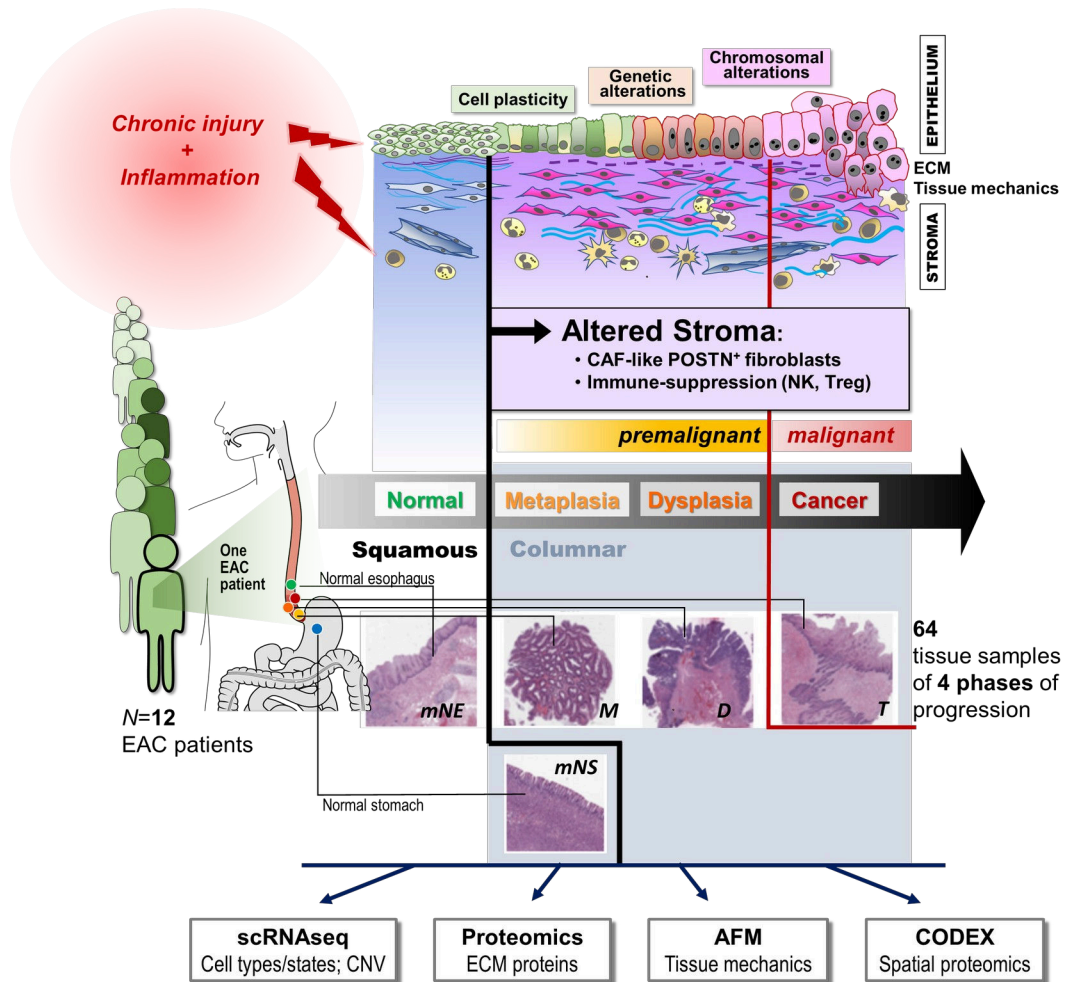
32 *Correspondence: sui.huang@isbscience.org, lorenzo.ferri@mcgill.ca

34

35 **Abstract (120 WORDS)**

36 Esophageal adenocarcinoma arises from Barrett’s esophagus, a precancerous metaplastic replacement
 37 of squamous by columnar epithelium in response to chronic inflammation. Multi-omics profiling,
 38 integrating single-cell transcriptomics, extracellular matrix proteomics, tissue-mechanics and spatial
 39 proteomics of 64 samples from 12 patients’ paths of progression from squamous epithelium through
 40 metaplasia, dysplasia to adenocarcinoma, revealed shared and patient-specific progression
 41 characteristics. The classic metaplastic replacement of epithelial cells was paralleled by metaplastic
 42 changes in stromal cells, ECM and tissue stiffness. Strikingly, this change in tissue state at metaplasia
 43 was already accompanied by appearance of fibroblasts with characteristics of carcinoma-associated
 44 fibroblasts and of an NK cell-associated immunosuppressive microenvironment. Thus, Barrett’s
 45 esophagus progresses as a coordinated multi-component system, supporting treatment paradigms that
 46 go beyond targeting cancerous cells to incorporating stromal reprogramming.

47
 48



49 INTRODUCTION

50 Esophageal cancer is the seventh most common cancer worldwide¹ and can be divided into two major
51 subtypes that constitute biologically distinct diseases: esophageal squamous cell carcinoma (ESCC),
52 observed predominantly in the upper esophagus, and esophageal adenocarcinoma (EAC), typically
53 located in the lower esophagus². These subtypes differ in etiology, epidemiology and genetic
54 characteristics. ESSC is the dominant type in much of Asia³ while EAC is the prevalent type in Western
55 countries, with a rapidly increasing incidence of currently 5-10 cases/100,000/year^{4,5}.

56 Histologically, EAC frequently displays a glandular tissue structure and genomic alterations that are
57 indistinguishable from those of the chromosomally unstable variant of proximal gastric cancer⁶ and very
58 distinct from the original squamous tissue structure typical of the esophagus. Most EACs typically
59 develop from metaplasia, an adaptive change to chronic injury caused by gastro-esophageal reflux
60 (GERD) of the lower mucosa of the esophagus known as Barrett's esophagus (BE)⁷. In this metaplastic
61 adaptive response driven by chronic inflammation, native squamous epithelium of the normal
62 esophagus is replaced by a columnar epithelium with gastric and/or intestinal characteristics and mucin
63 secretion. The prevalence of BE in the general population in Western countries is estimated to be 2%
64 and is typically only diagnosed incidentally in patients with symptomatic GERD who undergo endoscopy.
65 Patients with BE have a 40-fold increased lifetime risk of developing EAC. However, only a small minority
66 of BE cases (<1% per patient/year) progress to invasive carcinoma⁸.

67
68 Recent genome-wide analyses have focused on the identification of molecular changes occurring in the
69 esophagus epithelium during the emergence of BE to address the long-standing question of the cellular
70 origin of the metaplastic cells⁷ and characterize early genomic, extrachromosomal⁹⁻¹³ and
71 transcriptomic alterations^{14,15}. However, increasing evidence suggest that stromal alterations due to
72 chronic injury play a central role in development of metaplasia and progression to cancer¹⁶⁻¹⁸.
73 Therefore, it becomes paramount to investigate disease processes in the context of the whole tissue
74 rather than focusing only on one of its components, i.e., the epithelium. To this end, we performed a
75 systematic multi-omics analysis to characterize, in depth, the concomitant changes in epithelial,
76 immune, and stromal cell landscape, as well as changes in composition of the extracellular matrix and
77 tissue mechanics, during progression to cancer.

78
79 Chronic inflammation due to recurrent tissue injury can perturb tissue homeostasis and thereby
80 contribute to tumorigenesis¹⁹. Failure to restore the original tissue structure perpetuates an aberrant
81 regenerative response in which the parenchymal cells do not return to a normal, stably-differentiated
82 state. The tissue may enter a metaplastic state that constitutes an adaptive response. In the case of BE-
83 associated EAC, the esophageal mucosa is exposed to prolonged bile salts and acid reflux, dietary
84 irritants, alcohol, and smoking and the squamous epithelia of the lower esophagus is replaced by
85 columnar gastro-intestinal epithelia. For poorly understood reasons, metaplasia, inflammation and
86 stromal reorganization also place the tissues at a higher risk for malignancy. We have examined how this
87 perturbed homeostasis may drive tumorigenesis. The multifocal nature of BE-associated EAC, repeated
88 endoscopic surveillance and surgical resection in the absence of (neo)adjuvant therapy affords an
89 unparalleled opportunity to obtain a unique cohort of patient-matched tissue samples corresponding to

90 all clinical histological/diagnostic stages (hereafter, considered the biological ‘*phase*’ of progression) that
91 can be captured at a single time point in a given patient.

92

93 Our simultaneous multi-omics analysis of parenchyma and stroma at the various phases of progression
94 of BE to EAC revealed a coordinated program of non-genetic plasticity that included the epithelium, the
95 extracellular matrix (ECM) and stroma. This change in multi-component tissue identity at the
96 metaplastic phase was accompanied by acquisition of an NK-associated immunosuppressive tissue state
97 and the appearance of fibroblasts with characteristics previously associated with malignant stroma. The
98 joint consideration of single-cell resolution and tissue level molecular profiles enabled us to link known
99 and novel molecular markers of progression to their cellular origins and to shifts in cell-type
100 composition. Together, this multi-scale integration offers a starting point for designing multi-pronged
101 stromal reprogramming as a new therapeutic modality for reverting premalignancy or preventing
102 malignant progression.

103 RESULTS

104 Patient Recruitment and Sample Characteristics

105 A unique cohort of patients with BE-associated esophageal EAC was prospectively recruited to
106 participate in this study. A total of 64 fresh tissue samples from 12 newly diagnosed, treatment-naive
107 patients with confirmed EAC were collected for multi-omics analysis (Figs. 1A & S1). The samples
108 encompassed inflamed squamous esophagus (>5cm proximal to apical columnar-lined mucosa),
109 suspected Barrett’s metaplasia (columnar-lined mucosa), suspected dysplasia (based on high resolution
110 white light and narrow band imaging on endoscopy), and malignant tumor. In the majority of cases, we
111 also collected columnar stomach (gastric cardia) tissue. Samples were collected at the time of
112 endoscopy (5/12) or surgical resection (7/12). Histological confirmation of suspected tissue
113 diagnosis/stage (phase of progression, see below) was provided by independent analysis by two expert
114 pathologists and the samples were labeled accordingly (Methods). Patient information, sample
115 description, and histological diagnosis are provided in Table S1.

116

117 Global survey of cell types in progression from inflamed esophagus to EAC

118 Transcriptomic profiling of 64 samples collected from 12 patients with EAC by single-cell RNA
119 sequencing (scRNA-seq) captured the transcriptomes of 175,586 individual cells (Methods). This dataset
120 consisted of patient-matched samples encompassing, in various combinations, the multiple phases of BE
121 progression defined by the clinical-histological stage/diagnosis: matched “Normal” Esophagus (*mNE*)
122 (obtained from the inflamed squamous esophageal tissue adjacent to the lesion), Barrett’s Metaplasia
123 (*M*), Dysplasia (*D*), Tumor (*T*), and matched “Normal” Stomach (*mNS*) (obtained from the columnar
124 gastric tissue adjacent to the lesion). We also collected samples diagnosed as mixed histology, i.e., with
125 more than one diagnosis as frequently observed in this multifocal disease (Fig. S1B). For example,
126 specimen *M/D* for patient E17 contained both metaplasia and dysplasia.

127

128 After preprocessing, dimension reduction and clustering (Methods), cells clustered mainly by cell type,
129 but some patient/sample-specific variations remained despite our strictly standardized procedure for
130 processing live specimens (Fig. S2A). The Harmony algorithm²⁰ was therefore applied to remove such

131 batch effects (Fig. S2B). The unsupervised cluster analysis of cells produced 40 clusters across the two
132 clinical labels, diagnostic stage (progression phase) and patient. Correlation with reference cell type
133 transcriptomes from the Human Cell Landscape (HCL) database²¹ (Methods) provided “coarse-grained”
134 cell type labels for the majority of cells. Hence, the 40 clusters could be assigned to 16 readily
135 identifiable cell types. The largest group of cells comprised gastro-intestinal (GI) epithelial cells (78K
136 cells), followed by endothelial cells (17.7K), CD8 T cells (17.1K), CD4 T cells (14.3K), and fibroblasts (9.5K)
137 (Fig. 1B-C, Table S2). In the description of this study, marker genes are designated as positively
138 expressed unless explicitly annotated as negative.

139
140 The coarse-grained cell type clusters were then split into “fine-grained” categories representing 37 cell
141 subtype labels (Fig. 1D). For example, the gastro-intestinal (GI) epithelial cells marked by MUC5AC
142 expression were further divided into “functional types” (subtypes) that included goblet cells, chief cells,
143 and foveolar cells. Gastric mucus-producing cells were identified by strong expression of MUC6 (75% of
144 cells). Chief cells were identified by expression of PGC and LIPF, goblet cells through expression of
145 MUC2, TFF3 and SPINK4 and foveolar cells with MUC1, MUC5AC and TFF1²². For metaplasia, cells
146 expressing MUC2 and CDX2 without MUC5AC were termed ‘intestinal metaplasia’²³. The batch-
147 corrected cluster analysis thus correctly prioritized cell subtype over patient and progression phase as
148 the discriminatory cluster feature. Therefore, epithelial cells from nominal dysplasia and tumor samples
149 (*D*, *T*) were intermixed with normal and metaplastic cells in each of the cell type clusters; but the *D*, *T*
150 cells had on average the highest fraction of markers for cell division, consistent with the diagnostic cell
151 labels (Fig. S2 C-D). The lists of gene markers for each cell (sub)type based on statistical differential
152 expression analysis between the clusters are available in Table S3.

153 154 **Transcriptome clusters during progression are predominantly determined by the epithelium**

155 While single-cell transcriptomics allowed for resolving cell type heterogeneity, in order to map cell
156 populations in their entirety to the transcriptome space and derive differential gene expression between
157 progression phases, we computationally created “pseudo-bulk” transcriptomes²⁴ selectively for the
158 coarse-grained cell types of each sample (Methods). Principal Component Analyses (PCA) of pseudo-
159 bulks transcriptomes that included all cell types (mimicking classical bulk RNAseq) failed to show
160 diagnostic separation (Fig. 2A, left panel). However, PCA using only epithelial cell pseudo-bulk
161 transcriptomes were able to group the various nominal histological diagnoses. Indeed, *mNE* samples,
162 primarily inflamed squamous esophageal epithelium, were clearly separated from *M*, *D* and *T* along PC2,
163 with the exception of sample E24A (Fig. 2A, middle left panel). By contrast, and as expected, the *mNS*
164 samples were close to the cluster of *M*, *D* and *T* samples, and, in particular, overlapped with the *M*
165 samples in PC2 dimension, consistent with the current paradigm on Barrett's origin arising from
166 proximal migration of gastric glandular mucosa⁷, but they were still separated in PC3 (Fig. 2A, middle left
167 panel). Overall, the *M* and *D* samples clustered with the *T* samples (Fig. 2A).

168
169 The linear discrimination by PCA lessened, but still remained, when stromal (fibroblast/myofibroblasts/
170 endothelial) pseudo-bulk transcriptomes were used instead of epithelial cells (Fig. 2A, middle right
171 panel). Importantly, there was an intermixing between fibroblast cells from *mNS* with those from *M*, *D*,
172 and *T* samples, suggesting that fibroblast phenotype reflects an early shift from a squamous

173 (esophageal) to a columnar cell context. Immune cell bulk transcriptomes did not discriminate the
174 progression phases as clearly as stromal cells (Fig. 2A, right panel).

175

176 **Global Differential gene expression analysis reveal an immune suppressive stroma and novel** 177 **dysplastic markers**

178 To identify differentially expressed genes (DEGs) between the phases of progression, we used DESeq2²⁵
179 and pseudo-bulk transcriptomes of the coarse-grained cell types (Table S2) (Methods). The largest group
180 of cells, the GI epithelium, revealed the largest number of differentially expressed genes (6874 genes)
181 between tissue diagnoses, followed by endothelial cells (1612 genes), fibroblasts (624 genes) and CD8 T
182 cells (833 genes) (Figs. 2B & S3, Table S2).

183

184 In pathway enrichment analysis^{26,27}, DEGs of fibroblasts, B, Natural Killer (NK) and monocyte-derived
185 cells displayed significant associations for particular pathways (Table S4). For example, fibroblast DEGs
186 were strongly enriched for the functional annotation "TGF-beta regulation of extracellular matrix"
187 (BioPlanet 2019, adj. p-value 6e-17) (Fig. 2C), supporting acquisition of a carcinoma-associated fibroblast
188 (CAF) phenotype. Notably, genes characteristic of this pathway were under-expressed in both *mNE* and
189 *mNS* samples compared to *M*, *D* and *T* samples (Table S4). Supporting pathway analysis, DEG in
190 fibroblasts (increased SMOC1, FBN2, PDE4D and PDE10A in *M* samples; increased GDF15, ANGPTL2, C2
191 in *D* samples; and increased MAP3K5, TMEM158, COCH, TNFSF15, F2RL2, DKK3, BHLHE40, DCBLD1,
192 ITGAV, IL11, WNT2, and FLNA in *T* samples) jointly point to a TGF-beta driven immunosuppressive and
193 fibrotic program.

194

195 Although the goal of this survey was not to weigh in on evidence for the various hypotheses on the cell
196 of origin of BE^{28,29} our scRNAseq analysis confirmed the presence in our *M* phase samples of previously
197 noted "mixed" phenotype (multi-lineage) epithelial cells in conjunction with this question (Fig. S3B-D),
198 including transitional (squamous/columnar) basal progenitor cells (KRT5+/KRT7+)^{7,30} as well as the
199 gastric/intestinal mixed-phenotype cells¹⁵.

200

201 **Cell type composition changes during progression to EAC reflect a shift in tissue identity from** 202 **esophagus to stomach**

203 DEGs between phases can result either from changes in expression of genes in individual cells or from a
204 shift in relative abundance of cell number (cell type composition change). Single cell-resolution
205 transcriptomes permit comparison of samples at the level of the relative abundance of cell types instead
206 of molecular profiles. To evaluate the discriminatory power of this higher-level feature, the similarities
207 of the fine-grained cell type proportions were used to clusters the samples (Fig. S4A). Unsupervised
208 hierarchical clustering grouped the histological phases of samples across patients. Similar to PCA
209 analysis of epithelial pseudobulk transcriptomes (Fig. 2A, middle left panel), all *mNE* samples clustered
210 together, separated from the majority of *mNS* samples (dendrogram in Fig. S4A); in between are clusters
211 of the *mNS*, *M*, *D* and many *T* samples (right portion of dendrogram in Fig. S4A). Importantly, the ratio of
212 epithelium and stromal cell abundance was a major determinant of the large clusters (simplified heat
213 map underneath the dendrogram in Suppl. Fig. S4A). This was further supported by the observation that
214 variation in gene expression was primarily driven by changes in composition of the various epithelial cell

215 types rather than gene expression (cell phenotype) change, since the principal coordinates in Fig. 2A
216 correlated with cell type proportions across samples (Fig. S4B).

217

218 Analysis of specific cell type proportions at each disease phase provided additional insights (Fig. S4C).
219 Thus, *mNS* and *M* samples tended to contain fewer immune cells. Conversely, the *T* samples exhibited a
220 significantly higher proportion of macrophages (1.9-fold) and T cells (1.5-fold) compared to *mNE* (Fig. S4
221 C-D). Interestingly, this feature further set *T* apart from *M*, a difference not exposed by bulk gene
222 expression profiling of immune cells (Fig. 2A). Thus, cell type abundance, used as a feature for clustering,
223 could extract gene $\rightarrow T$. As expected, we observed a decrease of tissue-specific transcripts with
224 increasing malignancy, in line with ric patterns despite sample-specific variability.

225

226 **Changes in the individual cell types and their subtypes during progression**

227 We first examined the epithelial cells and changes of the transcriptional states with progression (*mNE*,
228 *mNS*) $\rightarrow M \rightarrow D$ either differentiation arrest or dedifferentiation in neoplasia which are now considered
229 hallmarks of malignancy³¹. The loss of differentiated cells was specifically manifest in the reduction of
230 expression of differentiation markers, e.g., MUC5AC, FCGBP, CLCA1, MUC6 and KRT20 at the transition
231 from *M* to *D/T* (Suppl. Fig. S4E). Thus, gastric and intestinal differentiation expression programs "faded"
232 in the development from *M* to *D* and *T* as previously observed⁷.

233

234 Among tumor microenvironment cells, the relative proportions of the 6 coarse-grained cell type
235 categories and corresponding transcript profiles changed during progression (Fig. 3). Within each of
236 these 6 groups (fibroblasts, myofibroblasts, endothelial cells, T/NK cells, myeloid cells and B/plasma
237 cells), we also analyzed the finer-grained cell subtypes (e.g., venous, arterial, capillary and lymphatic
238 endothelial cells) by sub-clustering these groups individually into subgroups and quantifying changes of
239 their abundance across disease progression phases (Methods).

240

241 First, within the fibroblasts (marked by DCN and PDGFRA expression), significant changes in cell type
242 proportions were observed (Fig. 3A). Further sub-clustering fibroblasts revealed a subpopulation
243 differentially expressing APDDC1, NTM and COL6A1 that was highly abundant in *mNE* but almost absent
244 in other tissue or progression phases (cyan cluster 3, Fig. 3A). Thus, an esophagus-specific fibroblast
245 population was already lost along with the loss of squamous epithelium at the *M* stage.
246 Correspondingly, the replacement of squamous epithelium by columnar epithelium in BE was
247 accompanied by replacement of APDDC1, NTM and COL6A1-expressing esophagus-specific fibroblasts by
248 PXDN, F3, POSTN-expressing fibroblast subpopulations (clusters 2, 4 and 8, Fig. 3A). These fibroblast
249 subpopulations were absent in *mNE* but appeared in *M*, *D* and *T* tissues. Intriguingly, these fibroblasts
250 that were associated with progression beyond *mNE* were transcriptionally almost identical to those
251 found in matched normal stomach (*mNS*) samples. These fibroblasts would be considered to be CAFs
252 (absent in *mNE*, present in *T*). Yet they were not "abnormal" *per se* but rather represented a cellular
253 reprogramming to a state very similar to that utilized by the non-neoplastic nearby gastric tissues (*mNS*).
254 We also confirmed a previously reported subpopulation of PI16-expressing "pan-tissue" fibroblasts
255 (cluster 0, Fig. 3A)³² that appeared to be stable across all specimens and progression phases.

256

257 Next, we examined the myofibroblast compartment (expressing ACTA2, PDGFA and NOTCH3). We found
258 subpopulations resembling vascular smooth muscle cells (clusters 1, 3 and 4, Fig. 3B)³³, pericyte-like
259 cells characterized by COL1A1, COL4A1, RGS5 and CD36 expression (clusters 0, 5 and 6, Fig. 3B) and a
260 cell subpopulation expressing pro-inflammatory cytokines, such as CCL2, CCL19, CCL21 and CXCL12
261 (cluster 7, Fig. 3B). Proportions of these subpopulations remained stable between *mNE*, *mNS*, *M* and *D*
262 samples. The number of pericyte-like cells increased substantially in *T* samples (3.5-fold compared to
263 *mNE*), a trend also observed in gastric cancers³⁴. This stromal subtype however was not tumor-
264 specific, as it was also found in all other stages albeit in relatively small amounts. While
265 neovascularization in tumor tissues produces abnormal vasculature devoid of pericytes, signaling from
266 these mural cells to endothelial cells is thought to be critical for promoting tumor angiogenesis^{35,36} and,
267 after injury, pericytes have been shown to detach from endothelial cells and transition to pro-
268 tumorigenic, inflammatory myofibroblast-like cells³⁷.

269
270 Within the endothelial compartment, we identified four prominent subpopulations, corresponding to
271 arterial (compared to other endothelial subclusters, differentially expressing HEY1 and SEMA3G), venous
272 (ACKR1), capillary (VWA1, PLVAP) and lymphatic (CCL21) endothelial cells³⁸⁻⁴⁰ (Fig. 3C). Whereas all
273 subpopulations were present at each progression phase, we observed a significantly higher proportion
274 of capillary endothelial cells (EC) in *T* and *mNS* compared to *mNE*, again revealing a change in tissue
275 identity during EAC progression that shifts the entire tissue, as a unit, towards the phenotype of
276 matched gastric tissue (*mNS*) (Fig. 3C). Furthermore, the frequency of a particular subpopulation of
277 venous endothelial cells (VEC, cluster 2, Fig. 3C) and lymphatic endothelial cells were also lower in *T* and
278 in adjacent *mNS*. VEC are the cellular source for capillary endothelium during angiogenesis⁴¹, and their
279 reduction along with the increased number of capillary EC may reflect depletion of VEC due to ongoing
280 angiogenesis in the tumor. Similarly, the low number of lymphatic endothelial cells in *T* is in line with the
281 general absence of lymphatics within tumors (although tumor-marginal lymphatics are critical for
282 lymphatic metastasis)^{42,43}. However, since these vasculature remodeling features seen in *T* were also
283 found in the non-cancerous *mNS*, we cannot rule out that this may reflect an intrinsic property of gastric
284 mucosa that distinguishes it from the squamous epithelium of matched normal esophagus that would
285 be co-opted during EAC progression.

286
287 Marked changes of cell type composition in the immune compartment of the tumor microenvironment
288 were revealed by single-cell transcriptomics of the various phases of progression although immune-cell
289 specific bulk transcriptomes were not a discriminatory feature (Fig. 2A, right panel). Among T cells and
290 NK cells, we identified cytotoxic T cells (CD8A), T-helper cells (CD4), T-regulatory cells (FOXP3) and
291 different subtypes of NK cells (GNLY) (Fig. 3D). Most of these subpopulations were stable across the
292 progression phases with the exception that *mNS* tissues had reduced levels of T-regulatory cells (cluster
293 3, Fig. 3D) and displayed slightly higher numbers of cytotoxic T cells compared to the squamous *mNE*.
294 Interestingly, *M* samples exhibited a sizable increase in NK cells, notably of the NCAM1(CD56^{high})
295 immunosuppressive subtype^{44,45} (cluster 5, Fig. 3D; FCGR3A, FCGR3B, NCAM1/CD56, NCR1) and a
296 decrease in T-helper cells (cluster 1, Fig. 3D), which jointly indicated acquisition of an
297 immunosuppressive environment in metaplasia.

298

299 In the myeloid compartment, scRNAseq readily identified macrophages (MSR1, TREM2), monocytes
300 (VCAN, S100A8), dendritic cells (PPA1, RUNX3) and neutrophils (FCGR3B, CSF3R) (Fig. 3E). Neutrophils
301 were abundant in both *mNE* and *mNS* samples (Fig. 3E), but their frequency was significantly lower in *D*
302 and *T* samples. Furthermore, as mentioned, there was a significant increase (3.2-fold) in macrophages in
303 *T* samples (Fig. 3E). The frequencies of monocytes and dendritic cells were constant across disease
304 progression phases.

305

306 Both B (MS4A1) and Plasma (JCHAIN, IGHA1) cells were present at all disease progression phases (Fig.
307 3F). Notably, *mNE* samples showed abundant B cells but contained few plasma cells. With the onset of
308 metaplasia, the fraction of B cells decreased significantly, while the fraction of plasma cells increased
309 substantially, a finding that has been previously associated with outcome of EAC⁴⁶.

310

311 **scRNA-seq analysis reveals large CNVs in the dysplastic phase and patient-unique clonal history of** 312 **malignant cells**

313 Genomic instability, manifested as copy number variants (CNVs), is a hallmark of EAC. Appearance of
314 CNVs in BE has been considered an early biomarker for progression^{10,47}. To both identify aneuploid cells
315 and estimate clonality, scRNA-seq reads were used to estimate CNVs in each cell⁴⁸.

316

317 For all scRNAseq samples, we inferred CNVs in epithelial cells using inferCNV (Methods) with matched
318 normal samples (*mNE/mNS*) as reference. As expected, tumor samples contained a substantial number
319 of epithelial cells with CNVs (Fig. 4A-B) not found in stromal cells (Fig. 4B). Dysplastic samples contained
320 cells with CNV profiles similar to cells from the corresponding tumor, suggesting a clonal relationship
321 between dysplasia and tumor (Fig. S5A-B). Most tumors contained one major copy number profile,
322 indicating that the cells were clonally related. No large-scale CNVs were seen in metaplastic samples.
323 Only two samples diagnosed as metaplasia exhibited small amounts CNV. However, these exceptions
324 were probably due to contamination with dysplastic and tumor cells (data not shown). Of note, any
325 small-scale CNVs in metaplasia could be undetectable given the genomic resolution limit (>10MBp) of
326 the methodology.

327

328 To confirm scRNAseq-inferred CNVs, we performed single-cell whole exome DNA sequencing on
329 selected samples. Comparison of CNV profiles from E21 tumor, either inferred from scRNAseq (Fig. 4C)
330 or obtained from the matched scDNAseq sample (Fig. 4D), revealed good agreement. Both methods
331 detected the same major clones: the first clone was characterized by chr1.q and Chr8 copy number gain,
332 and by chr5 deletion (red CNV cluster, Fig. 4C-D); the second clone showed copy number gains of chr7
333 and chr8.q and deletions of chr4 and chr8.p (green CNV cluster, Fig. 2C-D). scDNAseq did not identify a
334 third clone (blue CNV cluster in Fig. 2C), possibly due to the limited number of cells used for scDNAseq.

335

336 The copy number profiles of each patient's tumor were unique and manifested as distinct transcriptional
337 clusters of epithelial cells (color-coded clusters in Fig. 4E) which dominated the interpatient
338 heterogeneity observed in the tumor epithelial cells. In summary, our observations showed that in our
339 small cohort, large-scale copy number variation arose at the dysplastic phase, consistent with previous
340 findings^{10,49,50}.

341

342
343
344
345
346
347
348
349
350
351
352
353
354
355
356
357
358
359
360
361
362
363
364
365
366
367
368
369
370
371
372
373
374
375
376
377
378
379
380
381
382
383

Changes in extracellular matrix (ECM) composition during progression mirror concerted epithelial and stromal cell changes

The extracellular matrix (ECM) is central to the molecular and mechanical interaction between epithelial and stromal cells. We used mass spectrometry to examine ECM composition in a subset of the 12 patients for whom we had single-cell transcriptomic data (Fig. 1A, see Methods), focusing on comparison between *mNE* and *T*: 6 tumor samples (*T*) and 4 patient-matched normal esophagus samples (*mNE*) (Fig. S1A). In the ECM-enriched material purified from these samples, 1994 protein groups with at least two unique peptides were quantified by mass spectrometry, roughly half of which were categorized as “extracellular” proteins. Among them 78 were core matrisome proteins and 73 were matrisome-associated proteins (Fig. 5A). Principal component analysis of the samples based on the proteomic profiles showed separation between *T* and *mNE* samples (Fig. 5B).

Comparing pooled *T* versus *mNE* samples, we found 98 proteins with significantly altered abundances in the ECM-enriched extract (q -value < 0.001 and $|\text{fold change}| > 1.5$). 55 of them showed decreased and 43 increased expression in *T* compared to *mNE* (Fig. 5C). The 10 proteins with the most dramatic changes (9 “down-regulated” and 1 “up-regulated”), as well as a 22-protein matrisomal core protein signature, are presented in Fig. S6. The decrease in ECM protein expression during progression from *mNE* to *T* was predominantly represented by some specific collagens, in line with the reduction in collagen-producing fibroblasts in *M*, *D* and *T* compared to *mNE* observed in the scRNAseq dataset (Fig. 3A, fibroblast cluster 3)⁵¹. As expected, expression of keratins associated with the squamous *mNE*, also decreased during progression to *T*. Conversely, *tumor associated* ECM had increased levels of proteoglycans PRG2 and PRG3 as well as fibrinogens FGA, FGB and FGG (Table S6).

Integration of scRNAseq and proteomics reveal cellular sources of ECM protein changes

We next examined whether scRNAseq findings were consistent with those of ECM proteomic analysis for the 10 patient samples analyzed by both methods (Fig. 5D). scRNAseq could provide information about the cellular source(s) of the 98 ECM-associated proteins (Fig. 5E) with significantly altered abundance in *T* vs *mNE*. As Fig. 5D shows, relative ECM protein abundances (fold-change in *T* vs. *mNE*) for this set of proteins (Fig. 5C) correlated well with the fold changes of transcripts computed as pseudo-bulk expression from the equivalent patient samples (Spearman $R=0.73$).

Specifically, scRNAseq linked changes in protein abundances at the tissue level to shifts in specific cell types/subtypes that produced them. For instance, mRNA expression of collagens 6A1, 6A2 and 6A3 was reduced in *T* samples, a phenotype that was consistent with the loss of fibroblast subtypes that strongly expressed transcripts encoding these same ECM molecules during progression (cluster 3, Fig. 3A). The marked reduction in collagen 14A1 in the ECM proteomic analysis could also be explained by the observed shift in fibroblast subtype fractions, as transcripts for COL14A1, while expressed in *mNE* fibroblasts, were no longer expressed in matched normal stomach (*mNS*) fibroblasts, the fibroblast subtype that became predominant at the *M* phase and subsequent *D* and *T* phase (Fibroblast clusters 2, 4 and 8, Fig. 3A).

384 Notable departures from the correlation between ECM proteomics and scRNAseq included fibrillin
385 (FBN1) whose protein abundance increased but whose transcript levels decreased instead. This
386 discordance might be explained by its predominant expression in adipose tissue, a tissue compartment
387 represented in the proteomic analysis but totally absent in single-cell transcriptomics because
388 adipocytes are lost during the cell dissociation process⁵². Similarly, the relatively high abundance of the
389 two proteoglycans, PRG2 and PRG3, in tumor ECM was not concordant with transcript analysis which
390 showed no expression in *T* and *mNE*. This finding is consistent with the predominant production of these
391 proteoglycans in liver and bone marrow (and in female reproductive organs) and suggest that these
392 proteins may have been deposited via circulation in the esophagus tumor stroma⁵³. Similarly,
393 fibrinogens FGA and FGB, which are solely produced in the liver, were also unexpectedly elevated in the
394 tumor ECM proteome of several patients but not in the corresponding tumor transcriptome⁵⁴, pointing
395 again to the synthesis of fibrinogen in the liver and subsequent deposition at the tumor site. Strikingly,
396 concordance between fibrinogen proteome and transcriptome was observed for one patient (E14). This
397 concordance between fibrinogen protein and local transcripts could be explained by the rare but
398 previously reported occurrence of hepatoid differentiation (documented by identification of an alfa-
399 fetoprotein (AFP)-expressing cluster) of the EAC of this patient.

400
401 Examining cellular sources confirmed that one major protein absent in the tumor ECM-enriched extract,
402 KRT13 (Fig. 5C, Suppl. Table S6), a keratin filament protein characteristic of stratified squamous
403 epithelium, resulted from the replacement of the esophagus squamous epithelium by a gastro-intestinal
404 columnar epithelium (Fig. 5E). Another protein of interest was periostin (POSTN), an ECM protein that
405 was moderately but significantly increased in the tumor ECM (Fig. 5C, Table S6). Cell-type specific
406 transcript analysis (Fig. 3A) had shown that it was a prominent marker of a subtype of fibroblasts
407 associated with gastric tissue, and characteristic of progression from *mNE* to *M*, *D*, and *T* (fibroblast
408 clusters 2, 4 and 8, Fig. 3A). Tumor transcript analysis in the pseudo-bulk data (Fig. 5D) failed to detect
409 an increase in transcripts of POSTN in this comparison, although it has been previously implicated in
410 BE^{15,55}. However, single cell-resolution analysis showed that, while POSTN transcripts were elevated by
411 almost two-fold in tumor-associated fibroblasts, in this same sample set, the tumor capillary endothelial
412 cells (Fig. 3C), showed instead a down-regulation of POSTN by more than two-fold (Fig. S7A-B). Thus, a
413 shift of transcript levels for a given gene in opposite directions in distinct cell types/subpopulations
414 might conceal differential expression in bulk RNAseq (Fig. S7A-B).

415
416 Finally, among the most significantly increased non-ECM proteins in the ECM-enriched preparation of *T*
417 compared to *mNE* samples (Table S6), were Ig-related subunit chains IGHA2 and IGKC (Fig. 5C). This
418 increase could readily be attributed to the surge of plasma cells in *T* compared to *mNE*, consistent with
419 the cell-type composition changes noted above (Fig. 3E)^{46,56,57}.

420
421 Taken together, scRNAseq and cell type-level resolution analysis not only allowed us to trace back the
422 cellular origin of changes observed in bulk analysis methods, such as proteomics, but also allowed us to
423 expose opposing expression changes in distinct cell type compartments that might have masked a cell-
424 type specific differential expression.

425

426 **Changes in mechanical stiffness during progression confirm concerted epithelial and stromal**
427 **alterations**

428 Since ECM changes have been linked to altered mechanical tissue stiffness, which in turn can affect
429 tumor-promoting signaling⁵⁸, we used atomic force microscopy (AFM) to assess the stiffness of
430 esophageal tissues during disease progression by comparing AFM characteristics of samples across
431 disease progression phases for epithelial and stromal stiffness (Fig. S8A-B). Stiffness measurements of
432 epithelium were found to be in a range similar to those previously published (0.6-3.0 kPa)⁵⁸⁻⁶⁰ (Fig. 5F).
433 Strikingly, stiffness of the *mNE* (squamous) epithelium was ~20-times higher than that of *mNS*
434 (columnar) epithelium (1.2 vs. 0.06 kPa).

435
436 Metaplastic Barrett's esophagus (*M*) not only acquired a gastric histology but also a "softer" gastric-like
437 stiffness. However, as expected, this lower gastric-like stiffness increased with pathological progression.
438 Although the stiffness of epithelia in the columnar lesions *M*, *D*, *T* was 3-8 times lower (0.15, 0.4 and
439 0.45 kPa, respectively) compared to that of the squamous *mNE*, stiffness of these gastric-like columnar
440 lesions was still 3-8 times higher than that of normal tissue, *mNS* (Fig. 5F). Thus, while the esophageal
441 columnar lesions adopted a softer gastric-like identity, their stiffness was still significantly higher than
442 that of the non-cancerous *mNS*. This observation is in accordance with the well-documented general
443 concept of increased stiffness in diseased/cancer tissue compared to healthy tissue⁶¹.

444
445 AFM analysis also revealed mechanical changes in the stroma. Consistent with the difference in
446 epithelial type, stiffness of the stroma of *mNE* esophagus (~0.6 kPa) was dramatically higher than that of
447 *mNS* (~0.04 kPa) (Fig. 5F). However, in most samples, the stroma of the columnar lesions *M*, *D*, *T* was
448 similar or only slightly softer than that of *mNE* (0.24-0.26 kPa vs. 0.6 kPa), with large variation between
449 samples; some regions exhibited much higher stiffness, reflecting the general trend of neoplastic tissues
450 (Fig. 5F). The moderate decrease in stromal stiffness that correlates with replacement of squamous by
451 columnar tissue during progression was in accordance with the observed decrease in ECM proteins, such
452 as laminin and prolargin, as well as stromal cell cytoskeletal proteins that link cell mechanics to the ECM
453 (e.g. desmin, calponin, dystrophin, and filamins A and C), as identified by the ECM proteomics (Table S6).

454
455 **Multiplexed protein imaging reveals reorganization multi-cellular tissue neighborhood during**
456 **progression**

457 To interrogate the spatial relationships of the cell types within the progression phase of EAC, we
458 performed CODEX multiplexed protein imaging on 27 imaging regions in the esophageal tissue from 5 of
459 the 12 patients (Fig. 6A, Fig. S9A)⁶²⁻⁶⁴. Diagnosis of tissue and phase of progression (*mNE*, *M*, *D*, *T*; *mNS*)
460 was verified by pathologists with regard to proportions of cells using H&E (hematoxylin and eosin)
461 staining of the same sections post-CODEX (Fig. S9B-D, Table S8). Given our focus on stroma, we designed
462 our 54-antibody panel to interrogate epithelial, stromal and immune cell types (Table S9). The CODEX
463 marker panel allowed us to identify 45 unique cell types (Fig. S9E), 25 of which were epithelial⁷,
464 including "squamous" (*mNE*), "foveolar" (*M*), p53+ (p53-expressing) and lineage-negative epithelial cells
465 (*D*, *T*) (Fig. 6B,E, Fig. S9F), which were consistent with the overall change in cell type proportions seen in
466 the scRNAseq (Fig. S10).

467

468 Because CODEX preserves tissue geography, we next asked if spatial proximity of cell types to one
469 another was altered during disease progression in light of the dramatic changes in cell type composition
470 observed by scRNAseq (Figs. 2 and 3). Thus, we performed cellular neighborhood (NH) analysis to
471 identify conserved multicellular microstructures (Methods)⁶⁵ and expose changes in tissue organization
472 not observable by shifts in global cell proportions using scRNAseq. We identified 24 unique multicellular
473 neighborhoods that were labeled based on enrichment of cell types within each neighborhood (Figs. 6C
474 and S11A-B). For example, as expected, *mNE* samples were highly enriched for an “*apical squamous*” NH
475 - characterized by Annexin A1+ squamous cells - and for a “*basal squamous*” NH - characterized by both
476 Annexin A1+ and p63+ squamous cells (Fig. S11C,D).

477
478 We also detected a NH enriched for foveolar and goblet cells (Fig. S11B, F-G) that we termed
479 “*specialized*” NH, consistent with previously defined gland phenotypes in metaplasia⁶⁶. As expected, this
480 “*specialized*” NH correlated with the percentage of metaplastic epithelium (Fig. 6D, Fig. S12A). We also
481 detected NHs that were consistent with known epithelial organization (e.g., “*mature intestinal*” NH,
482 “*oxynto-cardiac*” NH, “*atrophic cardiac*” NH). In addition, we identified novel conserved NHs (e.g.,
483 “*muc5low specialized*” NH, “*muc6low mature intestinal*” NH) characteristic of BE epithelial organizations
484 (Figs. S12A and S13A). Analysis of neighborhoods allowed us to assign specific molecular alterations of
485 malignant cells to this higher-level pattern of tissue organization. For instance, the “*p53hi atrophic*
486 *cardiac*” NH correlated with the proportion of metaplastic epithelium, attributing p53 expression to
487 particular glands (Figs. S12A and S13A).

488
489 In the stroma, we identified several consistent neighborhood organizations (e.g., a “*stroma and*
490 *immune*” NH, a “*stroma and neutrophil*” NH, and a “*follicle, smooth muscle, vasculature*” NH).
491 Interestingly, presence of the “*stroma and neutrophil*” NH correlated with the proportion of epithelium
492 classified independently as high-grade dysplasia by two expert pathologists across all samples (Fig.
493 S11E). This NH also was enriched for CD4+ T cells, lymphatic and vascular endothelial cells, and antigen-
494 presenting cells (Fig. S11B).

495
496 **Communities of cell neighborhoods illustrate rearrangements of epithelial-stromal cellular entities**
497 **during progression**

498 Multiple NHs correlating with the specific histological phase of BE progression (*M*, *D*) suggested that the
499 size of an effective cellular neighborhood structure was smaller than the larger overall pathology that
500 underlies the histological diagnosis. This feature is reflected in the unique NH calls for cells of a single
501 gland and in the local stromal NHs for a given histological pathology (Fig. 6E). To better align
502 multicellular structures to the overall histological diagnosis, we thus evaluated the co-localization of
503 multiple NHs, referred to as “communities” (of neighborhoods). We defined specific communities of NHs
504 by increasing the number of neighborhood-defining cells (100), using the NH labels as input⁶⁷. This
505 process revealed a total of 10 unique communities (C) of neighborhoods (Fig. S12B-C). Thus, the “*apical*
506 *squamous*” NH and “*basal squamous*” NH were found within a single “*squamous epithelial community*
507 (C)” because of their characteristic occurrence in proximity to each other (Figs. 6F & S12B). The presence
508 of the “*squamous epithelial C*” correlated across all samples with the percentage of squamous
509 epithelium (Fig. 6G). Three other communities of NH showed positive correlations with the proportion

510 of epithelium: “*Specialized and Mature Intestinal C*” with M, “*Inflamed Dysplasia C*” with D and
511 “*inflamed mature intestinal C*” with T (Fig. 6G).

512

513 The relationship of community structures with the phases of progression afforded a new looking glass
514 for considering tissue geography in the cellular changes associated with BE progression by analyzing
515 cellular composition of communities instead of the global composition as captured by scRNAseq (Fig.
516 6H-J, Table S10). Overall, this analysis revealed an increase in immune and mesenchymal cells in the
517 communities with progression.

518

519 Within the epithelial cell compartment, with progression the squamous cell community (“*squamous*
520 *epithelial C*”) yielded to the foveolar community (“*Specialized and Mature Intestinal C*”) that increased in
521 epithelial cells that were negative for squamous and metaplastic lineage markers (Figs. 6H, S9E & S12D)
522 reflecting changes both at the level of glandular structures, towards gastro-intestinal formations, as well
523 as loss of cellular differentiation associated with progression.

524

525 Within the immune cell compartment, the proportion of neutrophils increased within the “*inflamed*
526 *dysplasia C*” (Figs. 6I & S12E). Indeed, three of the neutrophil-enriched NHs were specifically enriched
527 within the “*inflamed dysplasia C*” (Fig. S12F). Strikingly, while most immune cell types also increased
528 within the “*inflamed mature intestinal C*”, which correlated with invasive epithelium or tumor
529 pathology, neutrophils did not. Instead, macrophage subsets were enriched (Figs. 6I & S12G). This
530 “*inflamed mature intestinal C*” was enriched with diverse NHs, namely the “*mature intestinal and*
531 *immune*” NH, the “*APC enriched immune*” NH, and the “*stroma and immune NH*” (Fig. S11B). Each of
532 these NHs were characterized by abundance of immune cells (e.g., CD4+ T cells, macrophages, DCs,
533 CD8+ T cells) and absence of neutrophils. Finally, in this “*inflamed mature intestinal C*”, the proportion
534 of CD4+ Tregs also increased (Figs. 6I, S12I & S13H). This trend may reflect the role of Tregs in
535 preventing neutrophil accumulation during tissue repair⁶⁸.

536

537 Analysis of mesenchymal cells in communities revealed that the CD36hi endothelial cell population was
538 robust in the “*specialized & mature intestinal C*” (*associated with metaplasia*) but reduced in the
539 “*inflamed dysplasia C*” and “*inflamed mature intestinal C*” (Fig. 6J). Interestingly, the abundance of
540 CD36hi endothelial cells within all samples negatively correlated with the abundance of CD4+ Tregs (Fig.
541 S12J). This negative correlation was in accordance with the opposite phenotypes of a CD36hi anti-
542 tumorigenic state and a CD4+ Treg high immunosuppressive, pro-tumorigenic state. This finding
543 underscores the added value of evaluating cell proportion changes with structural guidance of cell
544 communities and is consistent with the downregulation of CD36 in chronically-inflamed tumor stroma⁶⁹.

545

546 **Cell type combinations in cell-cell interactions in stroma reprogramming during progression**

547 We next exploited the spatial NH information to examine cell-cell interactions (Figs. 6K & S13A-C, Table
548 S11). To evaluate the enrichment of cell-cell interactions in particular progression phases (M, D, and T),
549 we calculated the frequency of neighbors using a nearest neighbor approach and compared the
550 frequency of occurrences to null-models, achieved by 10,000 permutations of cell type locations
551 (Methods). Cell-cell interactions shared by all phases included those between immune cells (CD8+ T cell,
552 “M1” macrophage, and plasma cell) and stroma cells (Fig. S13D). This was consistent with the increase in

553 plasma cells across all disease phases observed with CODEX (Fig. S13E) and scRNAseq (Fig. 3F). Plasma
554 cells are normally seen within mucosal areas of the intestine and form a conserved niche⁶⁷. Thus, the
555 increase in plasma cells (Fig. 6I) and the identification of a specific “*plasma cell enriched*” NH (Fig. S11B)
556 may represent an aspect of reprogramming of the stromal environment.

557

558 Many unique interactions involving foveolar cell type were enriched in BE (Fig. 6K). For instance, in *M*,
559 but not *D* or *T* samples, foveolar cells were found next to the CD36hi endothelial cells and to nerves
560 (Figs. 6K-L & S13F), in line with their enrichment within the “*specialized & mature intestinal C*” (Fig. 6I).
561 Additionally, in both *M* and *D*, foveolar cells were found close to CD4+ T cells and plasma cells (Figs. 6M-
562 N & S13G-H), consistent with plasma cell niches known to accompany intestinal epithelial transitions.
563 Finally, we observed that neutrophils paired with lymphatic cells, endothelial cells and M1 macrophages
564 in *D* and *T* (Figs. 5M-N & S13I).

565

566 **Epithelial and stromal cellular communities become increasingly diverse during progression**

567 Communities associated with BE progression had altered proportions of both epithelial and stromal cell
568 types (Figs. 6H-J & S12C-G, Table S10). Indeed, the diversity of gland structures has been shown to be
569 associated with progression in BE⁷⁰. However, our analysis also took into account the stromal
570 component. We quantified the diversity of cell types in communities using the CODEX markers (Fig. 6O)
571 and found an increase in Shannon’s diversity index H in the communities associated with progression:
572 $H(\text{“squamous epithelial C”}) < H(\text{“specialized & mature intestinal C”}) < H(\text{“inflamed dysplasia C”}) <$
573 $H(\text{“inflamed mature intestinal C”})$ (Fig. 6O). This pattern indicated that areas with high (chronic)
574 inflammation and lacking well-differentiated structures were more likely associated with invasive
575 tumors.

576 **DISCUSSION**

577 In this study, we describe concomitant epithelial and stromal changes occurring during progression from
578 a premalignant state (BE) to invasive cancer (EAC). This was made possible by analyzing 64 tissue samples
579 collected from 12 individual patients that represent the sequential histological phases of BE progression
580 from matched “normal” esophageal tissue (*mNE*), to Barrett’s metaplasia (*M*), dysplasia (*D*) and invasive
581 adenocarcinoma (*T*) in the same patients. The matched normal stomach tissue (*mNS*) constituted a key
582 reference because BE is the adaptive acquisition of a gastric/intestinal-like tissue. The disease
583 progression phases co-occur within the same patient and thus can, to some extent, be regarded as a
584 progression trajectory. Our data show marked phase-specific alterations shared by the twelve patients
585 at multiple size scales, with respect to transcriptome, cellular content, large-scale CNVs, ECM proteomic
586 profile, tissue mechanics, and histological architecture, with some patient-specific variability. Our
587 studies underscore the importance and highlight new opportunities of not only multi-omics but also
588 multi-scale integrated analysis.

589

590 A major insight is that, despite absence of obvious histological alteration in the stromal compartment,
591 the stroma also underwent, from early in progression (*M* phase), drastic changes in cellular, mechanical
592 and molecular identity and tissue organization that complemented those seen in the epithelium. The
593 multi-scale approach enabled a combined assessment of change at the levels of cell numbers (cell type

594 proportions) and cell states (molecular cell subtype) which affected epithelial cells, fibroblasts,
595 endothelial cells, immune cells, acting in concert during advancement to malignancy and revealed wide-
596 spread and coordinated non-genetic cell plasticity.

597

598 A key finding was the early loss of esophagus-type and gain of gastric-type fibroblast subpopulations
599 with onset of epithelial metaplasia (BE) and in ensuing progression. Thus, the epithelial change from
600 squamous to columnar ($mNE \rightarrow M$) was accompanied by a commensurate transition from squamous-
601 supporting fibroblasts to columnar-supporting fibroblasts (Fig. 3A); this shift was robust enough to
602 separate mNE from $mNS/M/D/T$ in PCA space based on pseudo-bulk transcriptomes of stromal cells (Fig.
603 2A). This result is consistent with concerted changes of epithelium and stroma as one unit in the tissue
604 trajectory of healthy to premalignant and malignant tissue. Besides acquiring a gastric identity upon
605 transition to M and later to D and T , these fibroblasts also acquired characteristics previously
606 documented in carcinoma-associated fibroblast (CAF) populations, i.e., expression of TGF-beta targets⁷¹.
607 Most investigators believe that tumor cells program fibroblasts into pro-tumorigenic CAFs. However,
608 substantial data suggest that pro-tumorigenic fibroblasts may already be present before development of
609 a tumor^{69,72}. Our analysis of these esophageal samples at single-cell resolution confirmed this
610 observation. The origin of these pro-tumorigenic fibroblasts is intensely speculated. The presence of
611 pro-tumorigenic fibroblasts in BE may simply reflect the outgrowth of gastric tissue as one epithelium-
612 stromal unit or it may involve the migration of gastric fibroblasts. Alternatively, presence of the latter
613 may reflect a cell-level state transition (i.e., transdifferentiation) of local esophageal fibroblasts originally
614 supporting the squamous epithelium during progression or a reprogramming of progenitor (fibroblast)
615 cells. Finally, recent studies have demonstrated the transition of injured pericytes to a CAF-like state
616 that are pro-tumorigenic³⁷.

617

618 The shift in fibroblast subpopulation occurred early at the $mNE \rightarrow M$ transition (Fig. 3A). This might
619 entertain the interpretation that stromal changes precede and possibly drive epithelial transformation
620 to malignancy⁷³. Ongoing analyses on patients diagnosed with BE but who, unlike the patients in his
621 study, have not progressed to dysplasia or carcinoma will allow us to discriminate between events
622 already occurring at the BE disease phase in the absence of malignancy from events occurring in a BE
623 which has been subjected to a potential tissue field effect by the neighboring tumor. It should also be
624 noted that tissue plasticity described at these early stages of disease occurs in the absence of major
625 mutational or genomic alterations and thus represent examples of non-genetic plasticity in all tissue
626 components.

627

628 To more explicitly demonstrate the added value of single-cell resolution compared to bulk (whole
629 sample) analysis and explore a multi-scale analysis, we generated pseudo-bulk transcriptomes from the
630 scRNAseq data and compared samples as wholes or selectively, with respect to specific cell types. This
631 analysis showed that, at the whole tissue level, clustering of histology-based diagnosis (disease phases)
632 and corresponding disease progression phases was most obviously associated with changes in the
633 epithelium. However, extending previous reports emphasizing the role of stromal and immune cells in
634 tumor progression, our study shows that single-cell resolution, let alone the cells' spatial configuration,
635 must also be considered for discriminating disease phases and courses.

636

637 Analysis of ECM-enriched proteins with progression to tumor was in great part accompanied by
638 corresponding gene expression changes in epithelial and stromal cells. Integration with scRNAseq
639 pinpointed the cellular source down to the granularity of sub-cell types. The increased transcript
640 expression in *M*, *D*, *T* fibroblasts of periostin (POSTN), a developmental ECM protein overexpressed in
641 many tumors⁷⁴, was also increased in the ECM-enriched proteome of *T* samples compared to *mNE* (Fig.
642 5C). The scRNAseq data (Figs. 3A and 5E) readily attributed its source to the particular subpopulations of
643 fibroblasts that were shared by matched normal gastric samples (*mNS*). Interestingly, this change of
644 expression was partially compensated by a decrease in expression by endothelial cells at more advanced
645 phases of progression (Fig. S7A-B).

646
647 Similarly, the marked decrease in expression of some types of collagens in EAC tissues was in accordance
648 with a shift in the subtype of fibroblasts associated with *T* compared to those in *mNE* samples (Fig. 5A).
649 The granular cell-type level resolution of our analyses allowed us to fully appreciate the complexity of
650 such stromal changes, underscoring the importance of the specific cellular source for a change in
651 abundance of a protein in the bulk tissue. Thus, despite the net decrease in collagen-6 protein that could
652 be attributed to a loss of squamous epithelium-associated fibroblasts, this decrease was accompanied
653 by selective increased transcript expression in myofibroblasts (Fig. S7A). This apparent discordance
654 epitomizes the concerted changes in multiple cell types that converge to a pro-tumorigenic tissue
655 landscape. Indeed, whereas COL6-deficient fibroblasts would no longer assemble and maintain a
656 homeostatic ECM, the collagen-6-expressing myofibroblasts would instead drive inflammation and
657 fibrosis via endotrophin, the proteolytic bioactive product of collagen 6^{75,76}. These COL6-positive
658 myofibroblasts would correspond to the previously described dermoplastic fibroblasts found in
659 melanoma⁷⁷ and BE¹⁵.

660
661 The molecular changes in ECM and cells observed during progression was also manifest in the parallel
662 alteration of mechanical properties of both epithelium and stroma. The reduced epithelium stiffness
663 associated with the switch from squamous to gastric tissue is in agreement with the reported
664 progressive decrease in AFM stiffness in metaplastic CP-A (3.1 kPa) and dysplastic CP-D (2.6 kPa)
665 esophageal epithelial cell lines compared to that of the squamous esophageal epithelial EPC2 cell line
666 (4.7 kPa)⁷⁸, but also in the stroma albeit to a lesser more varied extent. However, progression from *M* to
667 *T* still kept the tissue stiffer than that of inherently softer non-cancerous *mNS* gastric tissue (Fig. 5F), in
668 line with the often observed increase in tissue stiffness in malignancies, which in turn feeds back to
669 modulation of gene expression, including genes that control ECM composition. This mutualism between
670 cellular programs and tissue mechanics underscores the importance of joint analysis of molecular,
671 cellular and mechanical changes^{78,79}.

672
673 Our study also highlighted the importance of considering cell (sub)type abundances as quantitative
674 observables (Fig. 3), illustrated by: (i) the gain of a gastric-specific fibroblast population (Fig. 3A, clusters
675 2 and 4) at the expense of an esophagus-specific fibroblast population (Fig. 3A, cluster 3) discussed
676 above; (ii) a dramatic over-representation of pericyte-like cells (Fig. 3B, clusters 0, 5 and 6) occurring
677 late, i.e. only at the tumor stage; (iii) a similar delayed over-representation of VWA1 and PLVAP-
678 expressing endothelial cells (Fig. 3D, cluster 0), two ECM proteins involved in the formation of the
679 stomatal and fenestral diaphragms of blood vessels; (iv) an early and drastic decrease in neutrophils

680 expressing genes of phagocytic and bactericidal function (Fig. 3E, clusters 3 and 7); and (v) a drastic loss
681 of B cell predominance over plasma cells seen in *mNE* but not in *mNS*, and at all phases of progression
682 (*M*, *D*, *T*) (Fig. 3F).

683

684 The combined analysis at various size scales of tissue geography enabled by CODEX afforded a new lens
685 through which hitherto unseen tissue organizational changes during progression become visible (Fig.
686 6P). The identification of consistent cell neighborhoods (NH) and communities (C) of NHs allowed us to
687 quantify changes in the number of cells of particular types (e.g., POSTN^{hi} fibroblasts, CD36^{hi} endothelial
688 cells, p53+ epithelial states) within distinct structures, exposing differentials lost by averaging over large
689 areas. In addition, these structures themselves change in number with progression. For instance, the
690 reduction in neutrophils and concomitant increase in Tregs within the same cell community during EAC
691 progression could not be detected at the global tissue level by scRNAseq. Such changes are of high
692 biological significance, given that the role of Tregs in tissue repair is in part mediated by suppression of
693 neutrophils⁸⁰. The identification of specific multicellular neighborhoods in metaplastic epithelium was
694 consistent with previous descriptions of distinct glandular structures found within BE⁷⁰.

695

696 Shifts in cell state during disease progression from *mNE* to EAC revealed the establishment of an
697 immunosuppressive tumor microenvironment permissive for malignant progression^{81,82}.
698 Aforementioned POSTN expression, first appearing in *M* fibroblasts has been proposed to serve as a
699 biomarker for BE progression⁵⁵ and is implicated in immunosuppression in the TME⁸³. Furthermore,
700 other highly differentially expressed genes in the POSTN-expressing fibroblast cluster associated with *M*,
701 *D*, *T* included CXCL14, also recently reported in BE scRNAseq analysis¹⁵. Notably, CXCL14 has been
702 reported to exert immunosuppressive activities when secreted by fibroblasts but not by epithelial
703 cells⁸⁴. POSTN and CXCL14 expression may contribute to the local enrichment in Tregs observed in some
704 CODEX cell neighborhoods of *D* and *T* samples. For instance, the “*inflamed mature intestinal*”
705 community which increased in number in *T* samples, contained numerous CD4 Treg cells. Similarly,
706 through consideration of neighborhood structure we found a negative correlation between Tregs and
707 CD36hi endothelial cells in some neighborhoods regardless of the disease phase, in line with the
708 reported association of loss of CD36hi endothelial cells with increased risk of progression in breast
709 cancer^{69,72}.

710

711 At the level of specific genes and pathways associated with EAC progression, numerous inflammatory
712 and malignancy markers in fibroblasts appeared in all modalities: scRNAseq, ECM proteomics and
713 CODEX. Overall, as expected, fibroblasts with gene signatures such as “TGF-beta regulation of
714 extracellular matrix”, or “Collagen biosynthesis and modifying enzymes”, were enriched with
715 progression as early as metaplasia, in line with adaptive alterations of a stroma subjected to the
716 constant stress of chronic inflammation. Specific changes pointed to a loss of tissue homeostasis
717 involving ECM remodeling by matrix metalloproteinases and collagen chaperones, such as SERPINH1,
718 ultimately resulting in the uncontrolled release of cytokines, such as TGF-beta. Such unopposed TGF-
719 beta signaling might account for the upregulation of periostin expression in fibroblasts at the
720 metaplastic phase^{15,85}.

721

722 Finally, the traditional use of systematic molecular profiling and differential expression/abundance
723 analysis remains potentially useful, notably if we exploit the availability of samples in the progression
724 phases. The identification of a small panel of biomarkers (PRAME, MAGEA6, CASP10, PTPN12, and
725 FAM183A) specifically upregulated at the dysplasia stage (*D*) is of particular practical importance
726 because they could serve as a much sought after biomarker panel for the rare progression from
727 premalignancy (BE) to malignancy (EAC). If confirmed, such biomarkers could initiate and justify more
728 aggressive ablative treatments in any dysplastic BE (including low grade dysplasia) prior to invasive
729 malignancy.

730
731 This Atlas of BE progressing to EAC, offers multiple modalities of data that also span multiple size scales
732 from molecular profiles to tissue architecture and mechanics, and will serve as a valuable resource to
733 the research community. Two limitations of this study are: (1) the course of progression is inferred from
734 snapshots of metachronic parallel evolution of lesions as a surrogate of a time course (longitudinal
735 monitoring), which however is permissive given the established sequence of the phases of progression;
736 (2) our matched normal samples used as non-cancerous baseline are actually not disease-free but likely
737 already inflamed tissues as revealed by comparison to disease-free individuals (unpublished
738 observations). Interactive web-portals to interrogate specific molecules in specific cell type and
739 progression phase are available (Methods). Many descriptive but intriguing findings await experimental
740 examination or focused validation in larger cohorts. Clinical translation of some of the observed changes
741 into actionable biomarkers for risk stratification or targets for prevention and intervention holds
742 tremendous potential. It will be also of great interest to determine if our findings can be extended to
743 other chronic inflammation-driven malignancies.

744 METHODS

745 [Sample Collection, Preparation, and Measurements](#)

746 **Human Barrett's Esophagus Tissue Specimens**

747 Fresh tissue specimens were obtained from consented patients with treatment naive Barrett's
748 esophageal adenocarcinoma (Research Institute - McGill University Health Centre REB # 2007-856)
749 undergoing endoscopy or esophagectomy. They were collected from regions containing tumor, matched
750 normal gastric (gastric cardia) and/or esophageal mucosa (at least 5 cm proximal to the top of columnar
751 lined mucosa), suspected metaplasia and suspected dysplasia. High-Definition white light and narrow
752 band endoscopic imaging was employed to attempt to clinically differentiate dysplasia from non-
753 dysplastic columnar lined mucosa (Barrett's metaplasia) at the time of surgery. Only tissue specimens
754 with confirmed histological diagnosis were used in subsequent multi-omic analyses (e.g. single cell
755 transcriptomics, multiplex imaging, ECM proteomics). Histological diagnosis was performed on H&E
756 stained sections of formalin fixed paraffin tissue blocks and corroborated by consensus of two expert
757 pathologists (S.C.-B. And P.-O.F.). Collected tissue specimens were divided in equal sections and placed
758 in cold medium (RPMI (Invitrogen) supplemented with Primocin (Invivogen) and gentamycin
759 (Invitrogen)) for single cell RNA sequence processing or shipment to various sites for subsequent
760 analyses. Patient demographics, exposure history (e.g., smoking, proton inhibitor use), Barrett's extent
761 (Prague Classification), and tumor characteristics (grade, stage) were collected (Suppl. Fig S1A).

763 [Single-cell RNAseq Methods](#)

764 **Single cell dissociation**

765 Tissue specimens were dissected to remove necrotic areas, minced and digested in 5 mL of Advanced
766 DMEM/F12 containing 10 mg Collagenase Type 3 (Worthington) and 500 U Hyaluronidase (Sigma) in a C-
767 tube (Miltenyi) using the gentleMACS Octo Dissociator (Miltenyi). The single cell suspension was
768 resuspended in PBS and 1mM DTT, strained through a 100um cell strainer (Fisher) and spun down
769 (500xg, 5 minutes, 4°C). Cells were resuspended in 0.25% Trypsin-EDTA (Invitrogen) and incubated for 5
770 minutes at 37°C, followed by addition of 10% fetal bovine serum to inactivate trypsin. The cell pellet
771 (500xg, 5 minutes, 4°C) was resuspended in 2.5U Dispase/10ug DNase buffer and incubated for 5
772 minutes at 37°C. The buffer was inactivated by adding excess PBS and the homogenate was strained (40
773 uM, Fisher) prior to centrifugation (500xg, 5 minutes, 4°C). Red blood cells were lysed using ACK Lysing
774 Buffer (Gibco) for 5 minutes at room temperature, followed by addition of excess PBS, prior to
775 centrifugation (500xg, 5 minutes, 4°C). The cell pellet was finally washed twice with 2% fetal bovine
776 serum in PBS prior to proceeding with single cell capture on the 10x Genomics platform.

777 **Single cell suspension quality assessment**

778 Before credentialing the cell suspension, the cells were filtered through a 40 um FLOWMI cell strainer
779 (SP Bel-Art; H13680-0040). Whenever necessary, centrifugation of the cells was carried out at 300xg for
780 11 minutes. Single cell viability and presence of debris and erythrocytes in the single cell suspension
781 were assessed prior to single cell capturing. Upon adequate viability (i.e. lack of debris and
782 erythrocytes), cells were captured on the 10x Genomics platform.

783 Cell viability was tested using the "LIVE/DEAD Viability/Cytotoxicity Kit for mammalian cells" that
784 contained Ethidium Homodimer-1 and Calcein-AM stain (ThermoFisher ; L-3224) dyes. First, a viability
785 stain mix was reconstituted by mixing 0.5 ul of 4mM Calcein-AM, 2ul of 2mM Ethidium Homodimer-1
786 and 100ul of PBS. A 5ul of cell suspension was then resuspended in 5ul of viability stain mix and the
787 solution was incubated at room temperature for 10 minutes. The sample viability was verified using a
788 hemocytometer (INCYTO C-Chip; DHC-N01-5) through GFP (for the Calcein-AM) and RFP (for the
789 Ethidium Homodimer-1) channels on an EVOS FL Auto Fluorescent microscope (ThermoFisher). Viability
790 was expressed as the percentage of live cells (Calcein-AM / GFP positive cells) over the sum of live
791 (Calcein-AM / GFP positive cells) and dead cells (Ethidium Homodimer-1 / RFP positive) cells.

792 Erythrocyte contamination was assessed by staining the cells with the cell permeable DNA dye DRAQ5
793 (ThermoFisher ; 65-0880-92). A nuclear staining mix was made by diluting the DRAQ5 stock solution
794 (5mM) down to 5uM with 1x PBS. Afterwards, 5ul of cell suspension was re-suspended in 5ul of nuclear
795 stain mix and the solution was incubated at room temperature for 5 minutes. The nuclear stain was
796 visualized using a hemocytometer (INCYTO C-Chip; DHC-N01-5) through the Cy5 channel on an EVOS FL
797 Auto Fluorescent microscope (ThermoFisher). Erythrocyte contamination was expressed as the
798 percentage of "round donut-shaped DRAQ5 negative objects on bright-field" over the sum of "round
799 donut-shaped DRAQ5 negative objects on bright-field" and "nuclear stained DRAQ5 positive cells".

800 Additionally, we assessed the cell suspension for the presence of any other contaminants/debris as well
801 as contaminants that might interfere with the capturing on the microfluidic chip such as large debris.
802 The percentage of debris presented in the sample was expressed as follows: Percentage of "observed

803 non-cell objects on bright-field” over the sum of “observed objects on bright-field” and “observed cells
804 marked on the fluorescent channels”. A sample was deemed adequate for capturing if “cell viability”
805 was $\geq 70\%$, “erythrocyte contamination” was $\leq 10\%$ and “debris percentage” was $\leq 30\%$. The cell
806 concentration in the cell suspension, measured by counting the number of “Calcein-AM / GFP positive
807 cells” and “Ethidium Homodimer-1 / RFP positive cells” in the large 4 squares on each corner of the
808 hemocytometer, was calculated as follows: Number of cells / ul = [(Calcein-AM / GFP positive cells +
809 Ethidium Homodimer-1 / RFP positive cells) / 4] * 10 * 2 where 10 was the dilution factor on the
810 hemocytometer and 2 was the dilution factor when the cell suspension was mixed with the dye
811 solution.

812 **Single cell capturing**

813 Single cells were captured on the 10x Genomics platform. Single cell 3’ end gene expression profiling
814 was carried out according to the “Chromium Next GEM Single Cell 3’ Reagent Kits v3.1” protocol and
815 recommended reagents. Single cell Copy Number Variation was queried using the “Chromium Single Cell
816 DNA Reagent Kits” protocol and recommended reagents. Of note the CNV kit described above is
817 currently discontinued. The sequencing libraries were created as per the above protocols with the
818 modifications presented in the following section.

819 **Sequencing of the 10x single cell libraries**

820 Libraries were quantified using a LightCycler 480 Real Time PCR instrument (Roche) and the KAPA library
821 quantification kit (Roche) with triplicate measurements. Library quantification values were used both for
822 the MGI library conversion and for Illumina sequencing normalization.

823 Libraries sequenced on MGI (MGI Tech) were converted after 10x library construction in order to be
824 compatible with MGI sequencers using the MGIEasy Universal Library Conversion Kit. The kit circularizes
825 the libraries making them compatible for MGI systems. To sequence the circularized libraries, they were
826 first amplified by rolling circle amplification, resulting in a long DNA strand which individually folds into a
827 tight ball (i.e. a DNA nanoball) where one library fragment results in one DNA nanoball. Before loading
828 into the flowcells, the amplified nanoballs were quantified with a Qubit ssDNA HS Assay kit
829 (ThermoFisher), normalized and loaded onto the sequencing flowcell using the auto-loader method
830 (auto-loader MGI-DL-200R). The flowcells have a functionalized surface that captures and immobilizes
831 the nanoballs in a grid pattern. Typically, two libraries were loaded per lane for the single cell RNA
832 libraries. The DNBSEQ-G400RS PE100 MGI kit with App-A primers was used for single cell RNA library
833 sequencing. The DNBSEQ-G400RS PE150 MGI kit with App-A primers was used for single cell DNA library
834 sequencing.

835 The flowcells were sequenced on a DNBSEQ-G400 MGI sequencer. Single cell RNA libraries were
836 sequenced as follows: 28 cycles for read1, 150 cycles for read2 and 8 cycles for the i7 index. Single cell
837 DNA libraries were sequenced as follows: 151 cycles for Read1, 151 cycles for Read2 and 8 cycles for the
838 i5 index. Because libraries must be color-balanced for all cycles sequenced in order to maintain a
839 minimum ratio of 0.125 for each base at each cycle, color-balanced single index adapters (10x
840 Genomics) were used for libraries sequenced on MGI.

841 A subset of 23 libraries were sequenced on the Illumina NovaSeq 6000 platform using S4 flowcells. To
842 ensure uniform loading of the libraries, a preliminary pool was sequenced on Illumina iSeq and the

843 library proportions were readjusted accordingly. Another subset of 12 libraries were sequenced on the
844 Illumina HiSeq 4000 system typically with one library per lane.

845 Although the MGI sequencer has onboard capability to demultiplex samples, we chose to use
846 independent tools to demultiplex the raw fastq files for each lane to give us the flexibility to reprocess if
847 needed. The fastq files generated using the balanced single index adapters were merged for each library
848 after demultiplexing. The MGI runs were mainly demultiplexed by fastq-multx
849 (<https://github.com/brwnj/fastq-multx>) but also using fgbio/DemuxFastqs
850 (<http://fulcrumgenomics.github.io/fgbio/tools/latest/DemuxFastqs.html>). In both instances we used a
851 mismatch of 1. Illumina runs were demultiplexed using the the standard bcl2fastq tool.

853 **scRNA-seq Data Processing and Analysis**

854 **Read processing and alignment**

856 After polyA-trimming via cutadapt (v3.2)⁸⁶, reads were pseudo-aligned to the GRCh38 reference
857 transcriptome (ENSEMBL release 96) with kallisto (v0.46.2)⁸⁷ using the default kmer size of 31. The
858 pseudo-aligned reads were processed into a cell-by-gene count matrix using bustools (0.40.0)⁸⁸. Cell
859 barcodes were filtered using the whitelist (v3) provided by 10xGenomics. All further processing was
860 done in scanpy (v.1.7.1)⁸⁹.

861

862 **Quality control and normalization**

863 Quality control was performed for each sample independently as follows. Cell barcodes with less than
864 1000 counts or less than 500 genes expressed or with more than 10% mitochondrial gene expression
865 were removed. Doublet cells were identified using scrublet⁹⁰, and any cell barcode with a scrublet score
866 > 0.2 was removed. Only coding genes were retained in the final count matrix. Expression profiles were
867 normalized by total counts, the 4000 most highly variable genes being identified⁹¹, renormalized, log-
868 transformed and z-scored. The data were projected onto the first 50 principal components.

869 After the above per-sample preprocessing, samples were pooled and integrated using Harmony²⁰ on the
870 first 50 principal components with a maximum of 25 iterations. A nearest neighbor graph (k=15) was
871 calculated on the Harmony-corrected principal components space. Datasets were visualized in 2D via
872 UMAP⁹² and initialized with PAGA⁹³ coordinates. The nearest neighbor graph was clustered with the
873 Leiden algorithm⁹⁴. The processed datasets were visualized interactively using Cellbrowser⁹⁵ allowing
874 for easy access and exploration across teams and laboratories.

875

876 **Cell type calling**

877 Cell types were called using the Human Cell Landscape (HCL) reference dataset²¹. Briefly, the raw
878 expression profile x_i of cells i was normalized by total counts and log-transformed
879
$$y_{ij} = \log(1 + x_{ij} / \sum_j x_{ij})$$

with x_{ij} the counts of genes j in each cell i . Cells were compared to the
880 Human Cell Landscape reference by Pearson correlation, and the reference profile with the highest
881 correlation determined the cell type call. If the highest correlation was below 0.3, the cell type was
882 defined as "unknown".

883

884 The per-cell types were categorized on a per-cluster level based priors calls with the expression of
885 markers indicated from a range of sources including Cell Ontology⁹⁶ and reference materials from
886 ThermoFisher, Abcam and BioLegend.

887

888 Fine-grained labels were produced using a number of techniques. To fine grain the squamous
889 esophageal epithelium we compared our esophageal dataset to 6 esophageal samples from the Human
890 Cell Atlas⁹⁷. HCA-derived gene signatures were produced from the top 50 most differentially expressed
891 genes for each cell type from the HCA data. Using the single-cell gene set scoring method GSSNNG, we
892 scored the cell type labels using those HCA-derived signatures. The squamous epithelium subtypes
893 (upper, intermediate, basal) were clearly indicated through high gene set scores in the CRUK dataset.
894 Also, the HCA signatures clearly identified our cell types including fibroblasts and glandular gastro-
895 intestinal (GI) epithelium. Some HCA signatures were non-specific in our dataset including the
896 esophageal basal cell layer, the venous endothelium, and the ductal epithelium. Otherwise, fine graining
897 was performed by using well known marker genes from the literature.

898

899 **Sample PCA and clustering**

900 In order to apply PCA, sample level clustering, and perform differential expression (as described below),
901 pseudo-bulk profiles were produced for each coarse-grained cell label and over all cells. To produce a
902 pseudo-bulk profile computationally, cells of a given type were selected and raw gene expression counts
903 were summed. For a given cell type, such as for example CD8 T cells, this produced one gene expression
904 profile per sample. PCA was performed using R 'prcomp', principal components (eigenvectors) were
905 recovered and used for plotting of principal components. Clustering of samples was performed using the
906 R hclust function with average linkage.

907

908 **Differential expression**

909 In order to estimate differential expression between the tissue diagnosis on a per cell basis, we applied
910 DESeq2 to pseudo-bulk profiles while accounting for sequencing depth and patient heterogeneity using
911 the model $gene \sim patient + cell_counts + avg_molecules + dx$ where the *patient* is patient ID (each
912 patient has several different samples), *cell_counts* is the number of cells observed in a given sample,
913 *avg_molecules* is the mean of gene counts, *dx* is the tissue diagnosis. The goal is to find genes where the
914 variations in expression patterns are explained more by the change in tissue diagnosis rather than from
915 other considered factors.

916

917 There was considerable bias introduced from ambient RNA which produced false positive results⁹⁸. In
918 order to identify differentially expressed genes that were artifacts the following heuristic was used: If a
919 gene was found to be differentially expressed in a cell type and was also differentially expressed in other
920 cell types, and the ambient profile was correlated with the pseudo-bulk profile (across samples) and
921 statistically associated with the tissue diagnosis [other metrics], then the DEG was removed from the
922 results. Gene expression heatmaps were created by taking the collection of differentially expressed
923 genes, and scoring genes based on association with disease progression. In particular, for the purpose of
924 visualization, genes were selected through association with (*mNE*, *mNS*, *M*) vs. (*D*, *T*) using logistic
925 regression.

926

927 **Gene set scoring**

928 For each coarse-grained cell type, differentially expressed genes with a max log2 fold change (between
929 tissue diagnoses) of at least 0.58 and adjusted p-value of 0.05 were submitted to the Enrichr service²⁶.
930 Pathway enrichment tables were downloaded for BioPlanet 2019, MSigDB Hallmarks, KEGG 2021, and
931 WikiPathways 2021. (see Suppl. Table S2)

932

933 **Statistical analysis of cell type proportion changes**

934 Changes in cell type proportions across diagnoses were analyzed with scCODA⁹⁹. Changes were
935 computed relative to mNE samples and reference cell types were selected based on the cell type with
936 the least dispersion across diagnosis. To account for inter-patient differences, and systematic differences
937 in cell type composition between biopsy/resection samples, those were included as covariates into the
938 scCODA model. Model inference was performed using HMC and 60000 iterations. MCMC chains were
939 inspected manually for convergence. Statistically significant covariates were determined using the
940 model's posterior inclusion probabilities and an FDR of 0.05.

941

942 **Copy Number Variation inference from scRNAseq**

943 We used a python re-implementation¹⁰⁰ of the inferCNV algorithm⁴⁸ to call copy number variation (CNV)
944 in the single cell data. First, all samples across all diagnoses were pooled and epithelial cells were
945 extracted based on cell type calling. Any epithelial cell from a mNE/mNS sample was assigned to the
946 reference set of inferCNV, any other epithelial cell was assigned to the query set in inferCNV. After
947 filtering out lowly expressed genes (mean expression <0.1) and standard inferCNV preprocessing, the
948 data were smoothed along chromosomal coordinates with a window size of 101 and a step size of 2. The
949 CNV burden $\sum_j |X_{ij}|$ of a single cell i was estimated as $\sum_j |X_{ij}|$, where X_{ij} is the
950 inferred gain/loss in cell i , gene window j . The 99% quantile of the CNV burden $\sum_j |X_{ij}|$ in mNE/mNS
951 epithelial cells was calculated and, assuming no CNV's present in mNE/mNS samples, any non-reference
952 cells exceeding this threshold were classified as containing CNVs.

953

954 **[Proteomics Methods](#)**

955 **Chemicals**

956 LC-MS-grade acetonitrile (ACN) and water were obtained from Burdick & Jackson (Muskegon, MI).
957 Reagents for protein chemistry, including sodium dodecyl sulfate (SDS), ammonium bicarbonate,
958 iodoacetamide (IAA), dithiothreitol (DTT), sequencing-grade endoproteinase Lys-C, and formic acid (FA)
959 were purchased from Sigma-Aldrich (St. Louis, MO). Sequencing-grade trypsin was purchased from
960 Promega (Madison, WI). Glycerol-free PNGase F was purchased from New England BioLabs (Ipswich,
961 MA).

962

963 **Sample Preparation**

964 Proteomic analysis was performed as described in Bons *et al.*¹⁰¹. Briefly, fresh esophageal tissues were
965 minced in small pieces, weighed, and flash frozen for storage at -80°C. The ECM fraction was isolated
966 from the frozen tissues using the Compartment Protein Extraction Kit (Millipore, #2145) as per
967 manufacturer's protocol. About 1/10 of purified ECM was used to assess ECM protein enrichment purity
968 and yield by Western blot analysis. From the remaining purified ECM fraction, proteins were solubilized
969 by agitation for 10 minutes in a solution containing 1% SDS, 50 mM DTT and 1X NuPAGE lithium dodecyl

970 sulfate (LDS) sample buffer (Life Technologies, Carlsbad, CA), followed by sonication for 10 minutes, and
971 finally heating at 85 °C for 1 hour with agitation. Solubilized proteins were concentrated in a single
972 stacking acrylamide Bis-Tris gel, in-gel reduced with 10 mM DTT, and alkylated with 55 mM IAA. Finally,
973 proteins were in-gel digested with 250 ng of sequencing-grade endoproteinase Lys-C in 25 mM
974 ammonium bicarbonate at 37 °C for 2 hours with agitation, followed by an overnight incubation with
975 250 ng sequencing-grade trypsin in 25 mM ammonium bicarbonate at 37 °C with agitation. After tryptic
976 peptide extraction, samples were vacuum dried, resuspended in 25 mM ammonium bicarbonate, and
977 peptides were deglycosylated with 3 µL (1,500 U) of glycerol-free PNGase F at 37 °C for 3 hours with
978 agitation. The reaction was quenched by adding FA to a final concentration of 1%. Peptide samples were
979 finally desalted using stage-tips made in-house containing a C₁₈ disk, vacuum dried, and re-suspended in
980 aqueous 0.2% FA spiked with indexed retention time peptide standards (iRT, Biognosys, Schlieren,
981 Switzerland)¹⁰².

982 **LC-DIA-MS Analysis**

983 LC-MS/MS were performed on an Eksigent Ultra Plus nano-LC 2D HPLC system (Dublin, CA) combined
984 with a cHiPLC system directly connected to an orthogonal quadrupole time-of-flight (Q-TOF) SCIEX
985 TripleTOF 6600 mass spectrometer (SCIEX, Redwood City, CA). The solvent system consisted of 2% ACN,
986 0.1% FA in H₂O (solvent A) and 98% ACN, 0.1% FA in H₂O (solvent B). Proteolytic peptides were loaded
987 onto a C₁₈ pre-column chip (200 µm × 6 mm ChromXP C18-CL chip, 3 µm, 300 Å; SCIEX) and washed at 2
988 µL/minute for 10 minutes with the loading solvent (0.1% FA in H₂O) for desalting. Peptides were
989 transferred to the 75 µm × 15 cm ChromXP C₁₈-CL chip, 3 µm, 300 Å (SCIEX) and eluted at 300 nL/min
990 with the following gradient of solvent B: 5% for 5 min, linear from 5% to 8% in 15 min, linear from 8% to
991 35% in 97 min, and up to 80% in 20 min, with a total gradient length of 180 min. Samples were analyzed
992 by data-independent acquisition (DIA) using 64 variable-sized windows covering the m/z 400-1,250
993 range (Suppl. Table S7)¹⁰³⁻¹⁰⁵. MS scans were collected with 250-ms accumulation time, and MS/MS
994 scans with 45-ms accumulation time in “high-sensitivity” mode. The collision energy (CE) for each
995 segment was based on the z=2+ precursor ion centered within the window with a CE spread of 10 or 15
996 eV.

997 **MS DIA Data Processing**

998 DIA data were processed in Spectronaut (version 14.10.201222.47784) (Biognosys) using a pan-human
999 library containing 10,316 proteins¹⁰⁶. Data extraction parameters were selected as dynamic using non-
1000 linear iRT calibration. Identification was performed using 1% precursor and protein q-values.
1001 Quantification was based on the MS/MS peak areas of the 3-6 best fragment ions per precursor ion,
1002 local normalization was applied, and iRT profiling was selected. Differential protein abundance analysis
1003 was performed using paired t-tests, and p-values were corrected for multiple testing using the Storey
1004 method¹⁰⁷. Protein groups with at least two unique peptides, q-value ≤ 0.001, and absolute Log₂(fold-
1005 change) ≥ 0.58 were considered to be significantly altered (Suppl. Table S6).

1006

1007 **Atomic Force Microscopy Methods**

1008 Snap frozen patient samples were cryosectioned. A reference slide has been H&E stained from the
1009 adjacent test sample to visualize the location of epithelium and stroma. Unfixed slides were tested with

1010 AFM for stiffness and distribution of measurements were visualized using AFM manufacturer's software
1011 (Fig. S8).

1012

1013 [CODEX Multiplexed Protein Imaging Methods](#)

1014 **CODEX Array Creation and Pathology Annotation**

1015 Imaging data were collected from 5 human donors, each of whom constituting a dataset. Each dataset
1016 included tissue sections taken from individually diagnosed formalin fixed paraffin embedded (FFPE)
1017 tissue blocks that were combined onto the same coverslip (cut at 4 μ m thickness). To ensure accurate
1018 disease phase diagnosis, three pathologists independently evaluated the H&E staining of the sections
1019 performed on the same tissue sections as used for the CODEX multiplexed imaging (Fig. S9B-C). They
1020 called disease phase granular diagnosis (e.g., mNE, mNS, M), and estimated percentages of type of
1021 epithelium in each image (e.g., % squamous, % metaplasia, % dysplasia, % tumor). The pathologists
1022 scores were then aggregated and averaged (Suppl. Table S8).

1023

1024 **CODEX Antibody Conjugation and Panel Creation**

1025 CODEX multiplexed protein imaging was executed according to the CODEX staining and imaging protocol
1026 previously described⁶³. Antibody panels were chosen to include targets that identify subtypes of
1027 intestinal epithelium and stromal cells, and cells of the innate and adaptive immune system. Detailed
1028 panel information can be found in Suppl. Table S9. Each antibody was conjugated to a unique
1029 oligonucleotide barcode, after which the tissues were stained with the antibody-oligonucleotide
1030 conjugates and validated to ensure that staining patterns matched expected patterns already
1031 established for IHC within positive control tissues of the esophagus or tonsil. Similarly, Hematoxylin and
1032 Eosin morphology stainings were used to confirm location of marker staining. First, antibody-
1033 oligonucleotide conjugates were tested in low-plex fluorescence assays and signal-to-noise ratio was
1034 also evaluated at this step, then conjugates were tested all together in a single CODEX multicyle.

1035

1036 **CODEX Multiplexed Protein Imaging**

1037 The tissue arrays were then stained with the complete validated panel of CODEX antibodies and
1038 imaged⁶³. Briefly, the workflow entailed cyclic stripping, annealing, and imaging of fluorescently labeled
1039 oligonucleotides complementary to the oligonucleotide on the conjugate. After validation of the
1040 antibody-oligonucleotide conjugate panel, a test CODEX multiplexed assay was run, during which signal-
1041 to-noise ratio was again evaluated, and the optimal dilution, exposure time, and appropriate imaging
1042 cycle was evaluated for each conjugate (Suppl. Table S9). Finally, each coverslip array underwent CODEX
1043 multiplexed imaging.

1044

1045 **CODEX Data Processing**

1046 Raw imaging data were then processed using the CODEX Uploader for image stitching, drift
1047 compensation, deconvolution, and cycle concatenation. Processed data were then segmented using the
1048 CellVisionSegmenter, a neural network R-CNN-based single-cell segmentation algorithm
1049 (<https://github.com/michaellee1/CellSeg>)¹⁰⁸. After upload, the images were again evaluated for specific
1050 signal: any marker that produced an untenable pattern or a low signal-to-noise ratio was excluded from
1051 the ensuing analysis. Uploaded images were visualized in ImageJ (<https://imagej.nih.gov/ij/>).

1052

1053 **CODEX Cell Type Analysis**

1054 Cell type identification was done following the methods developed previously⁶⁷. Briefly, nucleated cells
1055 were selected by gating DRAQ5, Hoechst double-positive cells, followed by z-normalization of protein
1056 markers used for clustering (some phenotypic markers were not used in the unsupervised clustering).
1057 The data were overclustered with X-shift (<https://github.com/nolanlab/vortex>). Clusters were assigned a
1058 cell type based on average cluster protein expression and location within the image. Impure clusters
1059 were split or reclustered following mapping back to the original fluorescent images.

1060

1061 **CODEX Cell-cell colocalization analysis and Shannon's Index**

1062 To evaluate enriched cell-cell interactions, we calculated the frequency of neighbors using a nearest
1063 neighbor (n=10 neighbors) approach and compared the frequency of occurrences to 10,000
1064 permutations of the cell type locations. We filtered this list for cell-cell interactions enriched within
1065 certain conditions compared to the other disease states. Shannon's Diversity Index was calculated by
1066 taking the negative sum of each proportion multiplied by the natural logarithm of the proportion.

1067

1068 **CODEX Neighborhood and Community Identification Analysis**

1069 Neighborhood analysis was performed as described previously^{109,110}. Briefly, this analysis involved (i)
1070 taking windows of cells across the entire cell type map of a tissue with each cell as the center of a
1071 window, (ii) calculating the number of each cell type within this window, (iii) clustering these vectors,
1072 and (iv) assigning overall structure based on the average composition of the cluster. Neighborhoods
1073 were overclustered to 30 clusters. These clusters were mapped back to the tissue and evaluated for cell
1074 type enrichments to determine overall structure and merged down into the final unique neighborhoods.
1075 Communities were determined similar to how multicellular neighborhoods were determined with some
1076 minor differences⁶⁵. Briefly, the cells in the neighborhood tissue maps were taken with a larger window
1077 size of 100 nearest neighbors. These windows were then taken across the entirety of the tissue and the
1078 vectors clustered with k-means clustering and overclustering with 20 total clusters. These clusters were
1079 mapped back to the tissue and evaluated for neighborhood composition and enrichment to determine
1080 overall community type.

1081 **DECLARATION OF INTERESTS**

1082 G.P.N. has equity in and is a scientific advisory board member of Akoya Biosciences, Inc.
1083 C.M.S. is a scientific advisor to, has stock options in, and has received research funding from
1084 Enable Medicine Inc., and is a scientific advisor to AstraZeneca plc.
1085 The other authors declare no competing interests.

1086 FUNDING

1087 This work was supported by a Cancer Research UK Grand Challenge (CRUK grant 29068). Additional
1088 support from the Tlsty Lab at UCSF (TDT: CRUK grant 27145, National Cancer Institute Award
1089 5R35CA197694, PG: National Cancer Institute Award 5R50CA211543), McGill University Thoracic and
1090 Upper GI Cancer Research Laboratories (LLF: CRUK grant 29071), the Advanced Genomic Technologies
1091 Laboratory (IR: CRUK grant 29078), and the Huang lab (SH: National Institute of General Medical
1092 Sciences Award 5R01GM135396) is greatly appreciated.

1093 REFERENCES

1094

1. Uhlenhopp, D.J., Then, E.O., Sunkara, T., and Gaduputi, V. (2020). Epidemiology of esophageal cancer: update in global trends, etiology and risk factors. *Clin. J. Gastroenterol.* *13*, 1010–1021. [10.1007/s12328-020-01237-x](https://doi.org/10.1007/s12328-020-01237-x).
2. Smyth, E.C., Lagergren, J., Fitzgerald, R.C., Lordick, F., Shah, M.A., Lagergren, P., and Cunningham, D. (2017). Oesophageal cancer. *Nat. Rev. Dis. Primer* *3*, 17048. [10.1038/nrdp.2017.48](https://doi.org/10.1038/nrdp.2017.48).
3. Yang, J., Liu, X., Cao, S., Dong, X., Rao, S., and Cai, K. (2020). Understanding Esophageal Cancer: The Challenges and Opportunities for the Next Decade. *Front. Oncol.* *10*, 1727. [10.3389/fonc.2020.01727](https://doi.org/10.3389/fonc.2020.01727).
4. McColl, K.E.L. (2019). What is causing the rising incidence of esophageal adenocarcinoma in the West and will it also happen in the East? *J. Gastroenterol.* *54*, 669–673. [10.1007/s00535-019-01593-7](https://doi.org/10.1007/s00535-019-01593-7).
5. Hur, C., Miller, M., Kong, C.Y., Dowling, E.C., Nattinger, K.J., Dunn, M., and Feuer, E.J. (2013). Trends in Esophageal Adenocarcinoma Incidence and Mortality. *Cancer* *119*, 1149–1158. [10.1002/cncr.27834](https://doi.org/10.1002/cncr.27834).
6. Cancer Genome Atlas Research Network, Analysis Working Group: Asan University, BC Cancer Agency, Brigham and Women's Hospital, Broad Institute, Brown University, Case Western Reserve University, Dana-Farber Cancer Institute, Duke University, Greater Poland Cancer Centre, et al. (2017). Integrated genomic characterization of oesophageal carcinoma. *Nature* *541*, 169–175. [10.1038/nature20805](https://doi.org/10.1038/nature20805).
7. Nowicki-Osuch, K., Zhuang, L., Jammula, S., Bleaney, C.W., Mahbubani, K.T., Devonshire, G., Katz-Summercorn, A., Eling, N., Wilbrey-Clark, A., Madisson, E., et al. (2021). Molecular phenotyping reveals the identity of Barrett's esophagus and its malignant transition. *Science* *373*, 760–767. [10.1126/science.abd1449](https://doi.org/10.1126/science.abd1449).
8. Krishnamoorthi, R., Mohan, B.P., Jayaraj, M., Wang, K.K., Katzka, D.A., Ross, A., Adler, D.G., and Iyer, P.G. (2020). Risk of progression in Barrett's esophagus indefinite for dysplasia: a systematic review and meta-analysis. *Gastrointest. Endosc.* *91*, 3-10.e3. [10.1016/j.gie.2019.07.037](https://doi.org/10.1016/j.gie.2019.07.037).
9. Weaver, J.M.J., Ross-Innes, C.S., Shannon, N., Lynch, A.G., Forshew, T., Barbera, M., Murtaza, M., Ong, C.-A.J., Lao-Sirieix, P., Dunning, M.J., et al. (2014). Ordering of mutations in preinvasive disease stages of esophageal carcinogenesis. *Nat. Genet.* *46*, 837–843. [10.1038/ng.3013](https://doi.org/10.1038/ng.3013).
10. Killcoyne, S., Gregson, E., Wedge, D.C., Woodcock, D.J., Eldridge, M.D., de la Rue, R., Miremadi, A., Abbas, S., Blasko, A., Kosmidou, C., et al. (2020). Genomic copy number predicts esophageal cancer years before transformation. *Nat. Med.* *26*, 1726–1732. [10.1038/s41591-020-1033-y](https://doi.org/10.1038/s41591-020-1033-y).
11. Katz-Summercorn, A.C., Jammula, S., Frangou, A., Peneva, I., O'Donovan, M., Tripathi, M., Malhotra, S., di Pietro, M., Abbas, S., Devonshire, G., et al. (2022). Multi-omic cross-

- sectional cohort study of pre-malignant Barrett's esophagus reveals early structural variation and retrotransposon activity. *Nat. Commun.* **13**, 1407. 10.1038/s41467-022-28237-4.
12. Stachler, M.D., Camarda, N.D., Deitrick, C., Kim, A., Agoston, A.T., Odze, R.D., Hornick, J.L., Nag, A., Thorner, A.R., Ducar, M., et al. (2018). Detection of Mutations in Barrett's Esophagus Before Progression to High-Grade Dysplasia or Adenocarcinoma. *Gastroenterology* **155**, 156–167. 10.1053/j.gastro.2018.03.047.
 13. Luebeck, J., Ng, A.W.T., Galipeau, P.C., Li, X., Sanchez, C.A., Katz-Summercorn, A.C., Kim, H., Jammula, S., He, Y., Lippman, S.M., et al. (2023). Extrachromosomal DNA in the cancerous transformation of Barrett's oesophagus. *Nature*. 10.1038/s41586-023-05937-5.
 14. Maag, J.L.V., Fisher, O.M., Levert-Mignon, A., Kaczorowski, D.C., Thomas, M.L., Hussey, D.J., Watson, D.I., Wettstein, A., Bobryshev, Y.V., Edwards, M., et al. (2017). Novel Aberrations Uncovered in Barrett's Esophagus and Esophageal Adenocarcinoma Using Whole Transcriptome Sequencing. *Mol. Cancer Res. MCR* **15**, 1558–1569. 10.1158/1541-7786.MCR-17-0332.
 15. Nowicki-Osuch, K., Zhuang, L., Cheung, T.S., Black, E.L., Masque-Soler, N., Devonshire, G., Redmond, A.M., Freeman, A., di Pietro, M., Pilonis, N., et al. (2023). Single-cell RNA sequencing unifies developmental programs of Esophageal and Gastric Intestinal Metaplasia. *Cancer Discov.*, CD-22-0824. 10.1158/2159-8290.CD-22-0824.
 16. Murphy, K.J., Chambers, C.R., Herrmann, D., Timpson, P., and Pereira, B.A. (2021). Dynamic Stromal Alterations Influence Tumor-Stroma Crosstalk to Promote Pancreatic Cancer and Treatment Resistance. *Cancers* **13**, 3481. 10.3390/cancers13143481.
 17. Mishra, R., Haldar, S., Placencio, V., Madhav, A., Rohena-Rivera, K., Agarwal, P., Duong, F., Angara, B., Tripathi, M., Liu, Z., et al. Stromal epigenetic alterations drive metabolic and neuroendocrine prostate cancer reprogramming. *J. Clin. Invest.* **128**, 4472–4484. 10.1172/JCI99397.
 18. Xu, M., Zhang, T., Xia, R., Wei, Y., and Wei, X. (2022). Targeting the tumor stroma for cancer therapy. *Mol. Cancer* **21**, 208. 10.1186/s12943-022-01670-1.
 19. Greten, F.R., and Grivennikov, S.I. (2019). Inflammation and Cancer: Triggers, Mechanisms, and Consequences. *Immunity* **51**, 27–41. 10.1016/j.immuni.2019.06.025.
 20. Korsunsky, I., Millard, N., Fan, J., Slowikowski, K., Zhang, F., Wei, K., Baglaenko, Y., Brenner, M., Loh, P.-R., and Raychaudhuri, S. (2019). Fast, sensitive and accurate integration of single-cell data with Harmony. *Nat. Methods* **16**, 1289–1296. 10.1038/s41592-019-0619-0.
 21. Han, X., Zhou, Z., Fei, L., Sun, H., Wang, R., Chen, Y., Chen, H., Wang, J., Tang, H., Ge, W., et al. (2020). Construction of a human cell landscape at single-cell level. *Nature* **581**, 303–309. 10.1038/s41586-020-2157-4.
 22. Parikh, K., Antanaviciute, A., Fawcner-Corbett, D., Jagielowicz, M., Aulicino, A., Lagerholm, C., Davis, S., Kinchen, J., Chen, H.H., Alham, N.K., et al. (2019). Colonic epithelial cell diversity in health and inflammatory bowel disease. *Nature* **567**, 49–55. 10.1038/s41586-019-0992-y.

23. Gutierrez-Gonzalez, L., Graham, T.A., Rodriguez-Justo, M., Leedham, S.J., Novelli, M.R., Gay, L.J., Ventayol-Garcia, T., Green, A., Mitchell, I., Stoker, D.L., et al. (2011). The clonal origins of dysplasia from intestinal metaplasia in the human stomach. *Gastroenterology* *140*, 1251–1260.e1–6. 10.1053/j.gastro.2010.12.051.
24. Squair, J.W., Gautier, M., Kathe, C., Anderson, M.A., James, N.D., Hutson, T.H., Hudelle, R., Qaiser, T., Matson, K.J.E., Barraud, Q., et al. (2021). Confronting false discoveries in single-cell differential expression. *Nat. Commun.* *12*, 5692. 10.1038/s41467-021-25960-2.
25. Love, M.I., Huber, W., and Anders, S. (2014). Moderated estimation of fold change and dispersion for RNA-seq data with DESeq2. *Genome Biol.* *15*, 550. 10.1186/s13059-014-0550-8.
26. Xie, Z., Bailey, A., Kuleshov, M.V., Clarke, D.J.B., Evangelista, J.E., Jenkins, S.L., Lachmann, A., Wojciechowicz, M.L., Kropiwnicki, E., Jagodnik, K.M., et al. (2021). Gene Set Knowledge Discovery with Enrichr. *Curr. Protoc.* *1*, e90. 10.1002/cpz1.90.
27. Chen, E.Y., Tan, C.M., Kou, Y., Duan, Q., Wang, Z., Meirelles, G.V., Clark, N.R., and Ma'ayan, A. (2013). Enrichr: interactive and collaborative HTML5 gene list enrichment analysis tool. *BMC Bioinformatics* *14*, 128. 10.1186/1471-2105-14-128.
28. McDonald, S.A.C., Lavery, D., Wright, N.A., and Jansen, M. (2015). Barrett oesophagus: lessons on its origins from the lesion itself. *Nat. Rev. Gastroenterol. Hepatol.* *12*, 50–60. 10.1038/nrgastro.2014.181.
29. Barbera, M., and Fitzgerald, R.C. (2010). Cellular origin of Barrett's metaplasia and oesophageal stem cells. *Biochem. Soc. Trans.* *38*, 370–373. 10.1042/BST0380370.
30. Jiang, M., Li, H., Zhang, Y., Yang, Y., Lu, R., Liu, K., Lin, S., Lan, X., Wang, H., Wu, H., et al. (2017). Transitional basal cells at the squamous–columnar junction generate Barrett's oesophagus. *Nature* *550*, 529–533. 10.1038/nature24269.
31. Hanahan, D. (2022). Hallmarks of Cancer: New Dimensions. *Cancer Discov.* *12*, 31–46. 10.1158/2159-8290.CD-21-1059.
32. Buechler, M.B., Pradhan, R.N., Krishnamurty, A.T., Cox, C., Calviello, A.K., Wang, A.W., Yang, Y.A., Tam, L., Caothien, R., Roose-Girma, M., et al. (2021). Cross-tissue organization of the fibroblast lineage. *Nature* *593*, 575–579. 10.1038/s41586-021-03549-5.
33. Lendahl, U., Muhl, L., and Betsholtz, C. (2022). Identification, discrimination and heterogeneity of fibroblasts. *Nat. Commun.* *13*, 3409. 10.1038/s41467-022-30633-9.
34. Lee, S.-H., Contreras Panta, E.W., Gibbs, D., Won, Y., Min, J., Zhang, C., Roland, J.T., Hong, S.-H., Sohn, Y., Krystofiak, E., et al. (2023). Apposition of fibroblasts with metaplastic gastric cells promotes dysplastic transition. *Gastroenterology*, S001650852300731X. 10.1053/j.gastro.2023.04.038.
35. De Palma, M., Biziato, D., and Petrova, T.V. (2017). Microenvironmental regulation of tumour angiogenesis. *Nat. Rev. Cancer* *17*, 457–474. 10.1038/nrc.2017.51.
36. Raza, A., Franklin, M.J., and Dudek, A.Z. (2010). Pericytes and vessel maturation during tumor angiogenesis and metastasis. *Am. J. Hematol.* *85*, 593–598. 10.1002/ajh.21745.

37. Dias, D.O., Kalkitsas, J., Kelahmetoglu, Y., Estrada, C.P., Tatarishvili, J., Holl, D., Jansson, L., Banitalebi, S., Amiry-Moghaddam, M., Ernst, A., et al. (2021). Pericyte-derived fibrotic scarring is conserved across diverse central nervous system lesions. *Nat. Commun.* *12*, 5501. 10.1038/s41467-021-25585-5.
38. He, S., Wang, L.-H., Liu, Y., Li, Y.-Q., Chen, H.-T., Xu, J.-H., Peng, W., Lin, G.-W., Wei, P.-P., Li, B., et al. (2020). Single-cell transcriptome profiling of an adult human cell atlas of 15 major organs. *Genome Biol.* *21*, 294. 10.1186/s13059-020-02210-0.
39. Bosma, E.K., van Noorden, C.J.F., Schlingemann, R.O., and Klaassen, I. (2018). The role of plasmalemma vesicle-associated protein in pathological breakdown of blood-brain and blood-retinal barriers: potential novel therapeutic target for cerebral edema and diabetic macular edema. *Fluids Barriers CNS* *15*, 24. 10.1186/s12987-018-0109-2.
40. Schupp, J.C., Adams, T.S., Cosme, C., Raredon, M.S.B., Yuan, Y., Omote, N., Poli, S., Chioccioli, M., Rose, K.-A., Manning, E.P., et al. (2021). Integrated Single-Cell Atlas of Endothelial Cells of the Human Lung. *Circulation* *144*, 286–302. 10.1161/CIRCULATIONAHA.120.052318.
41. Lee, H.-W., Xu, Y., He, L., Choi, W., Gonzalez, D., Jin, S.-W., and Simons, M. (2021). Role of Venous Endothelial Cells in Developmental and Pathologic Angiogenesis. *Circulation* *144*, 1308–1322. 10.1161/CIRCULATIONAHA.121.054071.
42. Leu, A.J., Berk, D.A., Lymboussaki, A., Alitalo, K., and Jain, R.K. (2000). Absence of functional lymphatics within a murine sarcoma: a molecular and functional evaluation. *Cancer Res.* *60*, 4324–4327.
43. Padera, T.P., Kadambi, A., di Tomaso, E., Carreira, C.M., Brown, E.B., Boucher, Y., Choi, N.C., Mathisen, D., Wain, J., Mark, E.J., et al. (2002). Lymphatic metastasis in the absence of functional intratumor lymphatics. *Science* *296*, 1883–1886. 10.1126/science.1071420.
44. Crome, S.Q., Nguyen, L.T., Lopez-Verges, S., Yang, S.Y.C., Martin, B., Yam, J.Y., Johnson, D.J., Nie, J., Pniak, M., Yen, P.H., et al. (2017). A distinct innate lymphoid cell population regulates tumor-associated T cells. *Nat. Med.* *23*, 368–375. 10.1038/nm.4278.
45. Corvino, D., Kumar, A., and Bald, T. (2022). Plasticity of NK cells in Cancer. *Front. Immunol.* *13*, 888313. 10.3389/fimmu.2022.888313.
46. Fristedt, R., Borg, D., Hedner, C., Berntsson, J., Nodin, B., Eberhard, J., Micke, P., and Jirström, K. (2016). Prognostic impact of tumour-associated B cells and plasma cells in oesophageal and gastric adenocarcinoma. *J. Gastrointest. Oncol.* *7*, 848–859. 10.21037/jgo.2016.11.07.
47. Li, X., Paulson, T.G., Galipeau, P.C., Sanchez, C.A., Liu, K., Kuhner, M.K., Maley, C.C., Self, S.G., Vaughan, T.L., Reid, B.J., et al. (2015). Assessment of Esophageal Adenocarcinoma Risk Using Somatic Chromosome Alterations in Longitudinal Samples in Barrett's Esophagus. *Cancer Prev. Res. Phila. Pa* *8*, 845–856. 10.1158/1940-6207.CAPR-15-0130.
48. Tickle T, Tirosh I, Georgescu C, Brown M, Haas B (2019). inferCNV of the Trinity CTAT Project.

49. Paulson, T.G., Maley, C.C., Li, X., Li, H., Sanchez, C.A., Chao, D.L., Odze, R.D., Vaughan, T.L., Blount, P.L., and Reid, B.J. (2009). Chromosomal instability and copy number alterations in Barrett's esophagus and esophageal adenocarcinoma. *Clin. Cancer Res. Off. J. Am. Assoc. Cancer Res.* *15*, 3305–3314. 10.1158/1078-0432.CCR-08-2494.
50. Stachler, M.D., Taylor-Weiner, A., Peng, S., McKenna, A., Agoston, A.T., Odze, R.D., Davison, J.M., Nason, K.S., Loda, M., Leshchiner, I., et al. (2015). Paired exome analysis of Barrett's esophagus and adenocarcinoma. *Nat. Genet.* *47*, 1047–1055. 10.1038/ng.3343.
51. Shimshoni, E., Merry, G.E., Milot, Z.D., Oh, C.Y., Horvath, V., Gould, R.A., Caruso, J.A., Chen-Tanyolac, C., Gascard, P., Sangwan, V., et al. (2023). Epithelial-Stromal Interactions in Barrett's Esophagus Modeled in Human Organ Chips. *Gastro Hep Adv.*, S2772572323000444. 10.1016/j.gastha.2023.03.009.
52. Norreen-Thorsen, M., Struck, E.C., Öling, S., Zwahlen, M., Von Feilitzen, K., Odeberg, J., Lindskog, C., Pontén, F., Uhlén, M., Dusart, P.J., et al. (2022). A human adipose tissue cell-type transcriptome atlas. *Cell Rep.* *40*, 111046. 10.1016/j.celrep.2022.111046.
53. Wynn, T.A. (2008). Cellular and molecular mechanisms of fibrosis. *J. Pathol.* *214*, 199–210. 10.1002/path.2277.
54. Wells, R.G. (2008). Cellular sources of extracellular matrix in hepatic fibrosis. *Clin. Liver Dis.* *12*, 759–768, viii. 10.1016/j.cld.2008.07.008.
55. Saadi, A., Das, M., Clemons, N., Zhang, C., Ferguson, M., Tokiwa, G., Serikawa, K., Hardwick, J., Dai, H., Carlini, L., et al. (2014). A potential role for Periostin in Barrett's carcinogenesis. *Cancer Epidemiol. Biomarkers Prev.* *16*, B28.
56. Onieva, J.L., Xiao, Q., Berciano-Guerrero, M.-Á., Laborda-Illanes, A., de Andrea, C., Chaves, P., Piñeiro, P., Garrido-Aranda, A., Gallego, E., Sojo, B., et al. (2022). High IGKC-Expressing Intratumoral Plasma Cells Predict Response to Immune Checkpoint Blockade. *Int. J. Mol. Sci.* *23*, 9124. 10.3390/ijms23169124.
57. Schmidt, M., Micke, P., Gehrmann, M., and Hengstler, J.G. (2012). Immunoglobulin kappa chain as an immunologic biomarker of prognosis and chemotherapy response in solid tumors. *Oncoimmunology* *1*, 1156–1158. 10.4161/onci.21653.
58. Fiore, V.F., Krajnc, M., Quiroz, F.G., Levorse, J., Pasolli, H.A., Shvartsman, S.Y., and Fuchs, E. (2020). Mechanics of a multilayer epithelium instruct tumour architecture and function. *Nature* *585*, 433–439. 10.1038/s41586-020-2695-9.
59. Cross, S.E., Jin, Y.-S., Rao, J., and Gimzewski, J.K. (2007). Nanomechanical analysis of cells from cancer patients. *Nat. Nanotechnol.* *2*, 780–783. 10.1038/nnano.2007.388.
60. Iyer, S., Gaikwad, R.M., Subba-Rao, V., Woodworth, C.D., and Sokolov, I. (2009). Atomic force microscopy detects differences in the surface brush of normal and cancerous cells. *Nat. Nanotechnol.* *4*, 389–393. 10.1038/nnano.2009.77.
61. Butcher, D.T., Alliston, T., and Weaver, V.M. (2009). A tense situation: forcing tumour progression. *Nat. Rev. Cancer* *9*, 108–122. 10.1038/nrc2544.

62. Kennedy-Darling, J., Bhate, S.S., Hickey, J.W., Black, S., Barlow, G.L., Vazquez, G., Venkatarahaman, V.G., Samusik, N., Goltsev, Y., Schürch, C.M., et al. (2021). Highly multiplexed tissue imaging using repeated oligonucleotide exchange reaction. *Eur. J. Immunol.* *51*, 1262–1277. 10.1002/eji.202048891.
63. Black, S., Phillips, D., Hickey, J.W., Kennedy-Darling, J., Venkatarahaman, V.G., Samusik, N., Goltsev, Y., Schürch, C.M., and Nolan, G.P. (2021). CODEX multiplexed tissue imaging with DNA-conjugated antibodies. *Nat. Protoc.* *16*, 3802–3835. 10.1038/s41596-021-00556-8.
64. Hickey, J.W., Neumann, E.K., Radtke, A.J., Camarillo, J.M., Beuschel, R.T., Albanese, A., McDonough, E., Hatler, J., Wiblin, A.E., Fisher, J., et al. (2022). Spatial mapping of protein composition and tissue organization: a primer for multiplexed antibody-based imaging. *Nat. Methods* *19*, 284–295. 10.1038/s41592-021-01316-y.
65. Hickey, J.W., Becker, W.R., Nevins, S.A., Horning, A., Perez, A.E., Chiu, R., Chen, D.C., Cotter, D., Esplin, E.D., Weimer, A.K., et al. (2021). 35672395. 2021.11.25.469203. 10.1101/2021.11.25.469203.
66. Souza, R.F., and Spechler, S.J. (2022). Mechanisms and pathophysiology of Barrett oesophagus. *Nat. Rev. Gastroenterol. Hepatol.* *19*, 605–620. 10.1038/s41575-022-00622-w.
67. Hickey, J.W., Tan, Y., Nolan, G.P., and Goltsev, Y. (2021). Strategies for Accurate Cell Type Identification in CODEX Multiplexed Imaging Data. *Front. Immunol.* *12*, 727626. 10.3389/fimmu.2021.727626.
68. D'Alessio, F.R., Tsushima, K., Aggarwal, N.R., West, E.E., Willett, M.H., Britos, M.F., Pipeling, M.R., Brower, R.G., Tuder, R.M., McDyer, J.F., et al. (2009). CD4+CD25+Foxp3+ Tregs resolve experimental lung injury in mice and are present in humans with acute lung injury. *J. Clin. Invest.* *119*, 2898–2913. 10.1172/JCI36498.
69. DeFilippis, R.A., Chang, H., Dumont, N., Rabban, J.T., Chen, Y.-Y., Fontenay, G.V., Berman, H.K., Gauthier, M.L., Zhao, J., Hu, D., et al. (2012). CD36 repression activates a multicellular stromal program shared by high mammographic density and tumor tissues. *Cancer Discov.* *2*, 826–839. 10.1158/2159-8290.CD-12-0107.
70. McDonald, S.A.C., Graham, T.A., Lavery, D.L., Wright, N.A., and Jansen, M. (2015). The Barrett's Gland in Phenotype Space. *Cell. Mol. Gastroenterol. Hepatol.* *1*, 41–54. 10.1016/j.jcmgh.2014.10.001.
71. Calon, A., Tauriello, D.V.F., and Batlle, E. (2014). TGF-beta in CAF-mediated tumor growth and metastasis. *Semin. Cancer Biol.* *25*, 15–22. 10.1016/j.semcancer.2013.12.008.
72. DeFilippis, R.A., Fordyce, C., Patten, K., Chang, H., Zhao, J., Fontenay, G.V., Kerlikowske, K., Parvin, B., and Tlsty, T.D. (2014). Stress signaling from human mammary epithelial cells contributes to phenotypes of mammographic density. *Cancer Res.* *74*, 5032–5044. 10.1158/0008-5472.CAN-13-3390.
73. Hao, Y., Triadafilopoulos, G., Sahbaie, P., Young, H.S., Omary, M.B., and Lowe, A.W. (2006). Gene expression profiling reveals stromal genes expressed in common between Barrett's esophagus and adenocarcinoma. *Gastroenterology* *131*, 925–933. 10.1053/j.gastro.2006.04.026.

74. Tilman, G., Mattiussi, M., Brasseur, F., van Baren, N., and Decottignies, A. (2007). Human periostin gene expression in normal tissues, tumors and melanoma: evidences for periostin production by both stromal and melanoma cells. *Mol. Cancer* 6, 80. 10.1186/1476-4598-6-80.
75. Park, J., and Scherer, P.E. (2012). Endotrophin - a novel factor linking obesity with aggressive tumor growth. *Oncotarget* 3, 1487–1488. 10.18632/oncotarget.796.
76. Williams, L., Layton, T., Yang, N., Feldmann, M., and Nanchahal, J. (2022). Collagen VI as a driver and disease biomarker in human fibrosis. *FEBS J.* 289, 3603–3629. 10.1111/febs.16039.
77. Davidson, S., Efremova, M., Riedel, A., Mahata, B., Pramanik, J., Huuhtanen, J., Kar, G., Vento-Tormo, R., Hagai, T., Chen, X., et al. (2020). Single-Cell RNA Sequencing Reveals a Dynamic Stromal Niche That Supports Tumor Growth. *Cell Rep.* 31, 107628. 10.1016/j.celrep.2020.107628.
78. Fuhrmann, A., Staunton, J.R., Nandakumar, V., Banyai, N., Davies, P.C.W., and Ros, R. (2011). AFM stiffness nanotomography of normal, metaplastic and dysplastic human esophageal cells. *Phys. Biol.* 8, 015007. 10.1088/1478-3975/8/1/015007.
79. Northcott, J.M., Dean, I.S., Mouw, J.K., and Weaver, V.M. (2018). Feeling Stress: The Mechanics of Cancer Progression and Aggression. *Front. Cell Dev. Biol.* 6, 17. 10.3389/fcell.2018.00017.
80. Li, J., Tan, J., Martino, M.M., and Lui, K.O. (2018). Regulatory T-Cells: Potential Regulator of Tissue Repair and Regeneration. *Front. Immunol.* 9, 585. 10.3389/fimmu.2018.00585.
81. Lagisetty, K.H., McEwen, D.P., Nancarrow, D.J., Schiebel, J.G., Ferrer-Torres, D., Ray, D., Frankel, T.L., Lin, J., Chang, A.C., Kresty, L.A., et al. (2021). Immune determinants of Barrett's progression to esophageal adenocarcinoma. *JCI Insight* 6, e143888, 143888. 10.1172/jci.insight.143888.
82. Gokon, Y., Fujishima, F., Taniyama, Y., Ishida, H., Yamagata, T., Sawai, T., Uzuki, M., Ichikawa, H., Itakura, Y., Takahashi, K., et al. (2020). Immune microenvironment in Barrett's esophagus adjacent to esophageal adenocarcinoma: possible influence of adjacent mucosa on cancer development and progression. *Virchows Arch. Int. J. Pathol.* 477, 825–834. 10.1007/s00428-020-02854-0.
83. Wang, Z., Xiong, S., Mao, Y., Chen, M., Ma, X., Zhou, X., Ma, Z., Liu, F., Huang, Z., Luo, Q., et al. (2016). Periostin promotes immunosuppressive premetastatic niche formation to facilitate breast tumour metastasis. *J. Pathol.* 239, 484–495. 10.1002/path.4747.
84. Gowhari Shabgah, A., Haleem Al-Qaim, Z., Markov, A., Valerievich Yumashev, A., Ezzatifar, F., Ahmadi, M., Mohammad Gheibihayat, S., and Gholizadeh Navashenaq, J. (2021). Chemokine CXCL14; a double-edged sword in cancer development. *Int. Immunopharmacol.* 97, 107681. 10.1016/j.intimp.2021.107681.
85. Morra, L., and Moch, H. (2011). Periostin expression and epithelial-mesenchymal transition in cancer: a review and an update. *Virchows Arch. Int. J. Pathol.* 459, 465–475. 10.1007/s00428-011-1151-5.

86. Martin, M. Cutadapt Removes Adapter Sequences From High-Throughput Sequencing Reads. *EMBnet.journal* 17, 10–12. 10.14806/ej.17.1.200.
87. Bray, N.L., Pimentel, H., Melsted, P., and Pachter, L. (2016). Near-optimal probabilistic RNA-seq quantification. *Nat. Biotechnol.* 34, 525–527. 10.1038/nbt.3519.
88. Melsted, P., Boeshaghi, A.S., Liu, L., Gao, F., Lu, L., Min, K.H., da Veiga Beltrame, E., Hjørleifsson, K.E., Gehring, J., and Pachter, L. (2021). Modular, efficient and constant-memory single-cell RNA-seq preprocessing. *Nat. Biotechnol.* 39, 813–818. 10.1038/s41587-021-00870-2.
89. Wolf, F.A., Angerer, P., and Theis, F.J. (2018). SCANPY: large-scale single-cell gene expression data analysis. *Genome Biol.* 19, 15. 10.1186/s13059-017-1382-0.
90. Wolock, S.L., Lopez, R., and Klein, A.M. (2019). Scrublet: Computational Identification of Cell Doublets in Single-Cell Transcriptomic Data. *Cell Syst.* 8, 281-291.e9. 10.1016/j.cels.2018.11.005.
91. Zheng, G.X.Y., Terry, J.M., Belgrader, P., Ryvkin, P., Bent, Z.W., Wilson, R., Ziraldo, S.B., Wheeler, T.D., McDermott, G.P., Zhu, J., et al. (2017). Massively parallel digital transcriptional profiling of single cells. *Nat. Commun.* 8, 14049. 10.1038/ncomms14049.
92. McInnes, L., Healy, J., and Melville, J. (2018). UMAP: Uniform Manifold Approximation and Projection for Dimension Reduction. *ArXiv180203426 Cs Stat.*
93. Wolf, F.A., Hamey, F.K., Plass, M., Solana, J., Dahlin, J.S., Göttgens, B., Rajewsky, N., Simon, L., and Theis, F.J. (2019). PAGA: graph abstraction reconciles clustering with trajectory inference through a topology preserving map of single cells. *Genome Biol.* 20, 59. 10.1186/s13059-019-1663-x.
94. Traag, V.A., Waltman, L., and van Eck, N.J. (2019). From Louvain to Leiden: guaranteeing well-connected communities. *Sci. Rep.* 9, 5233. 10.1038/s41598-019-41695-z.
95. Speir, M.L., Bhaduri, A., Markov, N.S., Moreno, P., Nowakowski, T.J., Papatheodorou, I., Pollen, A.A., Raney, B.J., Seninge, L., Kent, W.J., et al. (2021). UCSC Cell Browser: visualize your single-cell data. *Bioinformatics* 37, 4578–4580. 10.1093/bioinformatics/btab503.
96. Osumi-Sutherland, D., Xu, C., Keays, M., Levine, A.P., Kharchenko, P.V., Regev, A., Lein, E., and Teichmann, S.A. (2021). Cell type ontologies of the Human Cell Atlas. *Nat. Cell Biol.* 23, 1129–1135. 10.1038/s41556-021-00787-7.
97. Madisson, E., Wilbrey-Clark, A., Miragaia, R.J., Saeb-Parsy, K., Mahbubani, K.T., Georgakopoulos, N., Harding, P., Polanski, K., Huang, N., Nowicki-Osuch, K., et al. (2019). scRNA-seq assessment of the human lung, spleen, and esophagus tissue stability after cold preservation. *Genome Biol.* 21, 1. 10.1186/s13059-019-1906-x.
98. Yang, S., Corbett, S.E., Koga, Y., Wang, Z., Johnson, W.E., Yajima, M., and Campbell, J.D. (2020). Decontamination of ambient RNA in single-cell RNA-seq with DecontX. *Genome Biol.* 21, 57. 10.1186/s13059-020-1950-6.

99. Büttner, M., Ostner, J., Müller, C.L., Theis, F.J., and Schubert, B. (2021). scCODA is a Bayesian model for compositional single-cell data analysis. *Nat. Commun.* *12*, 6876. 10.1038/s41467-021-27150-6.
100. Sturm, G. (2022). infercnvpy: Scanpy plugin to infer copy number variation (CNV) from single-cell transcriptomics data.
101. Data-independent acquisition and quantification of extracellular matrix from human lung in chronic inflammation-associated carcinomas - PubMed <https://pubmed.ncbi.nlm.nih.gov/36228107/>.
102. Escher, C., Reiter, L., MacLean, B., Ossola, R., Herzog, F., Chilton, J., MacCoss, M.J., and Rinner, O. (2012). Using iRT, a normalized retention time for more targeted measurement of peptides. *Proteomics* *12*, 1111–1121. 10.1002/pmic.201100463.
103. Gillet, L.C., Navarro, P., Tate, S., Röst, H., Selevsek, N., Reiter, L., Bonner, R., and Aebersold, R. (2012). Targeted data extraction of the MS/MS spectra generated by data-independent acquisition: a new concept for consistent and accurate proteome analysis. *Mol. Cell. Proteomics MCP* *11*, O111.016717. 10.1074/mcp.O111.016717.
104. Collins, B.C., Hunter, C.L., Liu, Y., Schilling, B., Rosenberger, G., Bader, S.L., Chan, D.W., Gibson, B.W., Gingras, A.-C., Held, J.M., et al. (2017). Multi-laboratory assessment of reproducibility, qualitative and quantitative performance of SWATH-mass spectrometry. *Nat. Commun.* *8*, 291. 10.1038/s41467-017-00249-5.
105. Schilling, B., Gibson, B.W., and Hunter, C.L. (2017). Generation of High-Quality SWATH® Acquisition Data for Label-free Quantitative Proteomics Studies Using TripleTOF® Mass Spectrometers. *Methods Mol. Biol. Clifton NJ* *1550*, 223–233. 10.1007/978-1-4939-6747-6_16.
106. Rosenberger, G., Koh, C.C., Guo, T., Röst, H.L., Kouvonen, P., Collins, B.C., Heusel, M., Liu, Y., Caron, E., Vichalkovski, A., et al. (2014). A repository of assays to quantify 10,000 human proteins by SWATH-MS. *Sci. Data* *1*, 140031. 10.1038/sdata.2014.31.
107. Storey, J.D. (2002). A direct approach to false discovery rates. *J. R. Stat. Soc. Ser. B Stat. Methodol.* *64*, 479–498.
108. Lee, M.Y., Bedia, J.S., Bhate, S.S., Barlow, G.L., Phillips, D., Fantl, W.J., Nolan, G.P., and Schürch, C.M. (2022). CellSeg: a robust, pre-trained nucleus segmentation and pixel quantification software for highly multiplexed fluorescence images. *BMC Bioinformatics* *23*, 46. 10.1186/s12859-022-04570-9.
109. Bhate, S.S., Barlow, G.L., Schürch, C.M., and Nolan, G.P. (2022). Tissue schematics map the specialization of immune tissue motifs and their appropriation by tumors. *Cell Syst.* *13*, 109-130.e6. 10.1016/j.cels.2021.09.012.
110. Schürch, C.M., Bhate, S.S., Barlow, G.L., Phillips, D.J., Noti, L., Zlobec, I., Chu, P., Black, S., Demeter, J., McIlwain, D.R., et al. (2020). Coordinated Cellular Neighborhoods Orchestrate Antitumoral Immunity at the Colorectal Cancer Invasive Front. *Cell* *182*, 1341-1359.e19. 10.1016/j.cell.2020.07.005.

Figure Legends

Graphical Abstract. To obtain a comprehensive picture of the coordinated changes in epithelial, stromal and immune compartments during development of Barrett's-associated esophageal adenocarcinoma, patient-matched samples corresponding to various phases of disease progression were collected from 12 patients, each of which had at a given time point lesions at multiple stages progression (matched-normal, metaplasia, dysplasia, and carcinoma). Matched "normal" gastric tissues were also collected. These sample were analyzed by single cell RNA-sequencing (scRNAseq) for single-cell resolution transcriptomics and Copy Number Variant (CNV), by proteomics for extracellular matrix (ECM) proteins, by Atomic Force Microscopy (AFM for tissue stiffness and by CODEX spatial proteomics imaging. The integrative multi-omics analysis exposed drastic alterations in cell type composition and shifts in cell states in all three compartments. A large subpopulation of fibroblasts absent in the normal esophagus and characteristic of dysplasia and adenocarcinoma sample, that based on markers would indeed be considered cancer associated fibroblasts (CAF), appeared already in the metaplastic phase. This fibroblast subpopulation had transcriptomes virtually indistinguishable with fibroblasts of the cancer free gastric epithelium in these patients

Main Figures

Figure 1. Integrated multiomics analysis of the progression of Barrett's Esophagus (BE) to esophageal adenocarcinoma (EA). (A) Example of a surgical resection showing locations of samples representing the phases of disease progression and use in multiomic-analyses. (B) Gene markers (transcripts) used for classification of coarse-grained cell types from scRNAseq data. (C) UMAP visualization of the entirety of cells from all samples analyzed by scRNAseq color-labelled for clusters (Leiden unsupervised clustering), the coarse-grained cell types, tissue diagnosis, and patient IDs (clockwise from top left) obtained from scRNAseq. (D) UMAP visualization of all analyzed cells from all samples obtained from scRNAseq, color-labelled for the fine-grained cell type.

Figure 2. Overview of pseudo-bulk analysis. (A) Principal component analysis (PCA) displaying showing PC2 (x-axis) and PC3 (y-axis) of samples using pseudo-bulk transcriptome profiles for all cells (left panel), gastrointestinal (GI) epithelial cells (middle left panel), stromal cells (fibroblasts and endothelial cells) (middle right panel), and immune cells (T cells, B cells, Monocyte derived, Natural Killer (NK) cells, and dendritic cells (DC) (right panel)). Colors indicate the tissue diagnosis. (B) Heat maps showing changes in expression levels of selected genes (from left to right) for various pseudo-bulk schemes: all cells combined, gastro-intestinal (GI) epithelial cells, fibroblasts, endothelial cells and CD8 T cells at each phase of disease progression. (C) Heat map showing changes in expression levels of genes related to TGF-beta signaling in fibroblasts at each phase of disease progression.

Figure 3. Stromal and immune cell subtype composition changes during BE progression. (A) fibroblasts, (B) myofibroblasts, (C) endothelial cells, (D) T/Natural Killer (NK) cells, (E) myeloid cells (macrophages, monocytes, dendritic cells (DCs) and neutrophils), and (F) B/Plasma cells. **First column panels:** UMAP of cells from the respective cell type (including all diagnoses), color-coded by transcriptional cluster. **Second column panels:** Composition of

cells with respect to cluster (subtype) membership, for each “diagnosis” (=phase of progression)/tissue with same color codes as in UMAPs. **Third column panels:** Selected marker genes for clusters of interest. **Fourth Column panels:** TOP subpanel: Statistically significant enrichment (red) or depletion (blue) of a cellular subtype at each diagnosis (compared to *mNE*, determined by scCODA, Methods). BOTTOM panel: Composition of cells with respect to the diagnoses, for each transcriptional cluster (subtype).

Figure 4. Large CNVs are markers of BE progression to malignancy. (A) For each epithelial cell of each sample (horizontal axis) representing the phases of progression (color labels), the CNV burden (vertical axis) was estimated based on inferred CNVs from scRNAseq (Methods). Most tumor samples contained cells with significantly increased CNV score compared to the *mNE/mNS* samples (black horizontal line: 99% quantile of CNV score in *mNE/mNS* cells). (B) Number of cells with (black) and without (grey) CNVs, according to cell type (left panel) and to disease progression phase (right panel). Large CNVs were restricted to the epithelial compartment and appeared at the dysplastic phase. (C,D) CNVs for tumor E21 inferred from scRNAseq (C) and were consistent with CNVs obtained from scDNAseq (D). (E) UMAP of epithelial cells in transcriptome space with each cell’s CNV cluster membership identified in (C) shown in color (grey: CNVs absent). CNV clusters closely mimic transcriptional clusters.

Figure 5. Proteomic analysis and Atomic Force Microscopy (AFM) reveal changes in the extracellular matrix composition and tissue mechanics during BE progression. (A) Number of matrixome or matrixome-associated proteins detected by ECM proteomics grouped by protein class. (B) PCA of proteomic samples (*mNE*: green; *T*: red) shows differences in ECM-enriched protein extract composition between *mNE* and *T* samples. (C) Differential ECM protein abundances between *mNE* and *T* samples shows 43 and 55 proteins upregulated and downregulated in *T* compared to *mNE*, respectively. Proteins with the highest up/down-regulation in *T* vs. *mNE* are identified. (D) Positive correlation between ECM proteomic- (*y*-axis) and respective scRNAseq (*x*-axis) fold-changes in matched samples. Proteins of interest are highlighted in red font. (E) Expression of significantly down-regulated (top panel) and up-regulated (bottom panel) proteins identified by proteomic analysis (see C) grouped by scRNAseq cell type (including cells from all diagnoses). (F) Quantification of epithelium and stroma stiffness using AFM in a distinct cohort for the phases of progression, shown as violin plots. Each color represents an esophageal sample at a different phase from a given patient; included are here also samples from tumor-free individuals (“true normal”) as opposed to the matched-normal” samples from EA patients. Donors: *n*=3, for matched normal esophagus, esophagus metaplasia, and dysplasia; *n*=4, for esophageal cancer and true normal esophagus; *n*=2 for matched normal stomach. Two-way Anova test with Tukey post hoc test was used as statistical test. Thick and thin dashed lines represent median and quartiles in the distribution, respectively. *n* = 50-150 regions per patient, ns: not significant, **** *p* <0.001.

Figure 6. CODEX multiplexed proteomic imaging identifies epithelial and stromal tissue structures, exposing cell state changes. (A) Representative images of *mNE*, *M*, *D* and *T* esophageal tissues from one patient (of a total of 5) from CODEX multiplexed fluorescent imaging for 6 of the 54 markers queried (scale bar = 500 μ m) and corresponding (B) coarse-grained, CODEX-defined epithelial cell types mapped back to tissue coordinates. (C) Neighborhood (NH) maps for *mNE* and *M*. (D) Percentage of metaplasia, as determined by a pathologist (*y*-axis) versus percentage of the “Specialized” NH from CODEX analysis of each of the 27 regions imaged (*x*-axis). (E) Magnified region of NH map for *M* sample shown in C (scale bar = 100 μ m). (F) Community (neighborhood of neighborhoods) maps for representative *mNE* (left panel) and *M* (right panel) samples. (G) Percentage of squamous (*mNE*) esophagus,

metaplasia (*M*), high grade dysplasia (HGD), and invasive EAC epithelium as determined by a pathologist (*y*-axis) versus percentage of community determined by CODEX for each of the 27 regions imaged (*x*-axis). **(H-J)** Cell type composition for each of the 4 communities (*mNE*: grey; *M*: purple; *D*: green; *T*: pink) that correlated with diseased epithelial in panel G, broken down by (H) epithelial, (I) immune, and (J) mesenchymal groupings. Percentages are provided in Suppl.Table S10. **(K)** cell-cell interaction analysis with $-\log(p\text{-value})$ for each cell type pair compared to 10,000 random permutations, colored by overall disease state. **(L-N)** Representative images of the phases or progression: *mNE* (panel L), *D* (M), and *T* (N) from one donor (5 donors total) from CODEX imaging for 6 of the 54 markers queried (scale bar = 500 μm) and of magnified regions (scale bar = 50 μm). **(O)** Shannon's Diversity for cell types and proportions within each CODEX-defined community. **(P)** Schematic representation of overall changes in epithelial and stromal connections.

Supplemental Figures

Figure S1. Description of clinical samples and multi-omics analyses conducted. **(A)** Table describing the samples analyzed in this study including sampling method (surgical resection (SR) or endoscopic biopsy (B)), tissue diagnosis (*mNE*: matched Normal Esophagus, *M*: Barrett's metaplasia, *D*: dysplasia, *T*: tumor, *mNS*: matched Normal Stomach - other abbreviations indicate a mixture of tissue types), type of analysis performed and specimen ID. **(B)** Selection of pathohistological images of scanned hematoxylin and eosin-stained tissue sections independently assessed by two expert esophageal pathologists to confirm tissue diagnosis.

Figure S2. Overview of sample space and global cell type survey. **(A)** UMAP visualization for non-batch corrected scRNAseq data of all analyzed cells across all histological diagnoses (progression phases), color-coded by cluster. Note that the non-batch corrected data show separation into patient-specific cancer cells. **(B)** UMAP visualization for batch corrected scRNAseq data of all analyzed cells across all histological diagnoses, color-coded by cluster. **(C)** Cells color-coded for predicted cell cycle phase (Methods). Subsets of epithelial tumor cells and T cells appear highly proliferative (G2M phase, green). **(D)** Fraction of proliferating cells (S or G2M phase) color-coded for each patient for each cell type and phase of progression (diagnosis). Error bars denote 5% and 95% Bayesian credibility intervals of a binomial model.

Figure S3. Cell type-specific signatures of gene expression changes during BE progression. Differential gene expression at each phase of progression (diagnosis) based on pseudo-bulk transcriptomes, for 8 major cell types. The observed gene expression patterns specific for various cellular compartments illustrate profound epithelial, stromal and immune tissue alterations associated with disease progression.

Figure S4. Cell type composition changes during BE progression. **(A)** TOP: Clustering of individual samples based on cell type composition (proportions) Each sample's diagnosis is indicated above the dendrogram. BOTTOM: Epithelial, stromal and immune percentages of each sample (aggregated from cell type proportions used for clustering) are shown in the heatmap below the dendrogram. **(B)** Sample level PCA performed with pseudo-bulk gene expression measures showed that the variation in the PCA was largely due to variation in cell type quantities as shown by correlation with the principal coordinates and cell type proportions across samples. **(C)** Cell type proportions (as shown in A) collapsed by diagnosis. **(D)** Significant changes in cell type composition across diagnoses. Statistically significant changes with respect to *mNE* (determined by scCODA, see Methods) are shown above the bar graph

(red: upregulated, blue: down-regulated). **(E)** Normalized expression of differentiation markers in epithelial cells across the different phases of disease progression shows a loss of differentiation at the D/T phase of progression.

Figure S5. Copy number profile (A) and distribution of copy number clusters/clones across samples and diagnoses (B) inferred from scRNAseq. While dysplastic (*D*) cells (samples E07C and E07D1) form their own CNV clusters (clones 18 and 37), cells from matched *T* (sample E07B) show similar CNVs (clone 21), e.g., a gain of chr6p and a loss of chr6q indicating a clonal relationship between *D* and *T*.

Figure S6. Protein abundance changes in EAC (*T*) compared to matched normal esophagus (*mNE*). **(A)** Top 10 proteins with most altered abundance detected in ECM-enriched samples or *T* vs. *mNE* tissues. **(B)** Core matrixosomal protein signatures altered in *T* versus *mNE*.

Figure S7. (A) Identification of likely cell source of proteins with altered abundances during BE progression. Gene expression fold changes in scRNAseq pseudo-bulk analysis were queried for proteins that were identified as differentially abundant in the ECM proteomic analysis, i.e., either decreased (left panel) or increased (right panel) in *T* vs. *mNE*, respectively (Fig. 5 and Table S5). Cell type specificity and abundance for each transcript is displayed as circles (color-coded for cell type and size-scaled for cell abundance). **(B)** Plots with changes in mRNA expression of periostin (POSTN) inferred from scRNAseq data, grouped by cell type and diagnosis, reveals complexity changes that depends on cell source (shown in A).

Figure S8. AFM mechanics is consistent with a shift in tissue identity from squamous esophagus to BE (esophagus to stomach).

(A) Workflow of sample preparation for AFM stiffness measurements. **(B)** Stromal and epithelial esophagus stiffness gradients were compared at various phases of progression to EAC. Representative H&E images and corresponding AFM stiffness maps showing difference between stroma and epithelium stiffness at different phases of esophageal cancer progression and comparison with matched normal squamous esophagus (i.e., *mNE* adjacent to *BE* and tumor) and true normal (disease-free) squamous esophagus tissues. Dashed lines indicate the interface between stroma (*S*) and epithelium (*E*). Scales: 200 μ m.

Figure S9. Cell type-specific analysis from CODEX multiplexed proteomics imaging of samples corresponding to disease progression phases of BE-associated EAC.

(A) Schematic for overall approach to image tissues with CODEX imaging. **(B)** Representative H&E image taken after CODEX imaging with percentage of diagnosis (based on epithelial cell histology) labeled by pathologists. **(C-D)** Quantification of epithelial percentage (*y*-axis) for each overall (C) sub and (D) major diagnosis by pathologist from the H&E stain of the tissue section following CODEX multiplexed imaging. **(E)** Average protein expression (*x*-axis) by cell type (*y*-axis) derived from the clustered CODEX multiplexed imaging data. **(F)** Epithelial cell type percentages across the different disease phases as diagnosed by pathologists.

Figure S10. Comparison of cell type abundances across patients analyzed by both scRNAseq (A, C) (clinical samples) and CODEX (B, D) (adjacent tissue regions) grouped by sample (A, B) and diagnosis (C, D).

Figure S11. Multicellular Neighborhood (NH) analysis by CODEX imaging reveals multicellular neighborhood tissue reorganization during the progression of BE to EAC.

(A) Maps of multicellular neighborhoods mapped back to original coordinates for one

representative patient (5 patients total). **(B)** Definition of NHs based on cell types enrichment (red) or depletion (blue) within individual neighborhoods identified in Figure S8E. Rows represent hence -identified NHs, and their name given on the left. **(C)** Percentage of “Apical Squamous” NH within the different progression phases. **(D)** Average percentage of the epithelial neighborhoods within each of the phases as determined by a pathologist post H&E staining. **(E)** Percentage of high-grade (HG) dysplastic epithelium as determined by a pathologist (*y*-axis) versus percentage of “Stroma and Neutrophil” NH determined by CODEX for each of the 27 regions imaged. **(F)** Percentage of “Specialized” NH within the different disease phases. **(G)** Percentage of epithelial cell types within the “Specialized” NH.

Figure S12. Community (Neighborhood of neighborhoods) analysis of CODEX imaging illustrates the dynamic rearrangements of intricate epithelial-stromal cell entities during BE progression. **(A)** Percentage of epithelial cells as determined by a pathologist (*y* axis) versus percentage of the neighborhoods as determined by CODEX for each of the 27 regions imaged with correlations. **(B)** Neighborhoods enriched or depleted within individual communities identified. **(C)** Maps of communities mapped back to original coordinates for one representative example donor. Community color code is the same as in B. **(D-E)** Percentage of cell type within each community that correlated with pathologist-classified epithelium for (D) epithelial cell types and (E) neutrophils. **(F)** Percentage of neighborhoods within each community that correlated with pathologist-classified epithelium. **(G-H)** Percentage of cell type within each community that correlated with pathologist-classified epithelium for (G) macrophage phenotypes and (H) CD4+ Tregs. **(I)** Percentage of CD4+ Tregs in progression phases. **(J)** Percentage of CD4+ Tregs versus percentage of CD36hi endothelial cells within the same sample imaged.

Figure S13. Cell-cell interaction analysis from CODEX images reveals dynamic and increasingly diverse cell interaction pairs during BE progression. **(A-C)** Significant (average *p*-value <0.05) cell-cell interactions shown for (A) metaplasia, (B) dysplasia, and (C) tumor classified samples. **(D)** Cell-cell pairs found enriched in *M*, *D* and *T* disease phases with dashed line representing a *p* value of 0.05. **(E-F)** Percentage of (E) plasma cells and (F) CD36hi endothelial cells found across different disease phases. **(G-I)** Subset of cells identified by CODEX imaging replotted to tissue coordinates for (G) metaplasia, (H) dysplasia, and (I) tumor samples.

Supplemental Tables

Table S1. Patient and biosample metadata. Patient information, biosample descriptions, and histological diagnosis are provided for 64 samples.

Table S2. Coarse grained differentially expressed genes. For each of 16 coarse grained cell types, differential expression was calculated comparing phases of progressing with DESeq2 and the pseudo-bulk transcriptomes per biosample. Results were filtered through association testing with the ambient RNA from empty droplets.

Table S3. Fine grained gene markers. Gene markers of fine grained cell types based on statistical differential expression analysis between clusters.

Table S4. Fibroblast pathway signature scores. Using the DEGs of fibroblasts, B cells, natural killer cells (NK) and monocyte-derived cells, selected pathways were tested for association using Enrichr. Inputs were DEGs filtered to have at least a log₂ fold change of 0.58 and adjusted p-value of 0.05.

Table S5. Patient cell counts. From the single cell RNA-seq data, counts of both coarse grain and fine grained cell types per patient.

Table S6. ECM Proteomic differential abundance statistics. Comparing ECM protein abundance between pooled Tumor (T) samples versus matched Normal Esophagus (mNE) samples using paired T-tests with multiple testing correction.

Table S7. ECM Proteomics DIA isolation scheme. Samples were analyzed for ECM protein abundance by data-independent acquisition (DIA) using variable-sized windows covering the m/z 400-1,250 range.

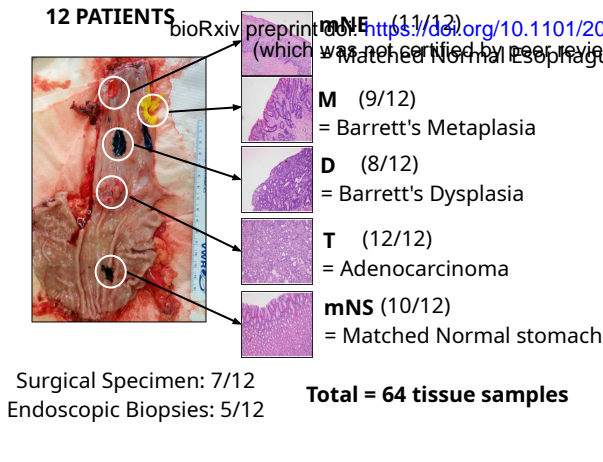
Table S8. CODEX Pathology concordance. Using imaging data from 5 human donors, three pathologists independently evaluated the H&E staining of the sections performed on the same tissue sections that were used for the CODEX multiplexed imaging. Pathologist scores were then aggregated and averaged for disease phase granular diagnosis (e.g., mNE, mNS, M), and estimated percentages of type of epithelium in each image (e.g., % squamous, % metaplasia, % dysplasia, % tumor).

Table S9. CODEX antibody information. The antibody panels used in generating CODEX data were chosen to include targets that identify subtypes of intestinal epithelium and stromal cells, and cells of the innate and adaptive immune system.

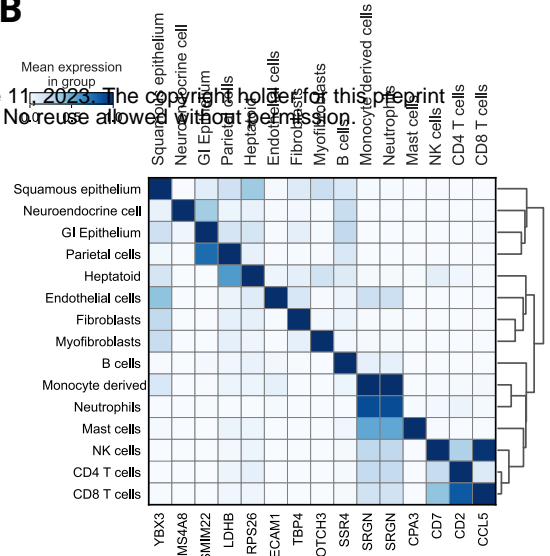
Table S10. CODEX communities. Percentages of cell type composition for each of the 4 communities (mNE: grey; M: purple; D: green; T: pink) that correlated with diseased epithelial, broken down by epithelial, immune, and mesenchymal groupings.

Table S11. CODEX neighborhood analysis. Spatial neighborhood (NH) information was used for cell-cell interaction statistics across progression phases (M, D, T). The frequency of neighbors, using a nearest neighbor approach, was compared to the frequency of occurrences in null-models, achieved by 10,000 permutations of cell type locations.

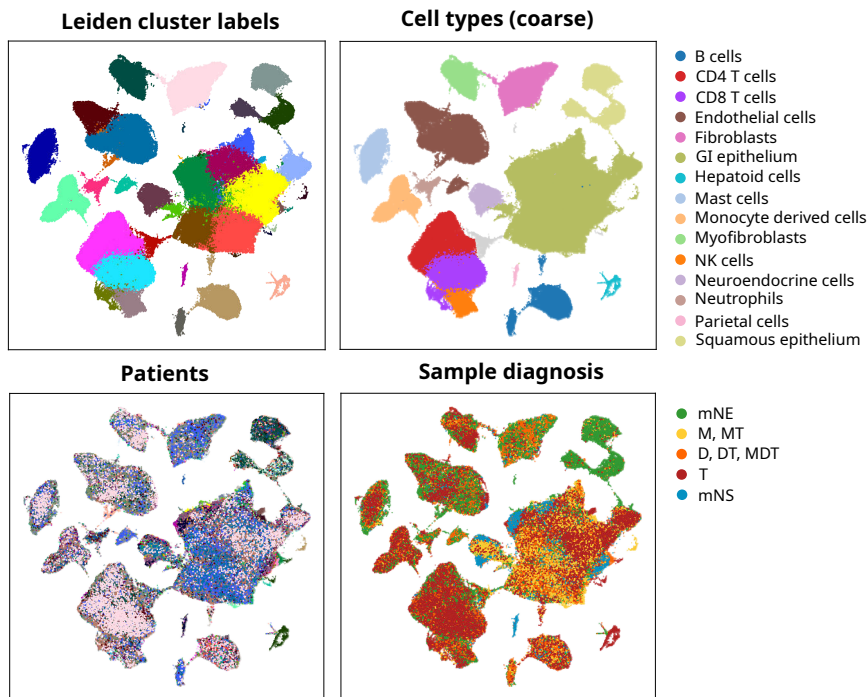
A



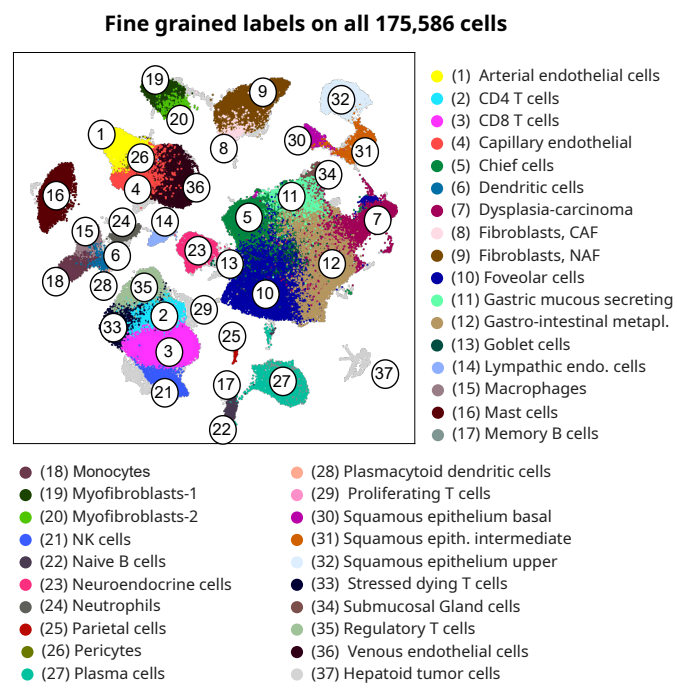
B



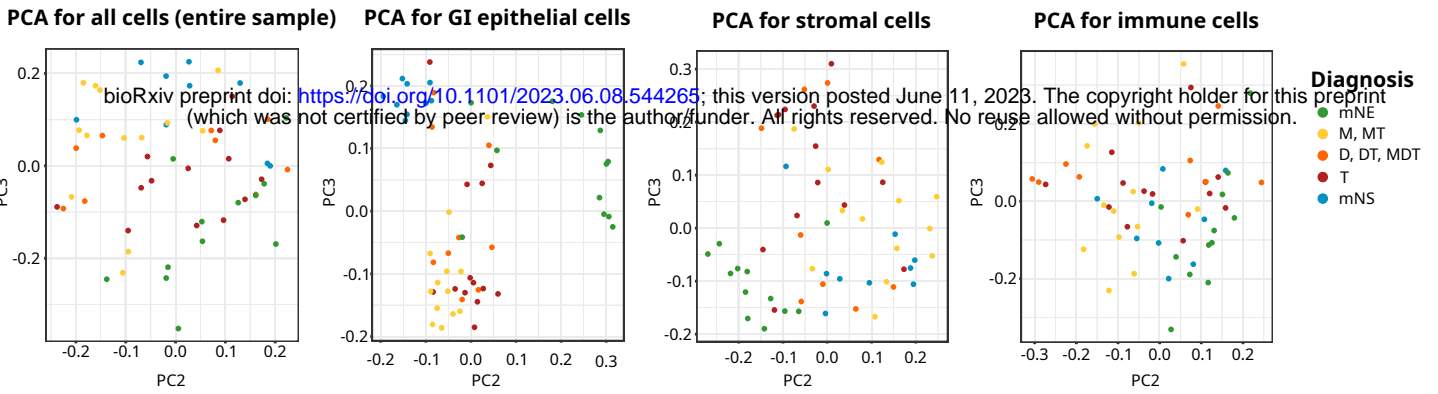
C



D

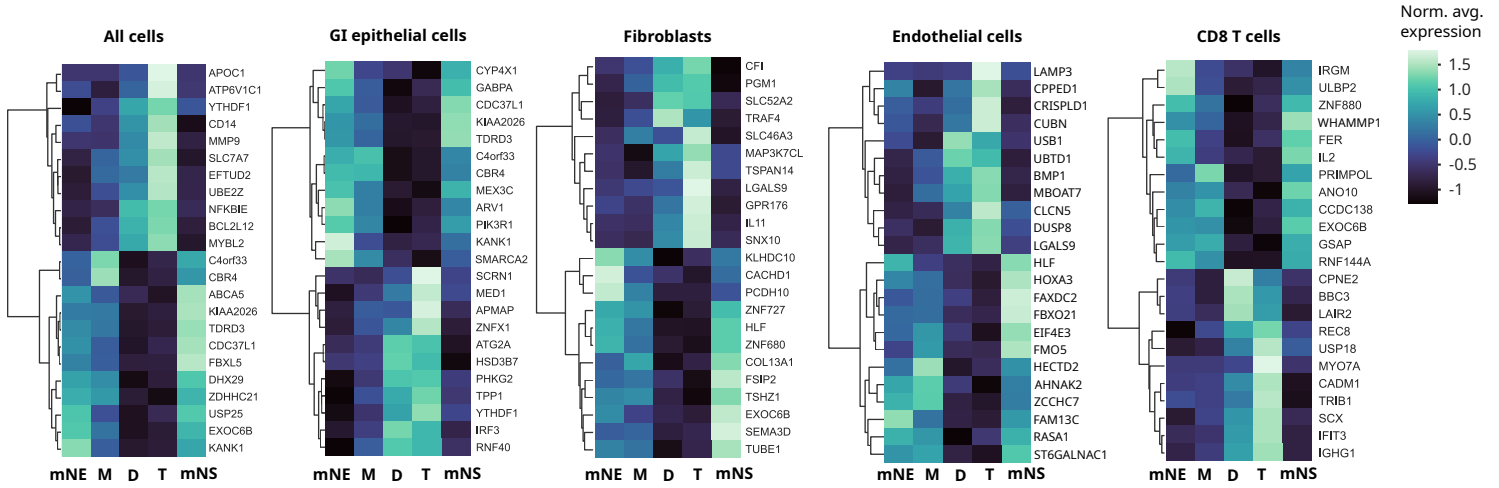


Sample grouping by similarity of pseudo-bulk-transcriptome

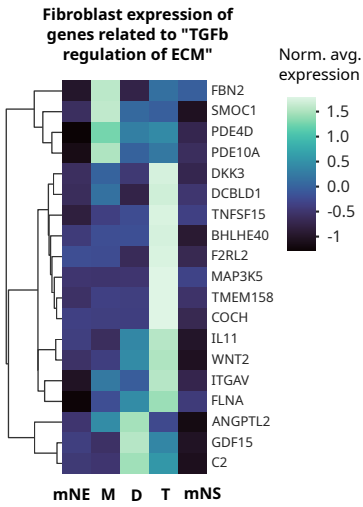


B

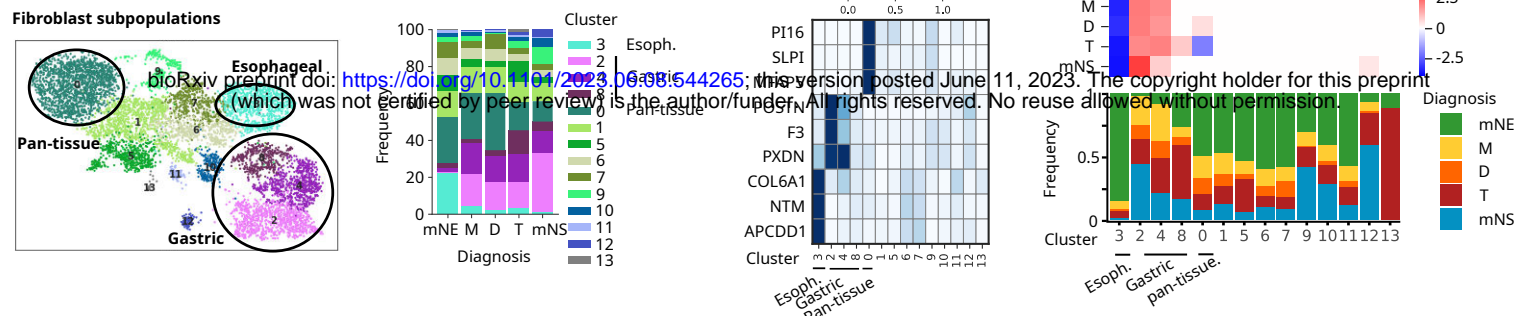
Average gene expression across tissues



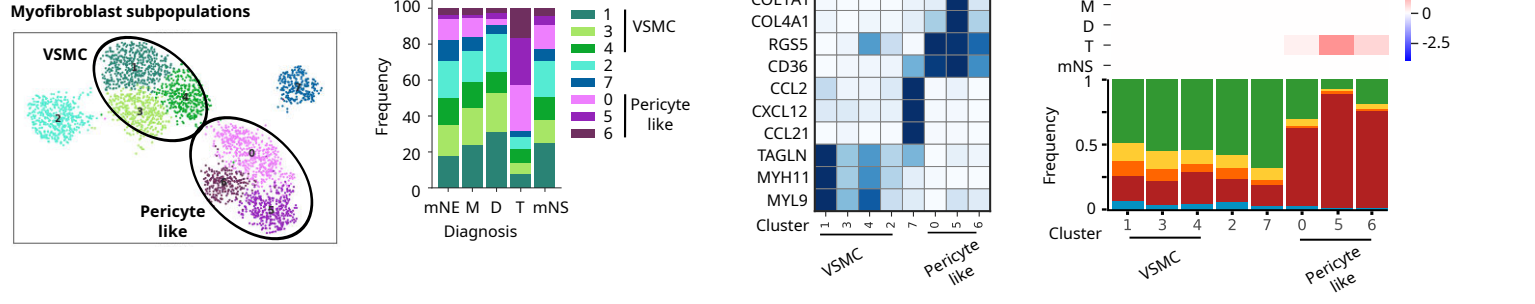
C



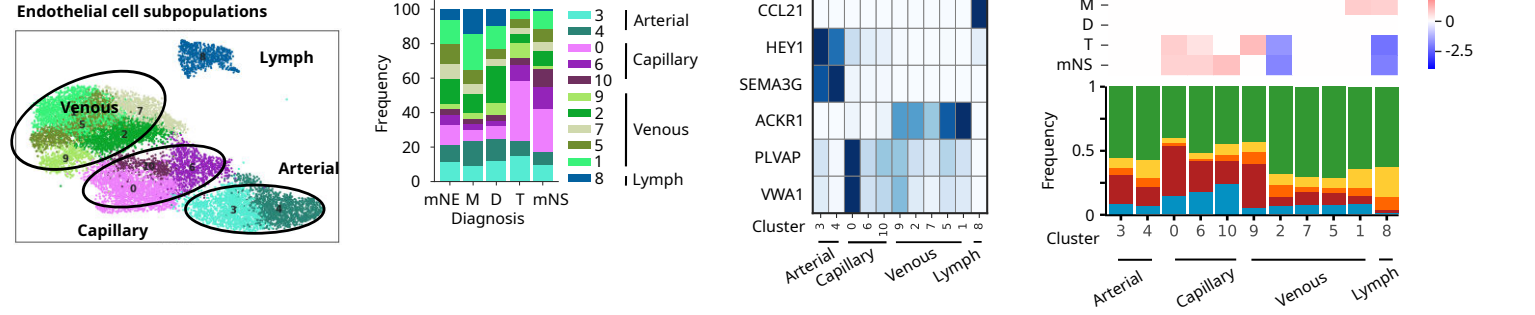
A



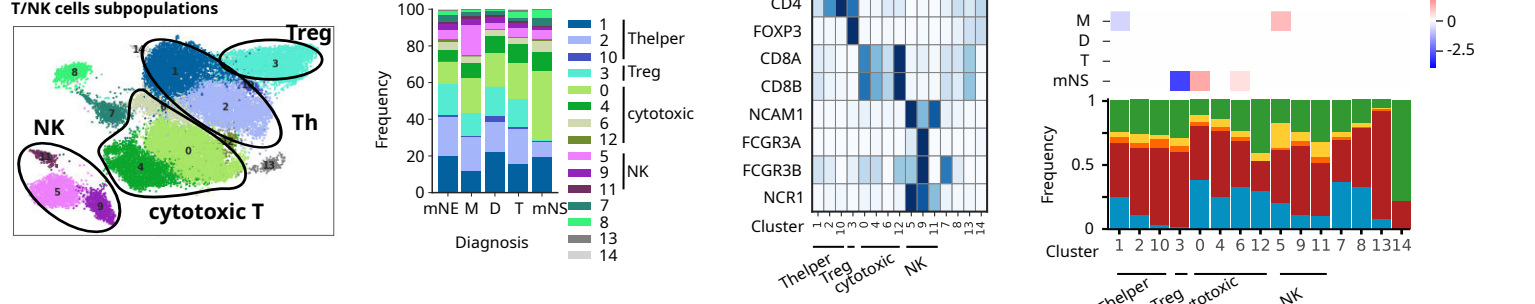
B



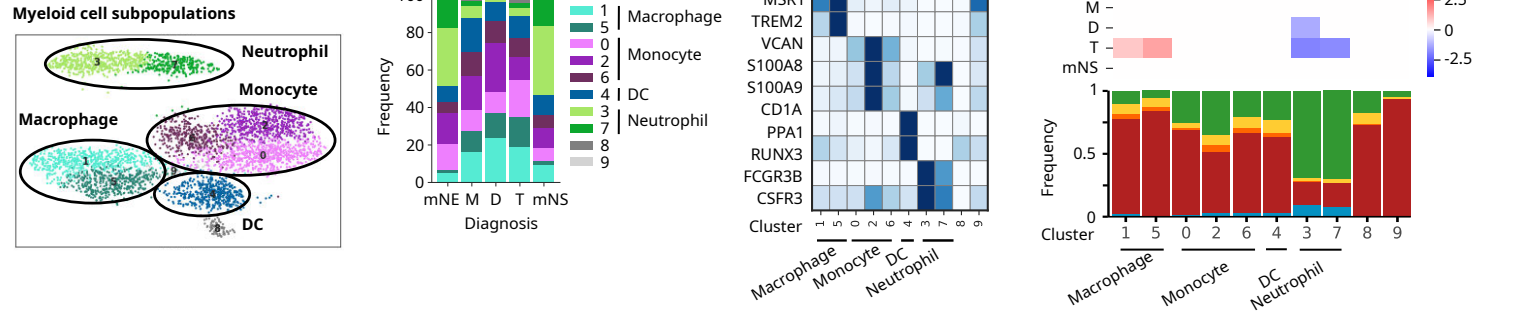
C



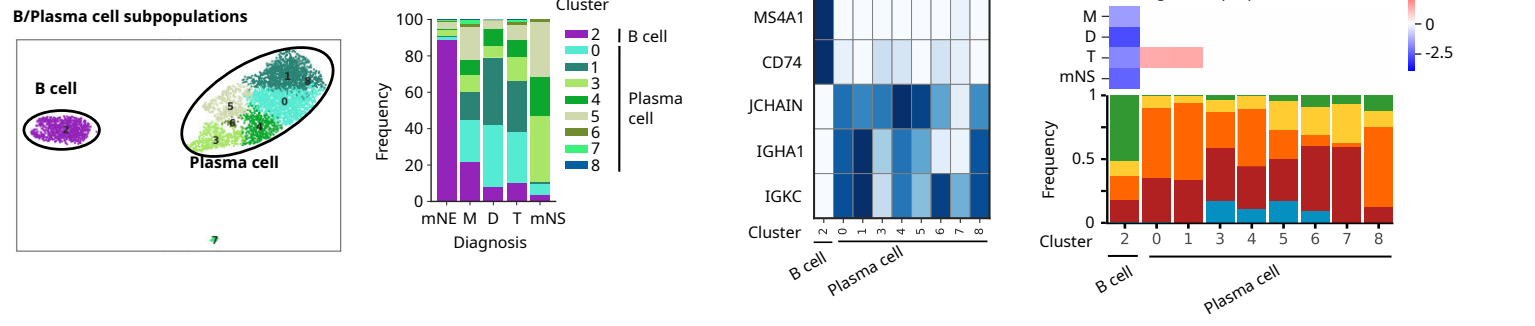
D

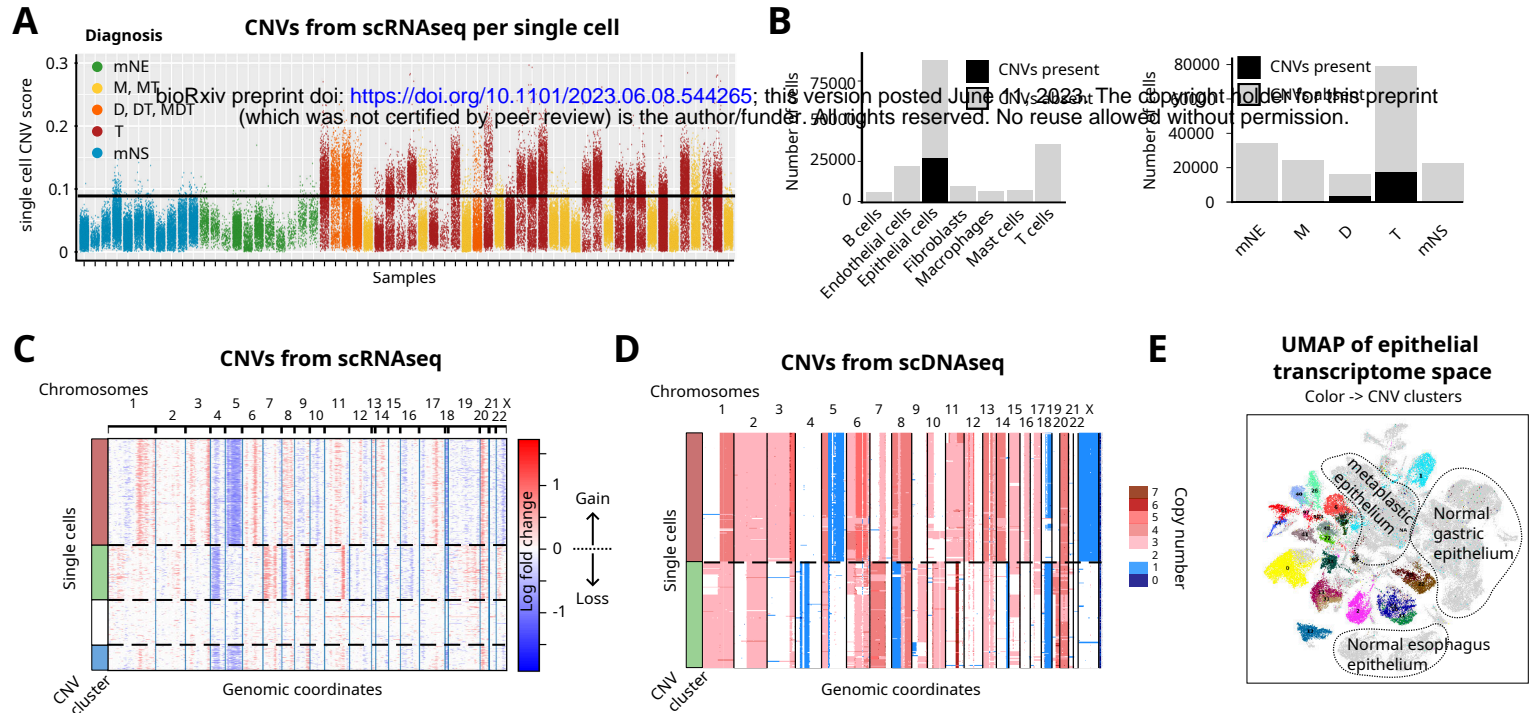


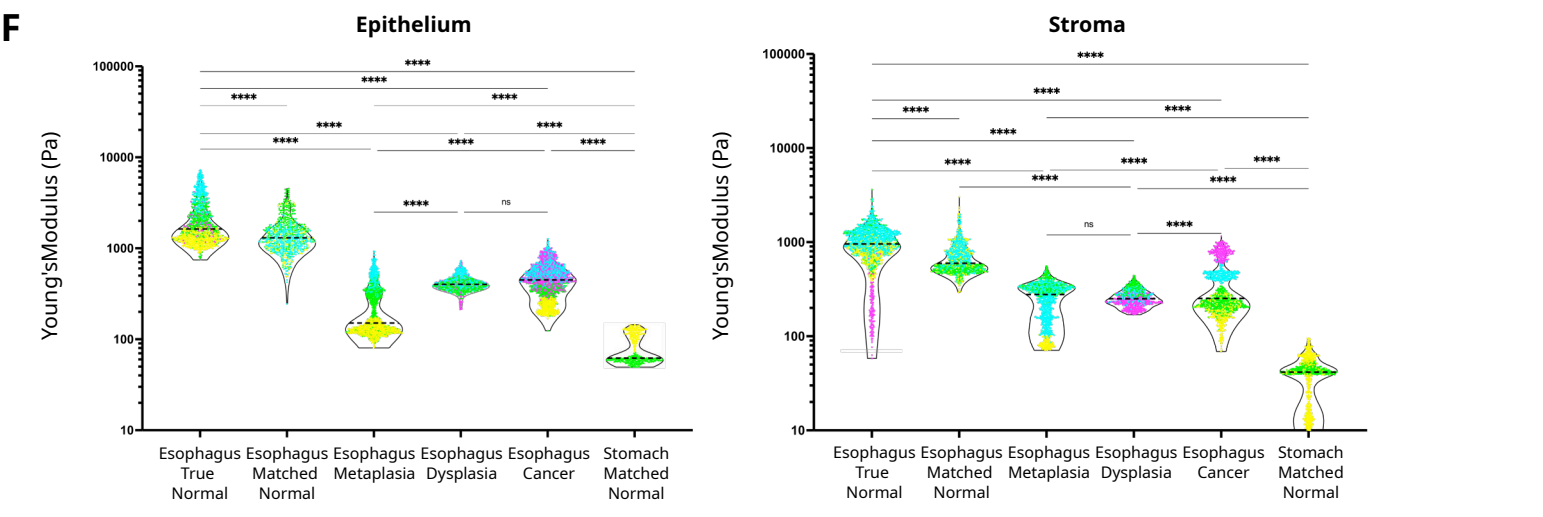
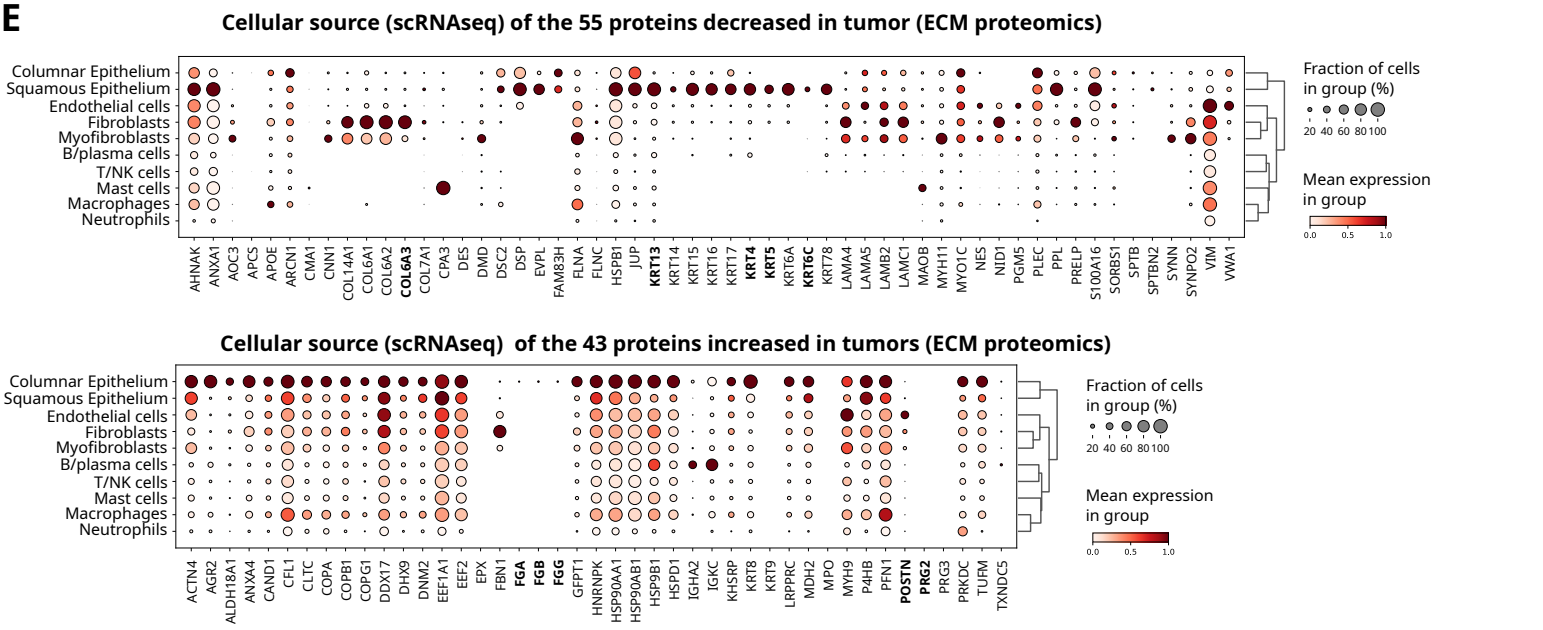
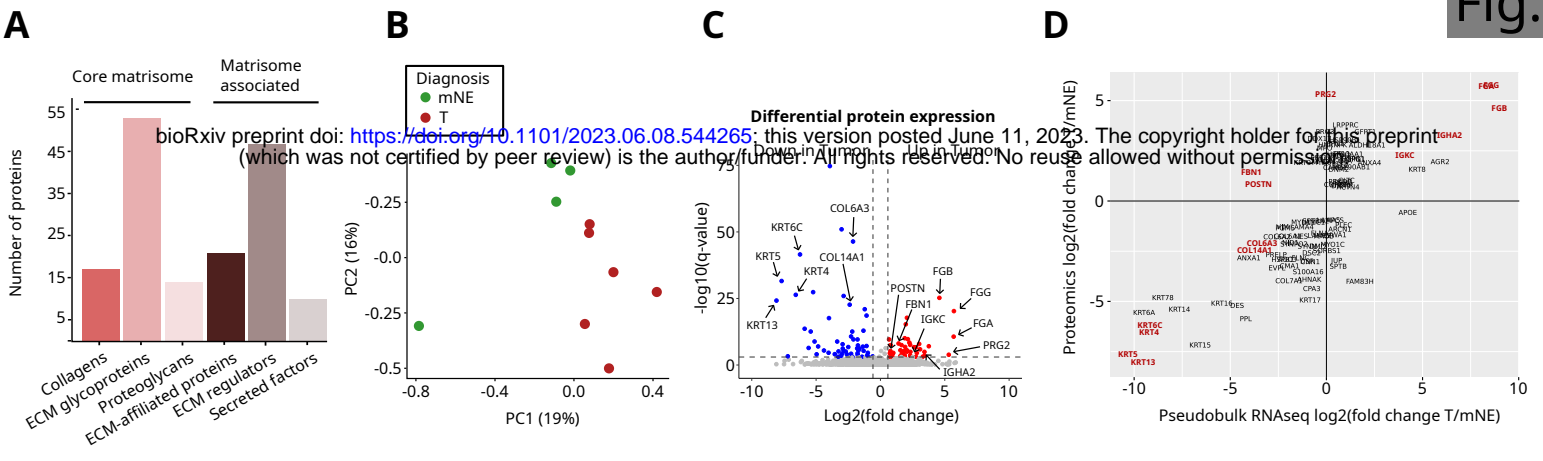
E

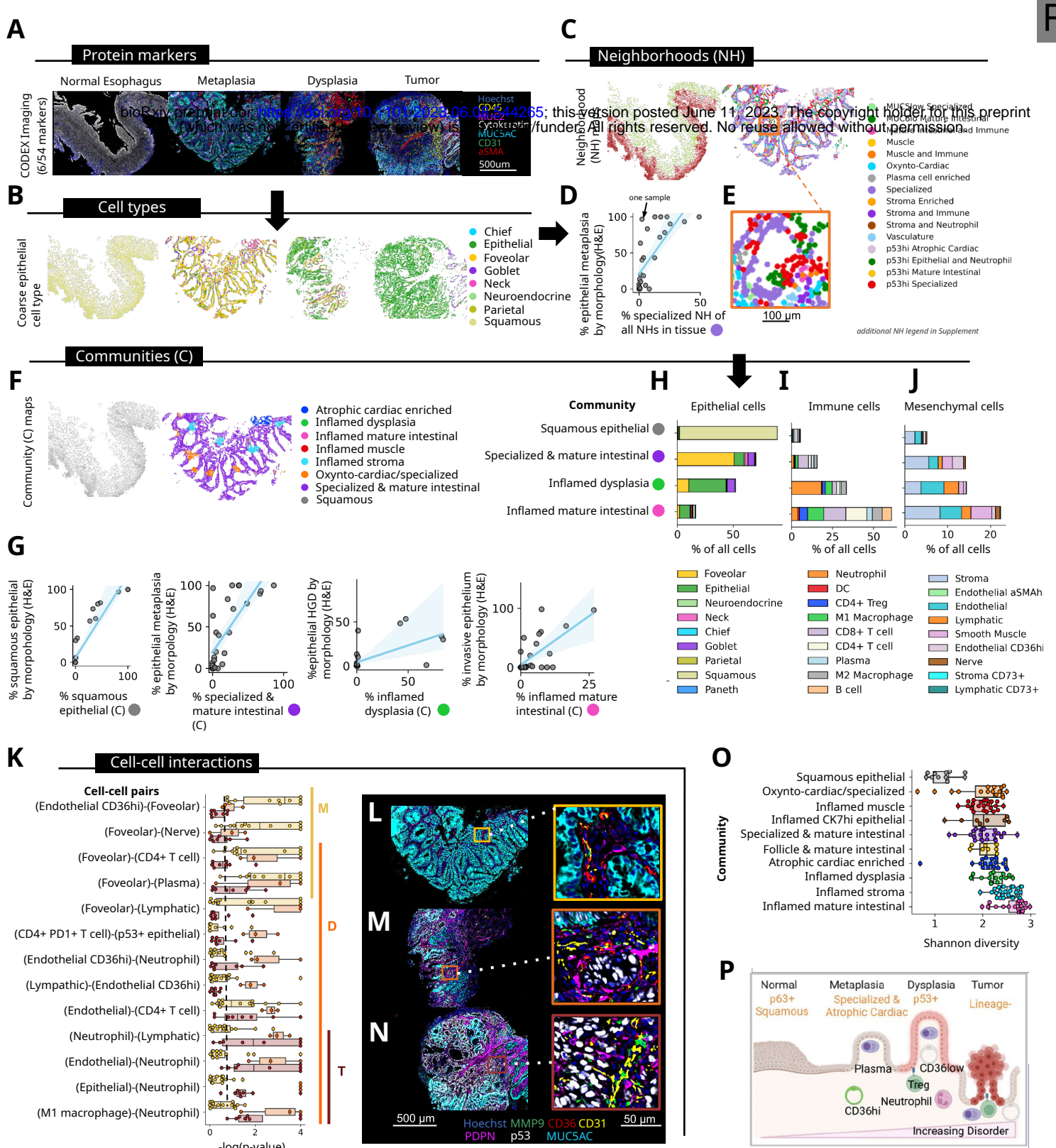


F









A

C

B

D

E

F

H

I

J

G

K

O

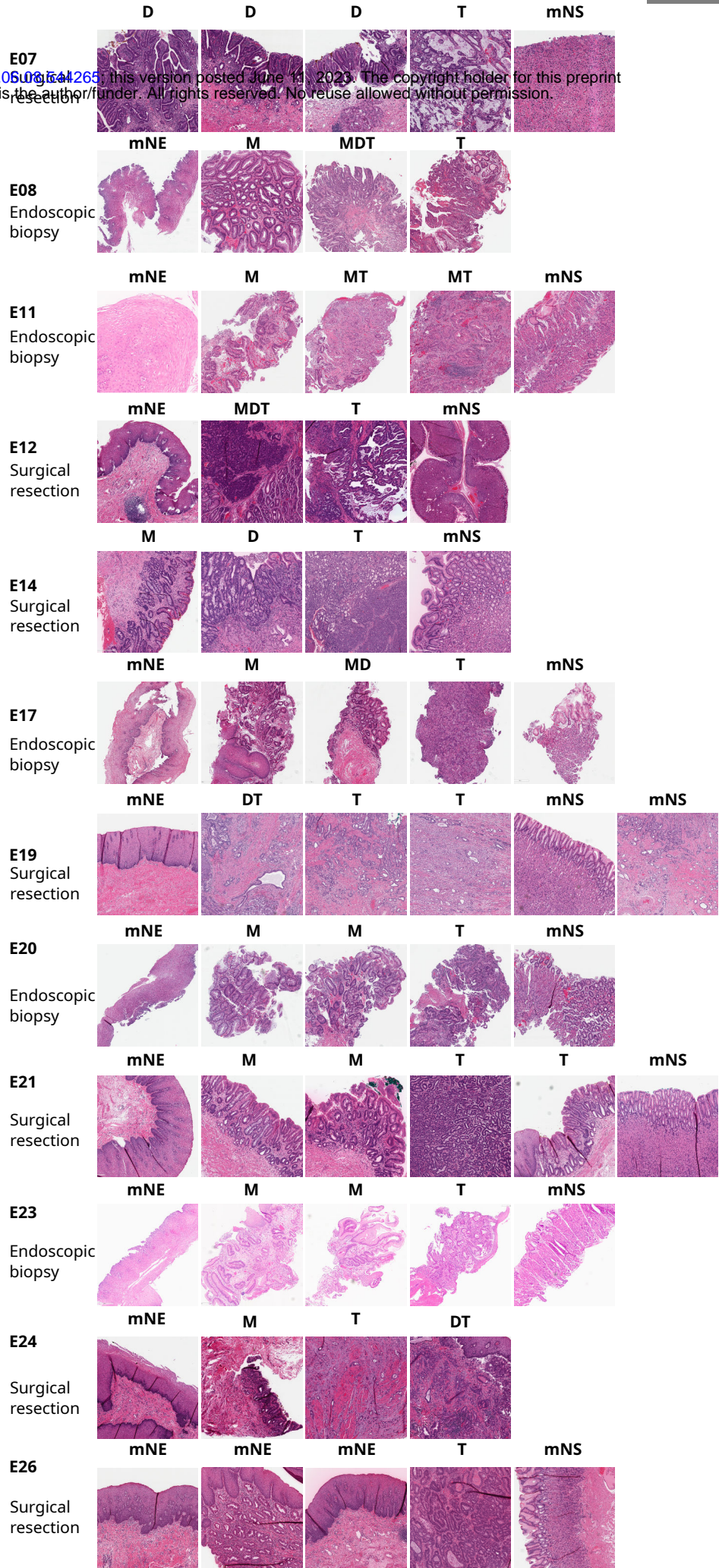
P

A

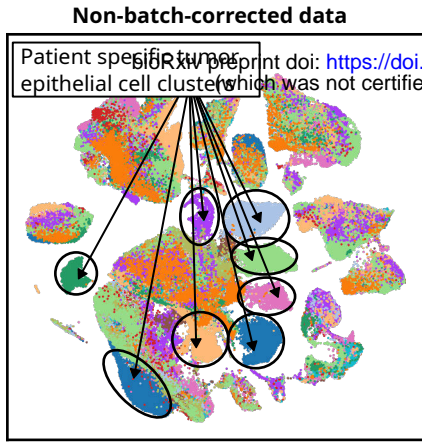
PATIENT	Type	Histological	ANALYSIS PERFORMED			SPECIMEN-ID
		diagnosis	scRNAseq	ECM-Proteome	CODEX	
E07	SR	D	Y	N	N	E07-c
		D	Y	N	N	E07-d1
		D	Y	N	N	E07-e
		T	Y	N	N	E07-f
E08	B	mNS	Y	N	N	E07-a
		mNE	Y	N	Y	E08-d
		M	Y	N	Y	E08-a
E08	B	TDM	Y	N	Y	E08-b
		T	Y	N	Y	E08-c
		mNE	Y	N	Y	E11-e
		M	Y	N	Y	E11-d
E11	B	MT	Y	N	Y	E11-b
		TM	Y	N	Y	E11-c
		mNS	N	N	Y	E11-a
		mNE	Y	N	Y	E12-a
E12	SR	MDT	Y	N	Y	E12-c
		T	Y	N	N	E12-b
		mNS	Y	N	Y	E12-d
		mNE	Y	Y	N	E14-a
E14	SR	M	Y	N	N	E14-c
		D	Y	N	N	E14-d
		T	Y	Y	N	E14-b
		mNS	N	N	N	E14-e
E17	B	mNE	Y	N	Y	E17-d
		M	Y	N	Y	E17-b
		MD	Y	N	Y	E17-c
		T	Y	N	Y	E17-a
E19	SR	mNS	Y	N	Y	E17-e
		mNE	Y	N	Y	E19-b
		TD	Y	N	Y	E19-f
		T	Y	N	Y	E19-a
E20	B	T	Y	N	N	E19-d
		mNS	Y	N	N	E19-c
		mNE	N	N	N	E20-e
		M	Y	N	N	E20-c
E21	SR	M	Y	N	N	E20-d
		T	Y	Y	N	E20-b
		mNS	Y	N	N	E20-a
		mNE	Y	Y	N	E21-f
E22	B	M	Y	N	N	E21-a
		M	Y	N	N	E21-d
		T	Y	N	N	E21-b
		T	Y	Y	N	E21-c
E23	B	mNS	Y	N	N	E21-e
		mNE	Y	N	N	E22-b
		mNE	Y	N	N	E22-c
		mNE	N	N	N	E22-e
E24	SR	T	Y	N	N	E22-d
		mNS	Y	N	N	E22-a
		mNE	Y	N	N	E23-e
		M	Y	N	N	E23-b
E26	SR	M	Y	N	N	E23-d
		T	Y	N	N	E23-c
		mNS	Y	N	N	E23-a
		mNE	Y	Y	N	E24-a
E26	SR	M	Y	N	N	E24-c
		T	Y	Y	N	E24-b
		TD	Y	N	N	E24-d
		mNE	Y	Y	N	E26-a
E26	SR	mNE	Y	N	N	E26-c
		mNE	Y	N	N	E26-d
		T	Y	Y	N	E26-b
		mNS	Y	N	N	E26-e

B

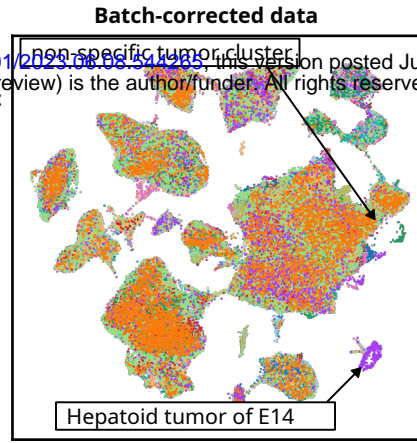
bioRxiv preprint doi: <https://doi.org/10.1101/2023.05.04.126505>; this version posted June 13, 2023. The copyright holder for this preprint (which was not certified by peer review) is the author/funder. All rights reserved. No reuse allowed without permission.



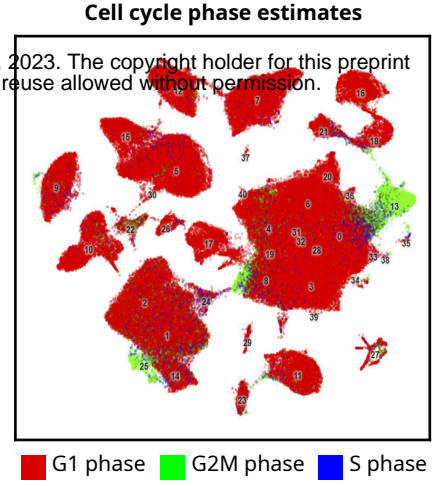
A



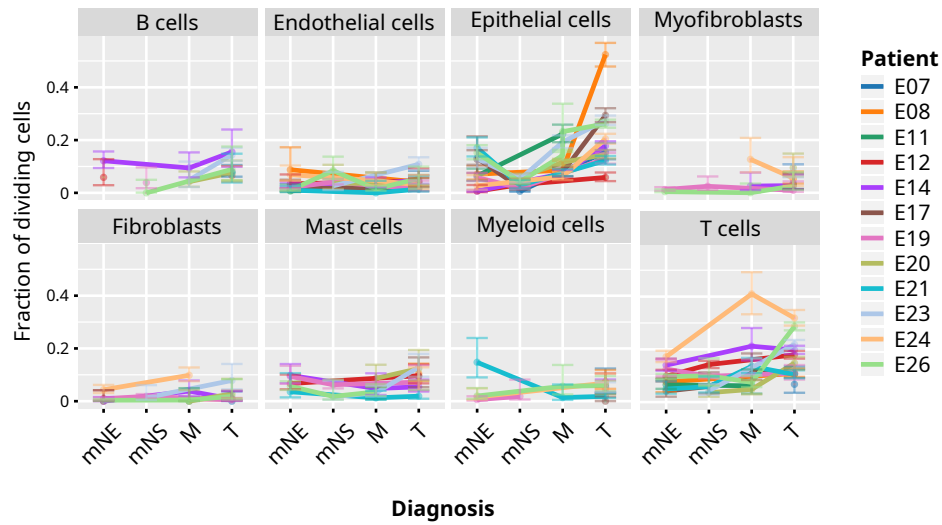
B



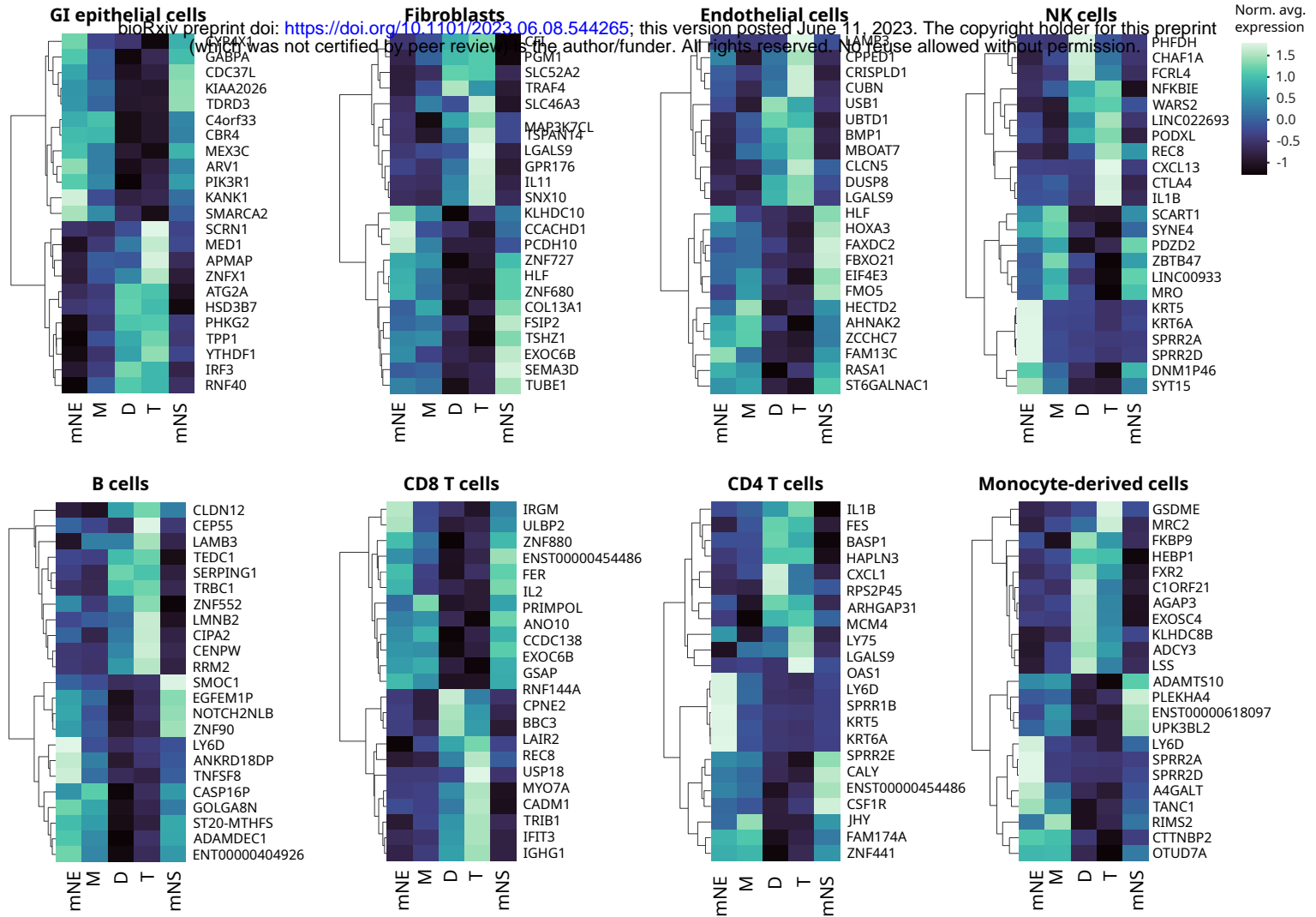
C



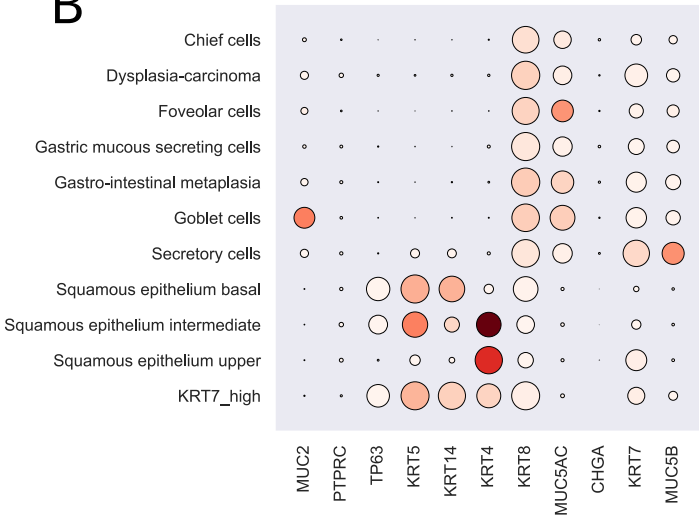
D



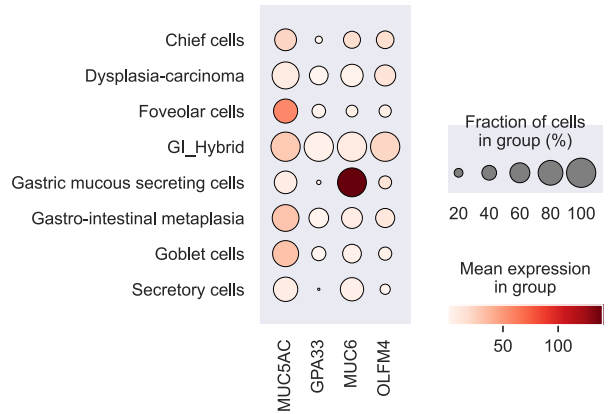
A



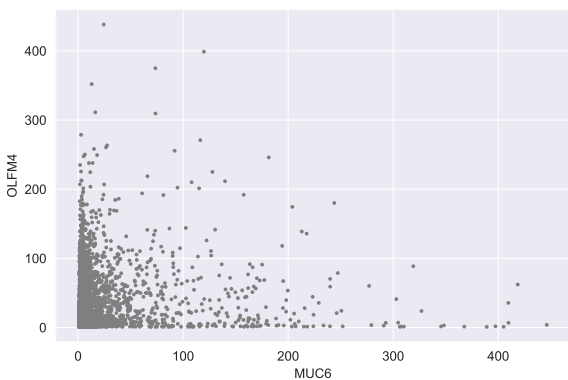
B

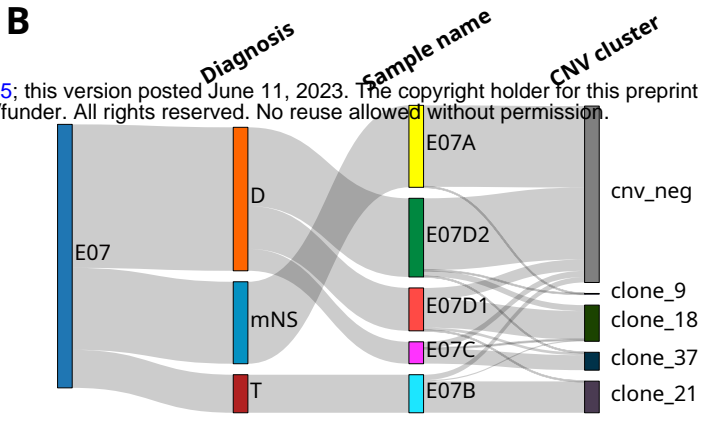
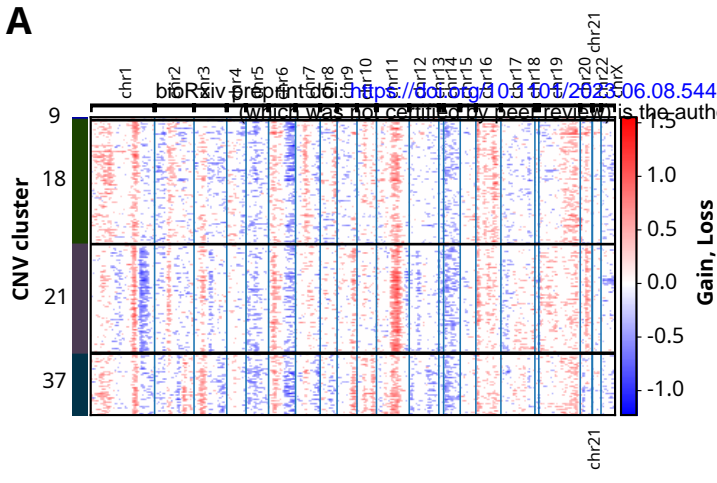


C



D





A. Top 10 proteins most altered in abundance detected in ECM preparation of tumor vs. normal esophagus

UniProt IDs	Genes	Protein Names	Protein Descriptions	Log ₂ (FC)	Log ₂ (FC)	Ratio	Qvalue
Q09666	AHNAK	AHNAK_HUMAN	Neuroblast differentiation-associated protein AHNAK	-3.93	3.93	0.07	1.85E-75
P15924	DSP	DESP_HUMAN	Desmoplakin	-3.02	3.02	0.12	1.06E-51
P12111	COL6A3	CO6A3_HUMAN	Collagen alpha-3(VI) chain	-2.13	2.13	0.23	4.03E-47
P48668	KRT6C	K2C6C_HUMAN	Keratin, type II cytoskeletal 6C	-6.25	6.25	0.01	2.94E-42
P13647	KRT5	K2C5_HUMAN	Keratin, type II cytoskeletal 5	-7.68	7.68	0.00	2.78E-32
P17661	DES	DESM_HUMAN	Desmin	-5.23	5.23	0.03	4.23E-28
P19013	KRT4	K2C4_HUMAN	Keratin, type II cytoskeletal 4	-6.58	6.58	0.01	4.32E-27
Q14315	FLNC	FLNC_HUMAN	Filamin-C	-2.86	2.86	0.14	1.16E-26
P02675	FGB	FIBB_HUMAN	Fibrinogen beta chain	4.58	4.58	23.91	5.89E-26
P13646	KRT13	K1C13_HUMAN	Keratin, type I cytoskeletal 13	-8.08	8.08	0.00	6.28E-25

q-value < 0.001 & absolute Log₂(FC) > 0.58

B. Matrisomal proteins altered in Tumor versus normal (patient-matched) esophagus

Genes	UniProt ID	Protein Descriptions	Matrisome Categories	Tumor vs Matched Normal
ANXA1	P04083	Annexin A1	ECM-affiliated proteins	-2.86
ANXA4	P09525	Annexin A4	ECM-affiliated proteins	1.88
COL14A1	Q05707	Collagen alpha-1(XIV) chain	Collagens	-2.39
COL6A1	P12109	Collagen alpha-1(VI) chain	Collagens	-1.78
COL6A2	P12110	Collagen alpha-2(VI) chain	Collagens	-1.81
COL6A3	P12111	Collagen alpha-3(VI) chain	Collagens	-2.13
COL7A1	Q02388	Collagen alpha-1(VII) chain	Collagens	-4.00
FBN1	P35555	Fibrillin-1	ECM glycoproteins	1.41
FGA	P02671	Fibrinogen alpha chain	ECM glycoproteins	5.69
FGB	P02675	Fibrinogen beta chain	ECM glycoproteins	4.58
FGG	P02679	Fibrinogen gamma chain	ECM glycoproteins	5.71
LAMA4	Q16363	Laminin subunit alpha-4	ECM glycoproteins	-1.32
LAMA5	O15230	Laminin subunit alpha-5	ECM glycoproteins	-0.98
LAMB2	P55268	Laminin subunit beta-2	ECM glycoproteins	-1.75
LAMC1	P11047	Laminin subunit gamma-1	ECM glycoproteins	-1.08
NID1	P14543	Nidogen-1	ECM glycoproteins	-2.10
POSTN	Q15063	Periostin	ECM glycoproteins	0.78
PRELP	P51888	Prolargin	Proteoglycans	-2.70
PRG2	P13727	Bone marrow proteoglycan	Proteoglycans	5.31
PRG3	Q9Y2Y8	Proteoglycan 3	Proteoglycans	3.43
S100A16	Q96FQ6	Protein S100-A16	Secreted factors	-3.55
VWA1	Q6PCB0	von Willebrand factor A	ECM glycoproteins	-1.71

Log₂(FC)

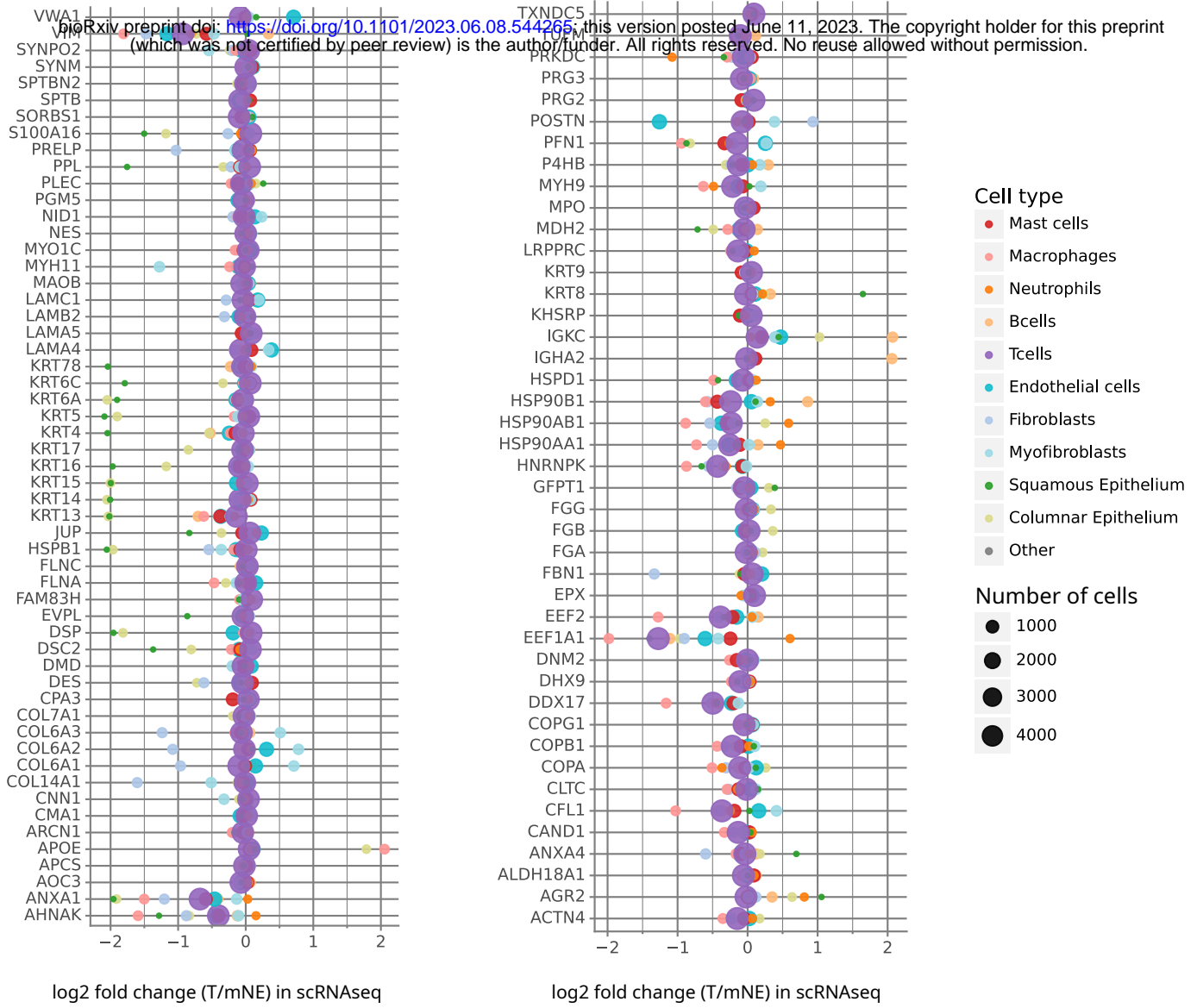


color display Log₂(FC) for the significantly altered proteins

A

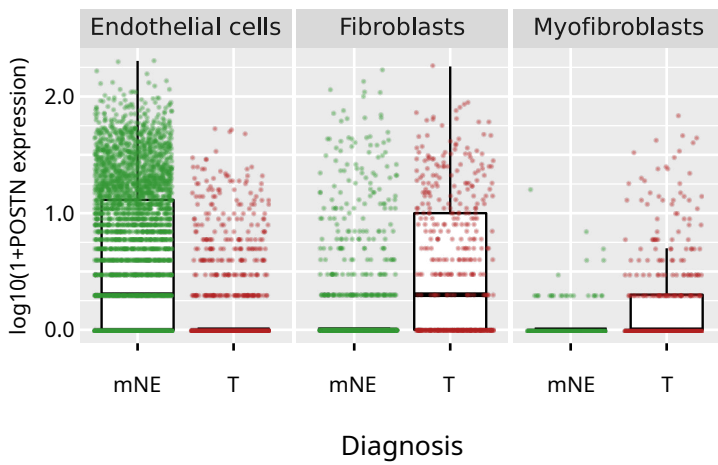
Downregulated (mNE->T) genes in ECM proteomics

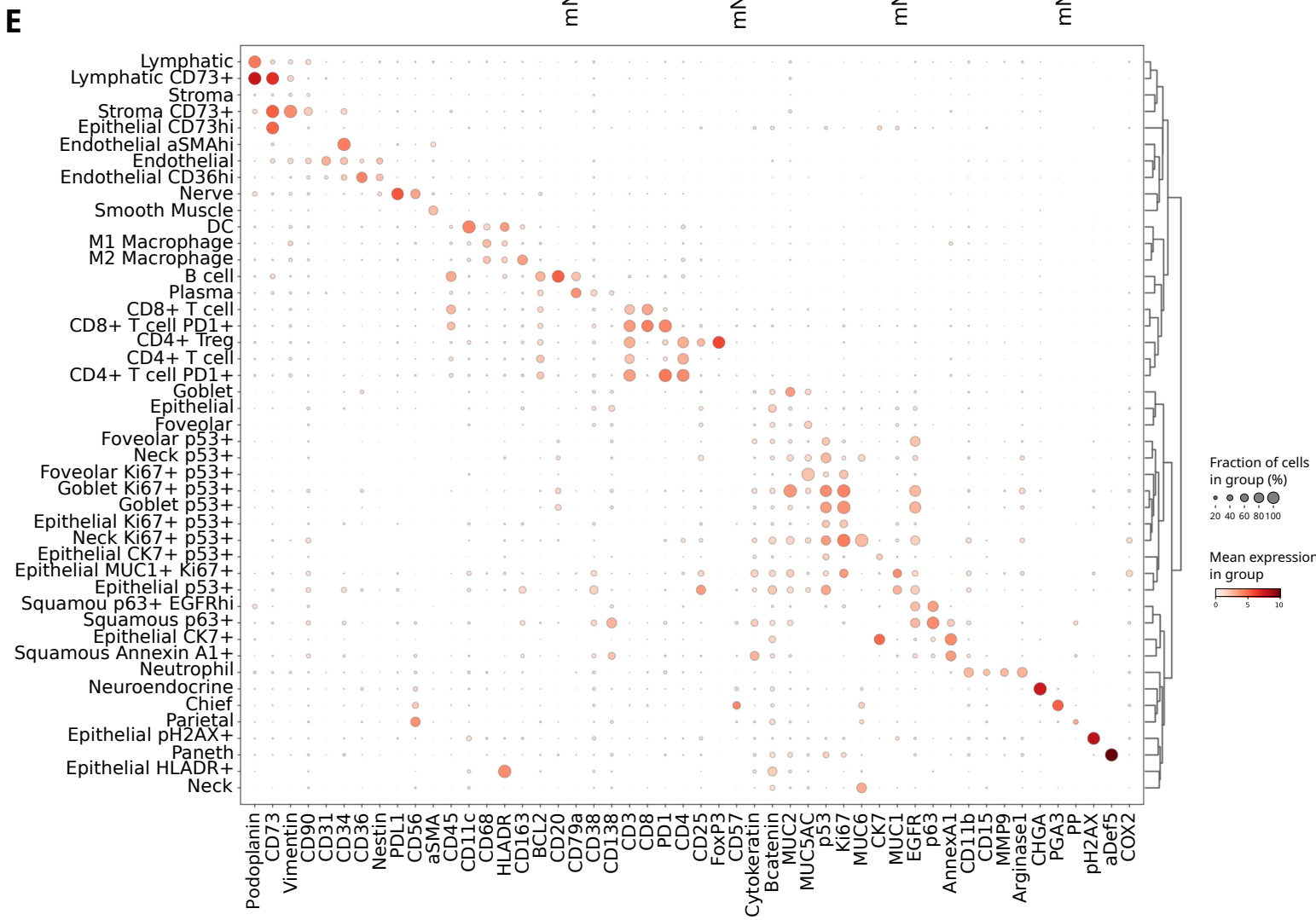
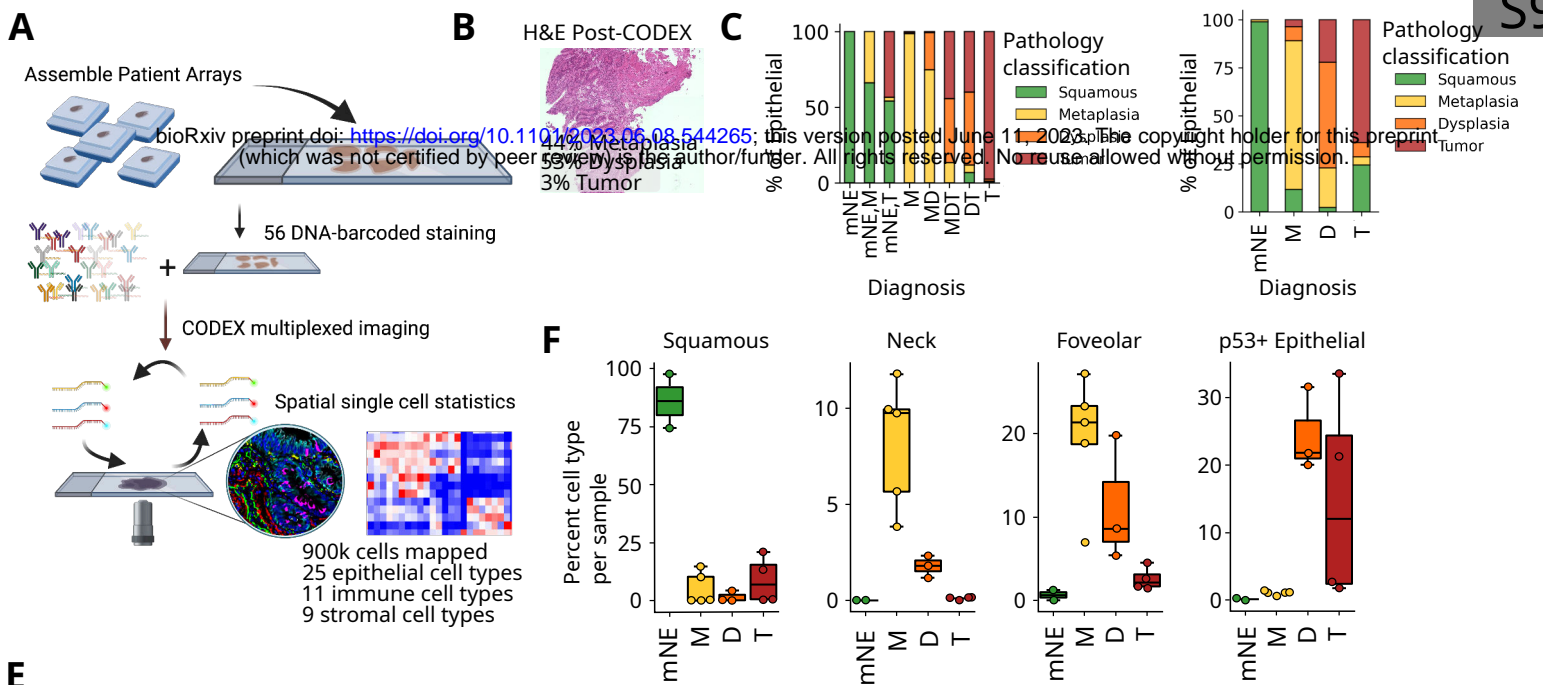
Upregulated (mNE->T) genes in ECM proteomics

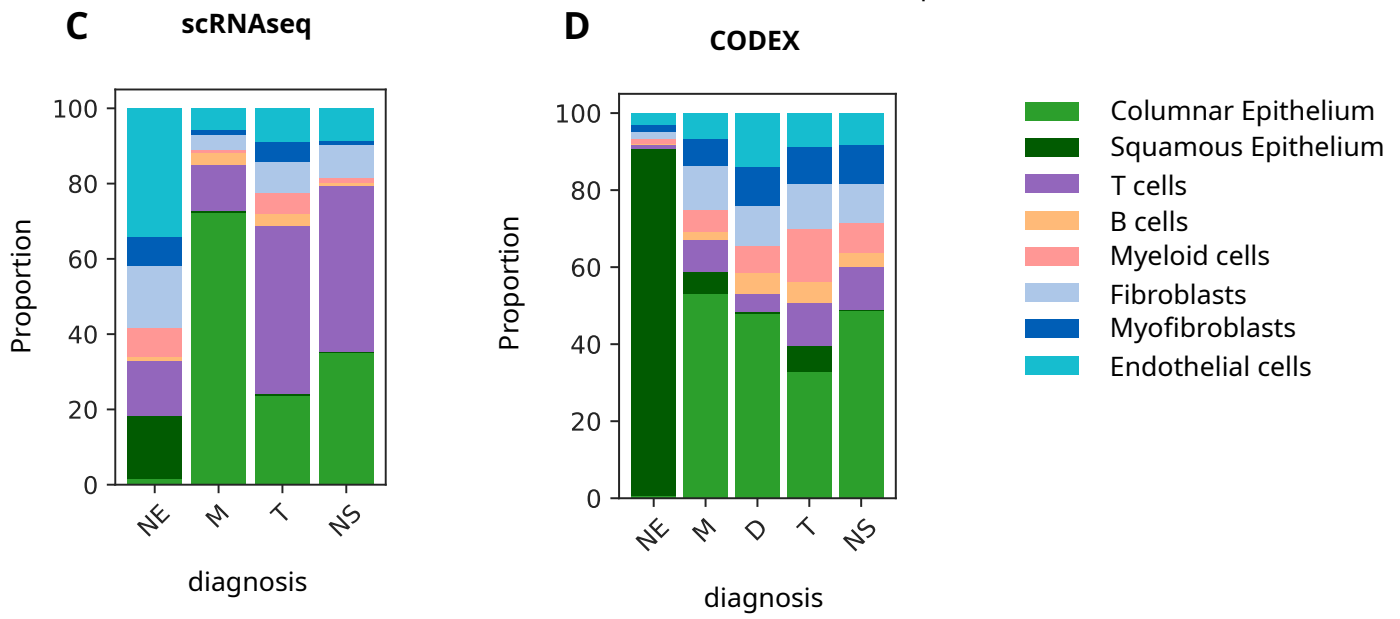
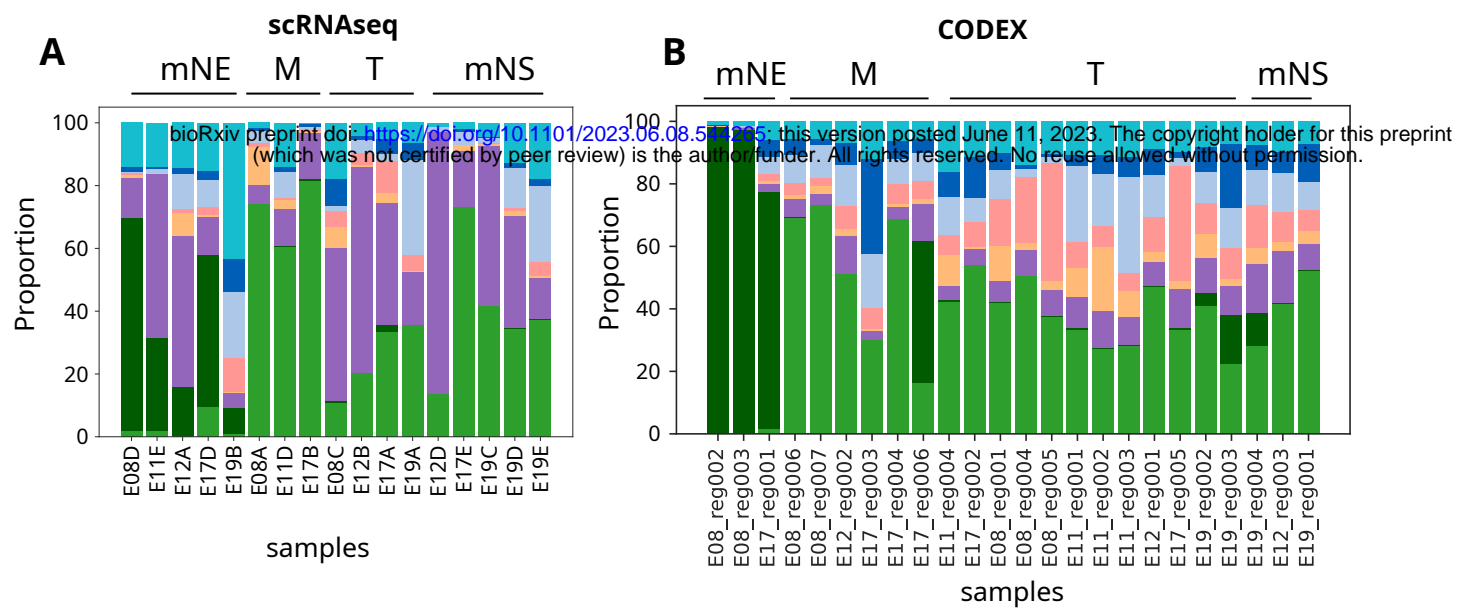


B

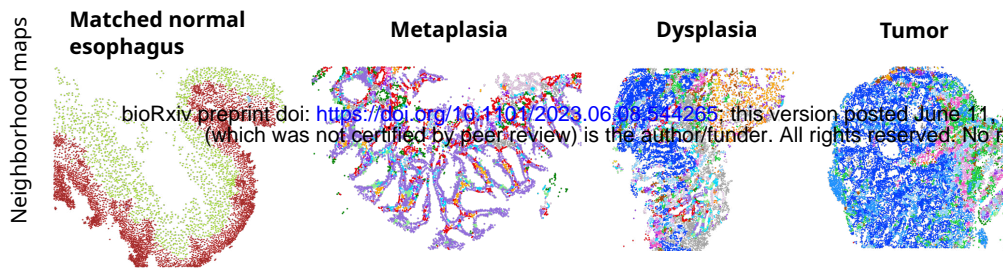
scRNAseq expression of POSTN



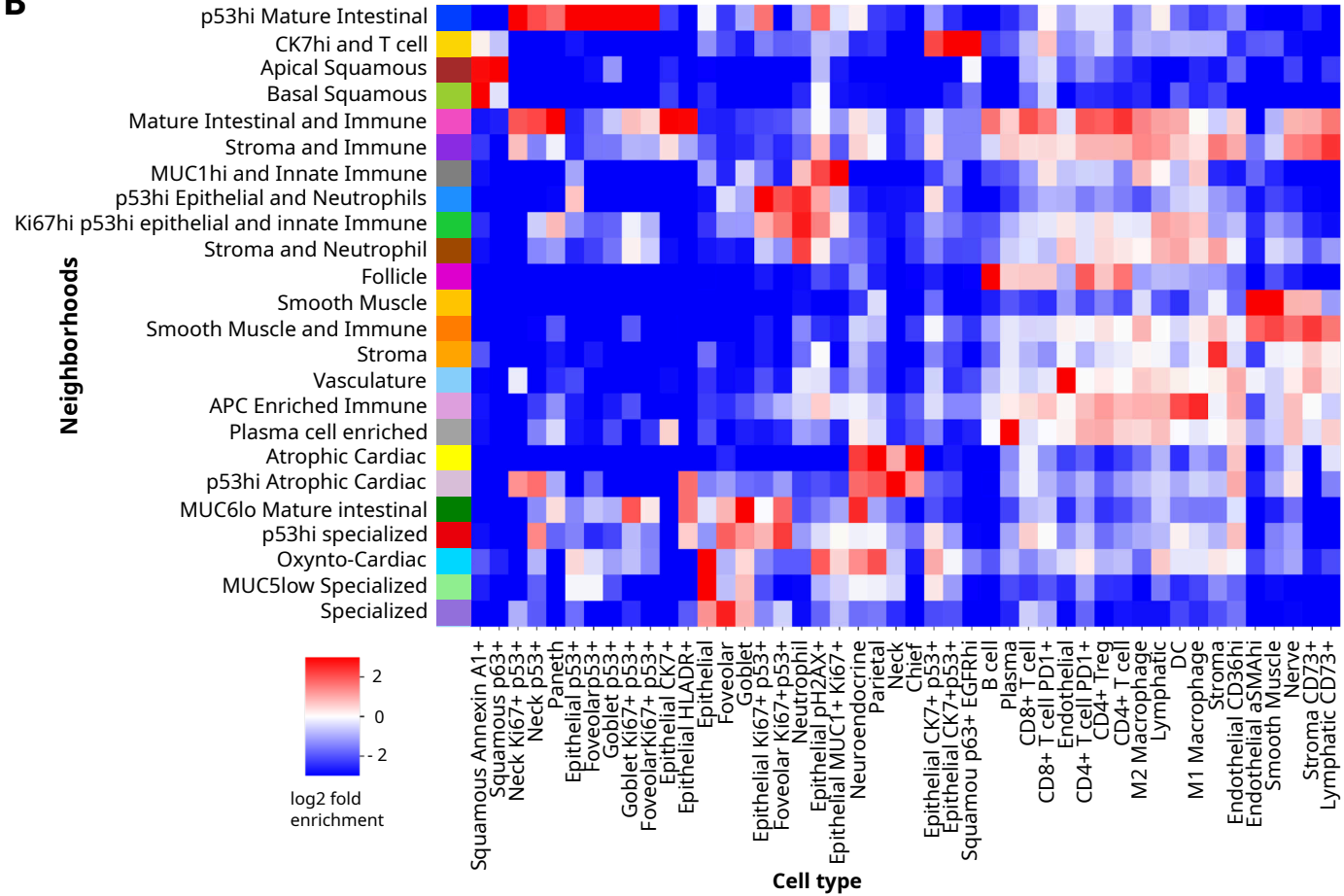




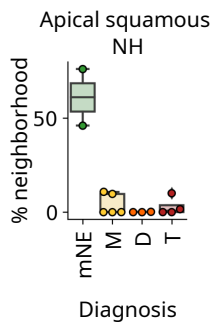
A



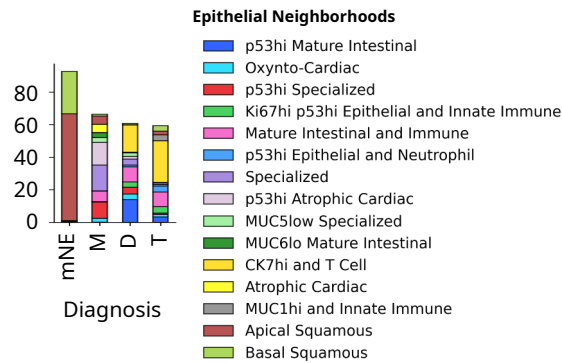
B



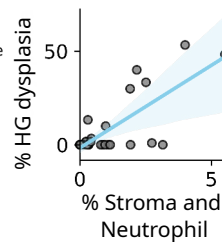
C



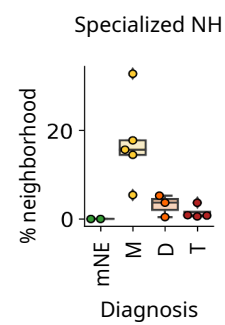
D



E



F



G

